Measurement of the magnetic moment of the 2+ state of 72Zn via extension of the high-velocity transient-field method

Enrico Fiori

To cite this version:

Enrico Fiori. Measurement of the magnetic moment of the 2+ state of 72Zn via extension of the high-velocity transient-field method. Nuclear Theory [nucl-th]. Université Paris Sud - Paris XI, 2010. English. NNT : . tel-00626463

HAL Id: tel-00626463
https://theses.hal.science/tel-00626463
Submitted on 26 Sep 2011

UNIVERSITÉ PARIS-SUD 11

Measurement of the magnetic moment of the 2_1^+ state of ^{72}Zn via extension of the high-velocity transient-field method

by

Enrico Fiori

A thesis submitted in partial fulfillment for the
degree of Doctor of Philosophy

in the
Faculté des sciences d'Orsay
École Doctorale 534 MIPEGE

13th December 2010

“Never argue with an idiot: they will lower you to their level and then beat you with experience”

Woody Allen

UNIVERSITÉ PARIS-SUD 11

Abstract

Faculté des sciences d'Orsay
École Doctorale 534 MIPEGE

Doctor of Philosophy

by Enrico Fiori

Magnetic moments can provide deep insight for nuclear structure and of the wave function composition, particularly when the single particle character of the nucleus is dominating. For this reason, the magnetic moment of the first excited state of the radioactive neutron-rich ^{72}Zn was measured at the Grand Accélérateur National d'Ions Lourds (GANIL, Caen, France). The result of the experiment confirmed the trend predicted by the shell model calculations, even if the error on the measurement did not allow for a rigorous constraint of the theories.

The measurement was performed using the transient field (TF) technique and the nuclei of interest were produced in a fragmentation reaction. Before this experiment, the high-velocity TF technique had been used only with projectile up to $Z = 24$. It was the first time that a magnetic moment of an heavy ion with $Z > 24$ was measured in the high velocity regime.

To further develop the technique and to gather information about the hyperfine interaction between the polarized electrons and the nucleons, two experiments were performed at the Laboratori Nazionali del Sud (LNS, Catania, Italy).

In this thesis the development of the high-velocity TF technique for the experiments on $g(2^+;^{72}Zn)$ and $B_{TF}(Kr, Ge)$ is presented. The analysis of the results and their interpretation is then discussed.

UNIVERSITÉ PARIS-SUD 11

Résumé

Faculté des sciences d'Orsay
École Doctorale 534 MIPEGE

Thèses de Doctorat

de Enrico Fiori

Les moments magnétiques peuvent donner des détails sur la structure nucléaire et sur la composition de la fonction d'onde du noyau, tout spécialement si le caractère de particule indépendante du noyau est prépondérant. Pour cette raison, le moment magnétique du premier état excité du noyau radioactif riche en neutrons ^{72}Zn a été mesuré au Grand Accélérateur National d'Ions Lourds (GANIL, Caen, France). Le résultat de l'expérience a confirmé les prédictions du modèle en couches, même si l'incertitude sur la mesure ne pouvait pas contraindre fortement les modèles.

La mesure a été effectuée en utilisant la technique du champ transitoire (TF) et les noyaux d'intérêt ont été produits par fragmentation. Avant cette expérience, la technique TF à haute vitesse n'avait été utilisée qu'avec des projectiles allant jusqu'à Z=24. Ce fut donc la première fois qu'un moment magnétique d'un ion lourd avec Z >24 avait été mesurée à cette vitesse.

Afin de développer la technique et de recueillir des informations sur l'interaction hyperfine qui agit entre les électrons et les noyaux polarisés, deux expériences ont été menées au Laboratorio Nationale del Sud (LNS, Catane, Italie).

Dans cette thèse, je présenterai le développement de la technique TF à haute vitesse pour les expériences $g(2^+;^{72}Zn)$ et $B_{TF}(Kr,Ge)$. L'analyse des résultats et leur interprétation seront ensuite discutées.

Contents

Abbreviations

BFO	**B**rute **F**orce **O**rientation
ESPE	**E**ffective **S**ingle **P**article **E**nergy
FWHM	**F**ull **W**idth **H**alf **M**aximum
HPGe	**H**igh **P**urity **Ge**rmanium detector
HVTF	**H**igh **V**elocity **T**ransient **F**ield
IPAD	**I**ntegral **P**erturbed **A**ngular **D**istribution
IPM	**I**ndependent **P**article **M**odel
LSSM	**L**arge **S**cale **S**hell **M**odel
NMR	**N**uclear **M**agnetic **R**esonance
RF	**R**adio **F**requency
RIG	**R**ecoil **I**n **G**as
RIV	**R**ecoil **I**n **V**acuum
SM	**S**hell **M**odel
TBME	**T**wo **B**ody **M**atrix **E**lement
TDPAC	**T**ime **D**ifferential **P**erturbed **A**ngular **C**orrelation
TDPAD	**T**ime **D**ifferential **P**erturbed **A**ngular **D**istribution
ToF	**T**ime of **F**light
TF	**T**ransient **F**ield

Physical Constants

speed of light	c	=	$2.997\ 924\ 58 \times 10^{8}\ m \cdot s^{-1}$
reduced Planck constant	$\hbar$	=	$1.054\ 571\ 628 \times 10^{-34}$ J·s
elementary charge	e	=	$1.602\ 176\ 487(40) \times 10^{-19}$ C
proton mass	m_p	=	$1.672\ 621\ 637(83) \times 10^{-27}$ kg
nuclear magneton	$\mu_N = \frac{e\hbar}{2m_p}$	=	$5.050\ 783\ 24(13) \times 10^{27}\ \mathrm{J{\cdot}T^{-1}}$
electric constant	$\epsilon_0 = (\mu_0 c^2)^{-1}$	=	$8.854\ 187\ 817 \times 10^{-12}\ \mathrm{F{\cdot}m^{-1}}$
magnetic constant	$\mu_0 = 4\pi \times 10^{-7}$	=	$1.256\ 637\ 061 \times 10^{-6}\ \mathrm{N{\cdot}A^{-2}}$
Bohr velocity	$v_0 = c/137$	=	$2.188\ 266\ 117 \times 10^{6}\ \mathrm{m{\cdot}s^{-1}}$

All values from CODATA [1]

Used Symbols

$\vec{B}$	magnetic field	tesla
B_{ns}	electron's field at nucleus	tesla
$B(E\lambda; I_i \rightarrow I_f)$	reduced transition probability	
$D^k_{qq'}(\alpha, \beta, \phi)$	rotation matrix	
G_k	recoil-in-vacuum attenuation parameter	
$P_k(x)$	Legendre polynomial	
S	slope	
$W(\theta)$	angular distribution	
$Y_{kq}(\theta, \phi)$	spherical harmonic	

ω_L	Larmor frequency	rad^{-1}
$\vec{\tau}$	torque	kg·m
$\delta_{2(n,p)}$	second difference in binding energy	MeV
$\Delta\theta$	precession angle	rad
ϵ	asymmetry	
η	Sommerfeld parameter	
Φ	precession angle per units of g-factor	rad
ξ	adiabaticity parameter	
ρ_{kq}	statistical tensor	

A mia madre,
alla mia famiglia.

Chapter 1

Theoretical background

Les noyaux sont constitués par des nucléons unis par la force nucléaire forte. La disposition de ces nucléons dans des configurations particulières caractérise les propriétés nucléaires comme les énergies des niveaux excités par rapport à l'état fondamental, les probabilités de transition et les moments magnétiques. En même temps, ces quantités donnent de nombreuses informations sur la structure nucléaire. Leur mesure est donc l'instrument principal pour connaitre la structure et le fonctionnement du noyau. En principe, le comportement et les propriétés des noyaux pourraient être calculés à partir des constituants fondamentaux, les protons et les neutrons, avec la bonne interaction. Malheureusement l'interaction n'est pas connue aussi exactement que l'est l'interaction électromagnétique. À ceci il faut ajouter le fait que la complexité de cette tâche grandis très vite avec le nombre des nucléons, et atteint très vite les limites des ordinateurs actuels. Pour ça, les résultats des modèles nucléaires développés récemment, de plus en plus précis mais toujours approximatifs, doivent être comparés à la réalité : la physique nucléaire a besoin des résultats expérimentaux.

Cette thèse est dédiée à la mesure du moment dipolaire magnétique, qui donne des informations très précises sur la composition de la fonction d'onde de l'état nucléaire. Une technique expérimentale très utilisée pour la mesure des facteurs gyromagnétiques des niveaux de courte demi-vie, de l'ordre des ps, est la méthode dite du champ transitoire (TF, Transient Field en anglais). Les champs magnétiques qui peuvent être atteints sont de l'ordre du kTesla et plus. Le TF est engendré par l'interaction hyperfine entre les électrons, polarisé par un champ magnétique extérieur, et le noyau. Les niveaux sont peuplés par excitation coulombienne. Cette technique de production a était utilisée depuis le début de la physique nucléaire expérimentale, sa force réside dans la théorie bien établi qui donne une bonne prédictibilité des résultats et dans la section efficace, normalement plus forte que pour les autres mécanismes de réactions nucléaires.

1.1 Introduction

Nuclei are constituted of protons and neutrons. The glue that is keeping the particles together, despite the repulsive Coulomb force, is the short-range strong nuclear force. The arrangement of the nucleons in a particular state gives rise to different nuclear properties, like the charge distribution, the nuclear radius, the energy of the state with respect to the ground state, the transitions probabilities, its half-life, the nucleon separation energy, the magnetic dipole and electric quadrupole moments. The measurement of these quantities leads to an understanding of the nuclear structure. Magnetic dipole moments are particularly sensitive to the wave function composition and their knowledge can lead to a precise determination of the proton and neutron components.

In principle, knowing the interaction it would be possible to calculate all these properties *ab initio*, building the nuclei using their basic components. Unfortunately, the present knowledge of the nuclear interaction does not allow us to go very far from the simplest cases. For this reason arises the necessity of performing experiments, to assure a basis of experimental results to which the theories can be compared.

Section 1.2 will deal with the electromagnetic moments of the nuclear states. In most cases not all the particles in the nucleus are actively taking part in the determination of the properties of the state. The wave function composition will reflect this gross experimental observation: only the active particles are represented. If only a very limited number of nucleons are involved, the state is said to have a *single particle character*, while if the number of particles is elevated, without a particular one standing out, we are speaking about *collective behavior*. Nuclear moments are very sensitive to single-particle character (magnetic dipole moments) and to collectivity and deformation (electric quadrupole) of nuclear states.

In the section 1.3 Coulomb excitation will be discussed. Since the very beginning of the particle accelerator era, this technique gave physicists the possibility to populate nuclear states, particularly collective states. The strength of the technique is the very well established theory behind it that allows for a reliable calculation of cross sections and angular distributions. Additionally, under most experimental conditions the cross section for Coulomb excitation of the first excited state is considerably higher than for other nuclear reactions.

Section 1.4 is about the hyperfine transient field effect that appears when an ion moves swiftly in a polarized ferromagnet. The electrons' magnetic field at the nucleus position can be very strong, in the kT/MT range, much higher than any macroscopic field man-made in laboratories. The transient field arises from the hyperfine interaction of such electrons' magnetic field with the nuclear magnetic moment, inducing a precession effect of the latter one. Under normal conditions the electrons' fields are isotropically distributed, but an external magnetic field can polarize them. The result is a total effect acting like a very intense magnetic field parallel to the polarization direction. The magnitude of the generated magnetic field provides physicists with an effective tool for measuring magnetic moments of very short lived states.

In chapter 2 a description of the region of the isotopic table in which we were interested is given. The nuclear dynamics of the region around the presumed doubly-magic ${}^{68}_{28}\mathrm{Ni}_{40}$ is illustrated. The nuclear interaction is investigated studying the evolution of the Ni, Cu, Co and Zn isotopic chains when going far away from stability, on the neutron rich-side. Chapters 3 and 4 will be devoted to the description of the experiments and to the interpretation of their results. Firstly the measurement of the g-factor of the neutron-rich ${}^{70}_{30}\mathrm{Zn}_{40}$ is presented, the physics case behind it and the analysis of the results. Secondly the technical development of the high-velocity transient-field technique is reported, with the perspective for the application to radioactive-ions beams.

The thesis is concluded by chapter 5, which sums up the work and set the direction of the outlooks of this technique.

The work of this first two chapter, with the exception of section 1.3.7, is taken from different sources to provide the reader with the necessary background for the understanding of chapters 3 and 4. Section 1.3.7 is a personal theoretical interpretation of the problems arose in the experiment described in Chap. 4.

1.2 Magnetic dipole moment

In 1924 Pauli [2] introduced the intrinsic angular momentum as a fundamental quantity associated with all particles. The year after this quantity was called *spin* by R. Kronig, G. Uhlenbeck and S. Goudsmith [3], with the analogy of spinning motion around its own axis.

Any mechanical angular moment, when associated to electric charges, creates a magnetic moment. This is true for particles as well. In complex systems like the nuclei, the resulting magnetic moment is the sum of all the magnetic moments of the constituents, added according to characteristic addition rules.

The theoretical basis for the measurement of magnetic moments of excited states was drawn up by E. L. Brady and M. Deutsch [4] in 1950 and exploited experimentally the year after by H. Frauenfelder and his group [5]. Observing the $\gamma - \gamma$ cascade from a ${}^{111}\mathrm{In}$ source, they measured the magnetic moment of the intermediate state of ${}^{111}\mathrm{Cd}$ by measuring the influence of an external magnetic field on the angular correlation. Nowadays this technique is called Perturbed Angular Correlation (PAC) and has become one of the most precise and used technique for magnetic moment measurement.

Another technique, proposed by Bloch *et al.* in 1946 [6] with the name of *nuclear induction* and later on called Nuclear Magnetic Resonance (NMR), has been improved and developed to become one of the most important diagnostic tools in medicine, the Magnetic Resonance Imaging (MRI).

Up to 1955 only four magnetic moments were known with an accuracy of about twenty percent. During the next decade this number increased to 40. In 1963 R. Steffen, in the closing speech at the conference *Extranuclear Perturbations in Angular Correlations*, predicted that not more than 100 magnetic moments of excited states could be measured. Steffen proved to be undoubtedly wrong: already in the next five years 150 new magnetic moments were measured. What made this leap possible was the increased understanding and use of hyperfine internal fields, the availability of isotope separators and a better knowledge of nuclear reactions. Many new techniques were elaborated and old techniques were adapted and improved to fit the new challenges. Especially the internal hyperfine fields arising from the interaction of the target's lattice with the projectile (the 'impurity'), in the beginning considered as a complication to the measurements, began to be probed with nuclei with well known magnetic moments. Very strong magnetic fields were discovered, much stronger than the static magnetic fields obtainable in laboratories with ordinary electromagnets. B. N. Samoilov [7] in 1959, the first to perform a measurement of the hyperfine magnetic field, discovered $H_{Fe}(\mathrm{Au}) \approx 100$ T for Au ions diluted in a Fe host, using the low temperature nuclear orientation technique. Since then extensive works have been carried out, many target elements have been tested using different probes. As the knowledge of these hyperfine fields grew, more successful experiments were set-up. In 1976 G. H. Fuller compiled the first dedicated compilation of magnetic moments. In 1988, the first Table of Nuclear Moments by P. Raghavan [8], contained about 1300 entries of excited and ground states. The most recent Table [9], compiled by N. J. Stone in 2005, contains about 1500 entries.

1.2.1 The physics of magnetic moments

The magnetic moment of a particular nuclear state is related to the moments of the i constituents:

$$\mu = \sum \mu_i \qquad \text{with} \qquad \mu_i = g_l^i \boldsymbol{l}_i + g_s^i \boldsymbol{s}_i \tag{1.1}$$

where g_l and g_s are the orbital and spin gyromagnetic factors, respectively. The orbital g-factors, for protons and neutrons, are $g_l^\pi = \mu_N$ and $g_l^\nu = 0$. Being fermions, with spin $\frac{1}{2}\hbar$, one would expect $g_s^\pi = 2$ and $g_s^\nu = 0$ for protons and neutrons, respectively. Instead, experimentally it was found that for free particles $g_s^\pi = 5.5845$ and $g_s^\nu = -3.8263$. This deviation from the expected values shows that the proton and the neutron are not fundamental particles, i.e. they are made out of other, more *elementary*, constituents,

the *quarks*. In principle, it is possible to use directly quarks in *ab initio* calculations, but reality shows that those models are useful only in a minority of cases, in the lightest nuclei where the complexity is not too high.
It should be remarked that the difference in sign of the two g-factors makes them particularly sensitive to the structure of nuclear states. In the next paragraph it will be shown that this difference can give significant indications on the composition of the wave function, showing if it is dominated by proton or neutron contribution.

The magnetic moment μ of a state $\mid IM\rangle$ is defined as the expectation value of the z component of the operator $\boldsymbol{\mu}$ in the substate of maximum z projection

$$\mu = \langle IM \mid \boldsymbol{\mu}_z \mid IM\rangle_{M=I}. \tag{1.2}$$

The magnetic moment is related to the gyromagnetic factor by the relation

$$\mu = gI \tag{1.3}$$

where I is measured in $[\hbar]$ and μ in *nuclear magneton* $[\mu_N]$.

1.2.2 Extreme single-particle model: odd-mass nuclei

In the extreme single-particle model an odd-mass nucleus can be imagined as constituted by an unpaired nucleon that orbits around an inert core. The nuclear properties will be determined by the unpaired nucleon. In this model the magnetic moments can be calculated coupling the orbital l and spin s momenta to form the total angular momentum j with the relation $j = l \pm s$. The magnetic moments can be calculated from 1.1

$$\mu = \begin{cases} (j-\frac{1}{2})g_l + \frac{1}{2}g_s & \text{for} \qquad j = l + \frac{1}{2} \\ \frac{j}{j+1}((j+\frac{3}{2})g_l - \frac{1}{2}g_s) & \text{for} \qquad j = l - \frac{1}{2}. \end{cases} \tag{1.4}$$

Substituting the experimental values of the g-factors

$$\begin{aligned} g_l^\pi &= 1 \quad g_s^\pi = +5.5845 \\ g_l^\nu &= 0 \quad g_s^\nu = -3.8263 \end{aligned} \tag{1.5}$$

in 1.4 we obtain the so called *Schmidt values*, usually plotted as function of j (fig.1.1). The extreme single-particle model could be imagined as a good representation of those nuclei that have a single valence nucleon (particle or hole) around a double magic core. When it comes to comparing the experimental values to the Schmidt values, however, we observe that usually they tend to fall in between the two Schmidt values. This certainly is a sign of the crudeness of the model, which is missing the interaction between the core

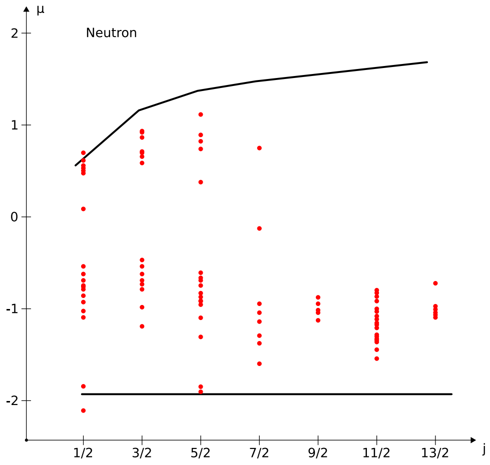

FIGURE 1.1: Calculated and experimental magnetic moments μ versus the total angular momentum j for neutron-odd nuclei. The solid lines shows the Schmidt values from 1.4. The dots are experimental points.

and the particle. The first and most important reason to account for this deviation is the effect of configuration mixing, as explained in ref. [10, 11] by Arima and Horie. Also, the experimental values in Eq. 1.5 are measured for bare protons and neutrons, while the g-factor in the nucleus, where the nucleons are interacting, is different, suggesting that the effect of mesonic exchange currents is important. Lastly, we considered the nucleons and the core completely inert while interactions between them (and between nucleons as well, if they are more than one) should not be neglected.

1.2.3 Extension to more than one extreme-particle

Let's consider a nucleus composed of an inert core and two nucleons. All the particles in the core are coupled such that its total angular momentum is 0. The total angular momentum of the nucleus is then determined by the momenta of the two nucleons, $\boldsymbol{I}'$ and $\boldsymbol{I}''$. The total angular momentum is the sum of these two momenta $\boldsymbol{I} = \boldsymbol{I}' + \boldsymbol{I}''$. The magnetic moment of the state is the expectation value of the operator $\boldsymbol{\mu}$, Eq. 1.2, in the substate of maximum angular moment projection. If we substitute in Eq. 1.2 the total angular momentum $\boldsymbol{I}$ and the relation 1.3 we obtain the expectation value for the magnetic moment of the nucleus

$$\mu = \langle IM \mid g' I'_z + g'' I''_z \mid IM \rangle_{M=I} \tag{1.6}$$

where g' and g'' are the g-factors of the two nucleons. This equation can be rewritten using the generalized Landé formula in the form

$$\mu = \frac{\langle IM \mid g'\boldsymbol{I}' \cdot \boldsymbol{I} + g''\boldsymbol{I}'' \cdot \boldsymbol{I} \mid IM\rangle_{M=I}}{I(I+1)} \langle IM \mid I_z \mid IM\rangle_{M=I} \tag{1.7}$$

from which derives

$$g = \frac{\langle IM \mid g'\boldsymbol{I}' \cdot \boldsymbol{I} + g''\boldsymbol{I}'' \cdot \boldsymbol{I} \mid IM\rangle_{M=I}}{I(I+1)}. \tag{1.8}$$

The evaluation of $\boldsymbol{I}^{','' } \cdot \boldsymbol{I}$ is performed the usual way:

$$\boldsymbol{I}^2 = (\boldsymbol{I}' + \boldsymbol{I}'')^2 = \boldsymbol{I}'^2 + 2\boldsymbol{I}' \cdot \boldsymbol{I}'' + \boldsymbol{I}''^2 \tag{1.9}$$

from which follows

$$\boldsymbol{I}' \cdot \boldsymbol{I}'' = \tfrac{1}{2}(\boldsymbol{I}^2 - \boldsymbol{I}'^2 - \boldsymbol{I}''^2) \tag{1.10}$$

that put into

$$\boldsymbol{I}^{','' } \cdot \boldsymbol{I} = \boldsymbol{I}^{','' } \cdot (\boldsymbol{I}' + \boldsymbol{I}'') = \boldsymbol{I}^{','' 2} + \boldsymbol{I}' \cdot \boldsymbol{I}'' \tag{1.11}$$

gives

$$\boldsymbol{I}^{','' } \cdot \boldsymbol{I} = \tfrac{1}{2}(\boldsymbol{I}^2 + \boldsymbol{I}^{','' 2} - \boldsymbol{I}^{'','2}). \tag{1.12}$$

Substituting the expectation values $\boldsymbol{I}^2 = I(I+1)$ in the equation, the expectation value for the g-factor is

$$g = \frac{g'[I(I+1) + I'(I'+1) - I''(I''+1)]}{I(I+1)} + \frac{g''[I(I+1) + I''(I''+1) - I'(I'+1)]}{I(I+1)} \tag{1.13}$$

which can be written as

$$g = \frac{1}{2}(g' + g'') + \frac{1}{2}(g' - g'')\frac{I'(I'+1) - I''(I''+1)}{I(I+1)}. \tag{1.14}$$

This relation is usually called the *additivity relation*.

It is worth noting that if the two nucleons occupy two levels with the same g-factors the second part of the equation vanishes. The g-factor of that configuration will then be independent of the total spin to which the two particles are coupled.

1.2.4 Collective structure

When the behavior of a nucleus is not well described in terms of singe-particle excitations, for example when there are a few valence particles, an approach to the problem is to suppose that the nuclear states can be described with a combination of single particle states, that is, that the wave function is a linear combination of single particle states.

For example, the first excited state of $^{70}_{30}\mathrm{Zn}_{40}$ could be represented by

$$\psi(2^+) = a\psi(\pi p_{3/2} \oplus \pi p_{3/2}) + b\psi(\nu p_{1/2} \oplus \nu p_{3/2}) + c\psi(\nu p_{1/2} \oplus \nu g_{9/2}) + \dots \tag{1.15}$$

where the parameters $a, b, c \dots$ are chosen such to represent the properties of the states, like the excitation energy, the magnetic moment and the quadrupole moment, and the operator $\oplus$ suppose that the angular momentum coupling is such that the resultant state is a 2^+ state.

In general, some states can be well described not by the motion of few valence nucleons but of the whole nucleus. These states are called *collective states*. Analyzing the properties of the nuclides it is possible to distinguish two regions that exhibit such behavior, $A < 150$ and $150 < A < 190$. The first region is generally described in a frame of vibrational motion around a spherical equilibrium shape and the second one with rotations of a non-spherical system. Patterns can be predicted: in both cases, the ground state present 0^+ spin-parity and the first excited state is a 2^+ state. For the vibrational states, at higher energy we have a triplet of 0^+, 2^+ and 4^+ states. The rotational band instead have the spins restricted to even values of I, so the 2^+ state is followed by a 4^+ state which is followed by a 6^+ state and so on. The energy spacing in a rotational band follow a quadratic progression on I. The magnetic moments are expected to be $I(Z/A)$, so for the first excited state the g-factor is Z/A. This limit is called *hydrodynamical limit* [12] because in the collective model the nucleus can be imagined like a liquid drop of incompressible nuclear matter.

The collective model was developed at the same time with the early shell-model, by the wedding of Gamow's liquid-drop model and Bohr's compound nucleus. Its formalization dates to 1936 by Breit and Wigner [13]. The success of this model completely overshadowed the shell-model, which was forgotten for more than ten years, till 1949. In fact already in 1939 the liquid-drop model explained the phenomenon of the nuclear fission of the heavy nuclei. Some more details about this model are given in the historical introduction to the shell model in Chap. 2.1.

It is worth noting that in some cases the wave function could be composed by many single particle states, one of which is predominant. In such case we assist to a coupling between collective and the single-particle state.

1.2.5 Measurement techniques

There are many techniques to measure magnetic moments. Each of them suits a particular set of characteristics of the nuclear state to be studied. The main constraint is the half-life of the state that can span from $10fs$ to infinity. Important as well are the spin (from $\frac{1}{2}\hbar$ up to $36\hbar$ for ^{154}Dy) and the population and decay mechanism of the state,

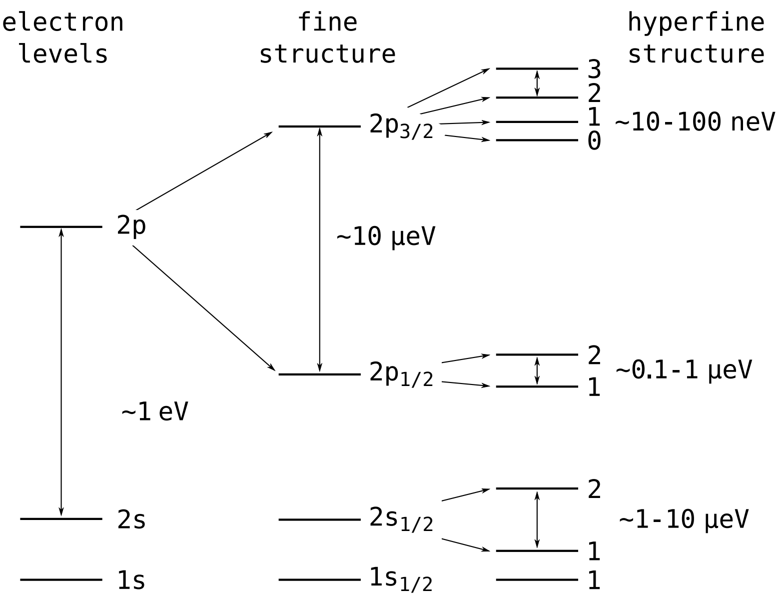

FIGURE 1.2: The electron degeneracy on the angular momentum J (leftmost column) is resolved by the $l - s$ spin-orbit coupling, generating the fine structure (central column). The interaction of J with the nuclear angular momentum results in the total spin F, which spans in the range $|I - J| < F < |I + J|$, and generates the hyperfine structure (rightmost column). The difference in energy between the split levels of the hyperfine structure is proportional to the nuclear magnetic moment.

the chemical properties of the element, etc.

For all the techniques there are two constant requirements: a) an ensemble of oriented nuclear states and b) a magnetic field. There are many ways to get a spin-orientation of the products we want to measure. It can be induced directly in the reaction mechanism (fusion-evaporation is well known to produce a substantial amount of orientation, as well as fragmentation if a proper condition on momentum distribution is imposed), the use of polarized beams to obtain polarized products. After the production, the orientation can be induced with "brute force" (BFO, which consists in cooling down the nuclei and applying a strong magnetic field, resolving the degeneracy on the total angular momentum and allowing only for the population of the state of the multiplet with lowest energy). The magnetic field may have different origins: it can be an external field generated by a magnet (up to few tesla for superconducting magnets) or a microscopical field generated by static (up to 1kT) or transient(up to few kT) hyperfine interaction.

Once the oriented ensemble is interacting with the magnetic field, two observable can be measured:

- the interaction energy due to the Zeeman effect;
- the precession of the magnetic moment's axis, hence of the angular distribution.

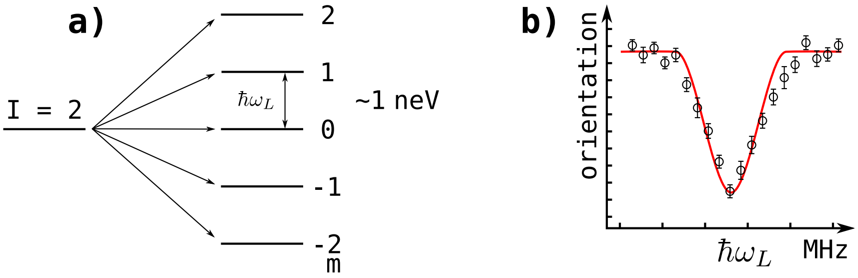

FIGURE 1.3: Zeeman effect. *a)* The interaction between the nuclear momentum and an external magnetic field induces a splitting of the order of neV. *b)* This quantity can be measured adding a radio frequency (RF) magnetic field: when the frequency of the RF matches the resonance frequency, the orientation of the spin ensemble is lost.

The interaction energy $\Delta E = \vec{\mu} \cdot \vec{H}$ can be measured using Mössbauer spectroscopy techniques, which leads to a precision measurement of both the magnetic moment and the hyperfine field. The limitation is that only low-energy states are accessible. Stable nuclei can be studied in atomic beam experiments, beta emitters using BFO and in β-NMR. These three techniques are based on the hyperfine splitting of the nuclear structure. In fig. 1.2 we can observe that the degeneracy of the electronic structure in J is resolved by the coupling between the orbital and spin angular momenta, generating what is called *fine structure*. When the electronic momentum J interacts with the nuclear spin I, each level is further split according to its total spin F. This is called *hyperfine structure*. The strength of the splitting is proportional to the nuclear magnetic moment. Its measurement is performed using different laser techniques.

If a level is interacting with a magnetic field, another much weaker splitting takes part. This effect is called *Zeeman effect* and is depicted in fig. 1.3. The energy splitting is function of the magnetic moment and for magnetic fields of the order of the Tesla it is typically of the order of the neV. Due to the difference in energy the substates will not be equally populated. This polarization will affect the angular distribution of the decay radiation, which will show a certain degree of anisotropy. The principle of the nuclear magnetic resonance is to add a radio frequency (RF) magnetic field perpendicular to the static magnetic field. When the frequency of this RF magnetic field will match the nuclear frequency of the transition, the orientation will be lost due to the induced transitions. The frequency of the RF field is typically around 1 MHz. The resonance frequency can be determined measuring the orientation as a function of the RF frequency.

The measurement of the Larmor precession effect accounts for the great part of the experiments. The interaction of the magnetic moment $\vec{\mu}$ with a magnetic field $\vec{B}$ results in a torque $\vec{\tau}$

$$\vec{\tau} = \vec{\mu} \times \vec{B} = \frac{d\vec{j}}{dt}. \tag{1.16}$$

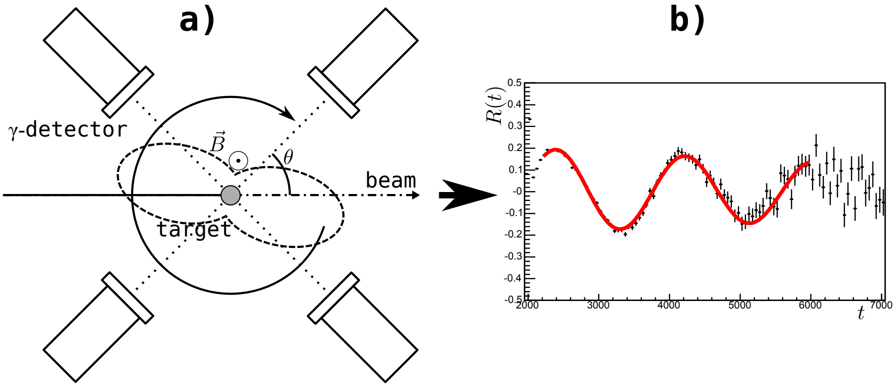

FIGURE 1.4: Time differential perturbed angular distribution technique. *a)* typical set-up, *b)* $R(t)$ function.

The effect of this torque is to make the angular momentum j precess about the magnetic field direction with a frequency proportional to the magnetic field strength and to the g-factor

$$\omega_L = -\frac{\mu_N}{\hbar} g B \tag{1.17}$$

ω_L is called the *Larmor frequency.*

1.2.6 Time Differential Perturbed Angular Distribution/Correlation (TDPAD/TDPAC)

For relative long lived states, from hundreds of ns up to μs, the angular distribution can spin a few times after the production, giving high precision measurements. In fig. 1.4 *a)* is presented a typical setup: the beam impinges on a target and the state of interest is populated. It is left decaying in an environment with no perturbations other than the applied magnetic field $\vec{B}$, which has a typical magnitude of 10 mT - 1 T and is provided by electromagnet or permanent magnets.

This technique can be applied to states with lifetimes down to few ns using the hyperfine magnetic fields, much stronger than the macroscopic fields. For a particular detector positioned at an angle θ, gating on the energy of interest we get the intensities as a function of the time $I(t;\theta)$ which will have an oscillating behavior superimposed on the exponential decay. The function $R(t)$ in *b)* is constructed in the following way

$$R(t) = \sqrt{\frac{I(t;\theta) - I(t;\theta + 90°)}{I(t;\theta) + I(t;\theta + 90°)}} \tag{1.18}$$

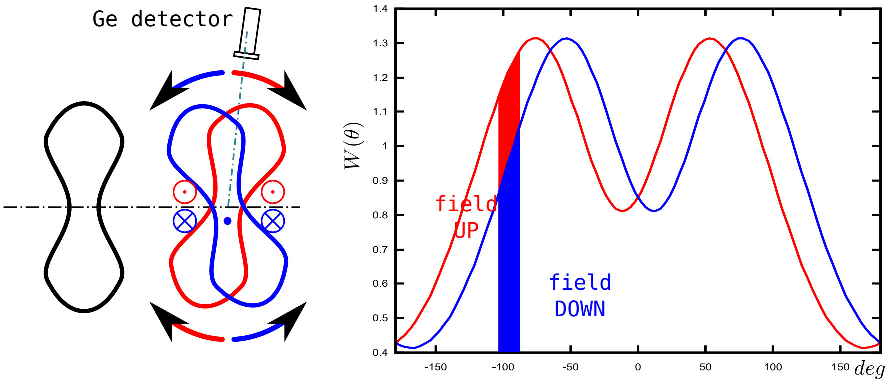

FIGURE 1.5: Principles of the IPAD technique. On the left, the angular distribution is shifted of an angle $\pm\Delta\theta$, in a direction or the other depending on the magnetic field direction. On the right the angular distributions $W(\theta \pm \Delta\theta)$ are plotted. The shaded area is the angular coverage of the γ-ray detector. The difference between the two intensities is proportional to the magnetic moment.

where the double ratio eliminates the exponential decay of the line. The resulting function is oscillating with a frequency ω_L proportional to the magnetic moment. The experimental function $R_{exp}(t)$ is fitted with a general function of the form

$$R_{theo}(t) = Ae^{-\lambda t} \sin(\omega_L t + \theta) \tag{1.19}$$

to get the value of ω_L. The exponential decay of the amplitude of the oscillation is due to the relaxation of the orientation of the spin ensemble and it varies from case to case, depending on the characteristic of the projectile, on the target's crystal, on the defects in the lattice. If the relaxation time is long, compared to the state life-time, the term in Eq. 1.19 can be omitted. If it is short, the experiment cannot be performed and another target material, if possible, must be chosen.

The strength of this technique is the precision achievable when the $R(t)$ function has the time to perform several oscillations.

The name of the technique refers to the different way the θ angle is measured: if with respect to a fixed angle we have a *distribution* and the technique is called TDPAD, while if the angle is measured between the two events of a γ-particle/γ-γ *coincidence* the name is TDPAC.

1.2.7 Integral Perturbed Angular Distribution (IPAD)

In this technique, the magnetic field interacts with the excited nuclide for a time interval Δt causing a precession of an angle $\Delta\theta$

$$\Delta\theta = -g\frac{\mu_N}{\hbar}B\Delta t. \tag{1.20}$$

This precession angle is well below a complete 2π rotation: with a typical g-factor of 0.3 and an interaction interval of few ps we need very strong magnetic fields to have an appreciable precession angle. From eq. 1.20 we see that for $\Delta\theta \approx 10$ mrad we need a field of 1 kT. Such intense fields can be obtained with the transient hyperfine interaction, as will be explained in section 1.4.

The target is usually surrounded by pairs of detectors positioned symmetrically with respect to the beam direction. A particle detector is used for the identification of the particles emitted and for the determination of their angle of emission. The correlation is performed between the particle emitted during the production of the state and the γ-ray emitted in its de-excitation.

In the absence of magnetic field, the angular distribution of the emitted radiation is $W(\theta)$, as defined in sect. 1.3. If the excited state interacts with the magnetic field, the angular distribution rotates with an angle $\Delta\theta$, and the angular distribution becomes $W(\theta \pm \Delta\theta)$, where the sign depends on the magnetic field direction. Usually in these experiments the magnetic field is perpendicular to the plane defined by the γ-ray detectors and is provided by the transient field. The transient field has its origins in the hyperfine interaction between the projectiles and the electrons of a ferromagnetic target, polarized by an electromagnet. The transient field is parallel to the external magnetic field used for the polarization, so reversing the current's directions in the electromagnet means to change the direction of the transient magnetic field. Figure 1.5 makes evident the mechanism of the technique: if the γ-detector is not moved, changing the magnetic field direction will result in different intensity of the photopeak. Combining measurements taken with different magnetic field direction allows for the determination of this difference, which is proportional to the precession angle.

It is possible to show that

$$\Delta\theta = \epsilon/S \tag{1.21}$$

where ϵ is the *asymmetry* and the *slope* S – the logarithmic derivative of the angular distribution

$$S = \frac{1}{W(\theta)}\frac{dW(\theta)}{\theta}\bigg|_{\theta_\gamma} \tag{1.22}$$

calculated at detection angle θ_γ in the rest-reference frame of the nucleus. The asymmetry ϵ is defined:

$$\epsilon = \frac{1-\rho}{1+\rho} \tag{1.23}$$

where the double ratio ρ is written as

$$\rho = \sqrt{\frac{N(\theta_\gamma, \uparrow)N(-\theta_\gamma, \downarrow)}{N(-\theta_\gamma, \uparrow)N(\theta_\gamma, \downarrow)}} \tag{1.24}$$

and it is a function only of the number of counts in the photopeak per magnetic field direction (↑ and ↓) and detection angle θ_γ, i.e. it is independent of detector efficiencies and beam current variations throughout the measurement.

It should be pointed out that the measurement could be carried out with only one detector, but a multi-detector set-up is preferable to obtain a higher total efficiency (higher statistic) and to get rid of some systematic errors. In fact, changing the field direction at a fixed interval of time (typically every 1-10 minutes) and using detectors in symmetric pairs allows to get rid of sources of error like the efficiency of each detector $\epsilon_{1,2}$, the beam current changes during each field direction $I_{\uparrow,\downarrow}$ and differences in the switching interval $T_{\uparrow,\downarrow}$. Taking into account all the terms, the double ratio is written

$$\begin{aligned} \rho &= \sqrt{\frac{\epsilon_1 I_\uparrow T_\uparrow N(\theta_{\gamma 1}, \uparrow) \times \epsilon_2 I_\downarrow T_\downarrow N(\theta_{\gamma 2}, \downarrow)}{\epsilon_2 I_\uparrow T_\uparrow N(\theta_{\gamma 2}, \uparrow) \times \epsilon_1 I_\downarrow T_\downarrow N(\theta_{\gamma 1}, \downarrow)}} \\ &= \sqrt{\frac{\epsilon_1 I_\uparrow T_\uparrow \epsilon_2 I_\downarrow T_\downarrow \times [N(\theta_{\gamma 1}, \uparrow)N(\theta_{\gamma 2}, \downarrow)]}{\epsilon_2 I_\uparrow T_\uparrow \epsilon_1 I_\downarrow T_\downarrow \times [N(\theta_{\gamma 2}, \uparrow)N(\theta_{\gamma 1}, \downarrow)]}} \end{aligned} \tag{1.25}$$

which simplifies to eq. 1.24.

It is also important to notice that for a successful measurement, the γ-ray detectors' position should be carefully chosen, i.e. maximizing the observed asymmetry through positioning them at the maximum of the slope.

1.2.8 Recoil in vacuum/gas (RIV/RIG) and other techniques

The hyperfine interaction is used also for ions recoiling in vacuum or gas (RIV/RIG) or emerging from thin foils tilted respect to the beam direction [14]. In the RIV technique the hyperfine field is not polarized in a particular direction but presents an isotropic distribution. The damping of the amplitude of the angular distribution is proportional to the g-factor and the interaction time. This promising technique is currently being explored by Stuchbery and Stone [15].

The tilted foils technique aims to polarize the excited states by making them traverse several targets. The polarization is given only by surface effects, so many thin layers are

used. The target used are made of carbon with a thickness of few μg/cm^2. At present Hass *et al.* [16] are exploring this technique at ISOLDE.
If the short lived state can be populated from a long-lived one, it can be possible to implant the latter in a ferromagnetic host and wait for its decay, as pioneered by Stuchbery [17].
Stone, in his compilation of nuclear moments [9], lists more than eighty techniques and variations, each applicable to a particular set of state's conditions.

1.3 Coulomb excitation

To produce the excited states, one of the most interesting mechanisms that can be used is Coulomb excitation. Its cross section is usually much higher compared to other nuclear reactions like single - and multi-nucleon transfer, fission or fusion-evaporation, and, with relativistic-energy beams, states of higher collectivity can be accessed.
In the early 1930's nuclear reactions started being explored using the newly developed particle accelerators. In 1928, Widerøe [18] designed the first linear accelerator. Within a few years the cyclotron and electrostatic machines became available to the nuclear physicists. With the former, Lawrence in 1931 was able to accelerate Hg ions up to MeV energies. The same year Van De Graaf built a machine able to reach 1 MV and the machine that bears his name, together with the Tandem improvement, became the most popular electrostatic machine in nuclear physics laboratories.
Following the intuitions of Rutherford, Chadwick and Ellis [19], in the very beginning of this accelerator era, Landau [20] and Weisskopf [21] perceived the possibility of using long range electric interaction for nuclear excitation, but only in 1939 was this phenomenon experimentally observed. Barnes [22] populated the first excited level of ^{115}In, a long lived isomer, using a mechanism that was later on identified as Coulomb excitation. The theoretical development [23] that followed led to a better understanding of the mechanism. Remarkably, a classical approach was giving good agreement with experiments. It was also pointed out that the levels populated with Coulomb excitation were low energy collective states, which made this technique particularly suitable for the study of collective motions.
With the technical development of particle accelerators, it is nowadays possible to reach relativistic energies ($>$ 100 MeV/A) for the bombarding ions. Far from being obsolete, the Coulomb excitation is used to populate states up to 10-20 MeV [24], retaining all its predictability.

1.3.1 Theoretical background

Theory distinguishes three different regimes that require a different approach, depending on the energy of the projectile. In a semiclassical frame, the interaction is characterized by the *Sommerfeld parameter*

$$\eta = \frac{Z_1 Z_2}{v}\frac{e^2}{\hbar} \tag{1.26}$$

where Z_1 and Z_2 are, respectively, the atomic number of the projectile and of the target nuclei and v the velocity of the projectile. If $\eta \gg 1$, the electromagnetic interaction is strong enough to prevent the charge distributions of the two nuclei from overlapping and the interaction that takes part between the projectile and the target is purely electromagnetic. This is the case of low bombarding energies (low in relation to the Coulomb barrier). If the energy loss during the interaction is small, the projectile is moving along a hyperbolic Rutherford trajectory in the field generated by the target nucleus. The excitation probability from an initial state i to a final one f is then given by

$$\left(\frac{d\sigma}{d\Omega}\right)_{CoulEx} = \left(\frac{d\sigma}{d\Omega}\right)_{Ruth} P_{i\to f} \tag{1.27}$$

where $(d\sigma/d\Omega)_{Ruth}$ is the differential Rutherford cross section and

$$P_{i\to f} = \frac{1}{(2I_i+1)}\sum_{M_i M_f} |b_{if}|^2 \tag{1.28}$$

the probability of inducing a transition, without considering the orientation of the states. The excitation cross section can be described by the same matrix elements that are describing the electromagnetic decay with the emission of γ radiation, via the expansion in multipoles. The transition amplitudes b_{if}, the probability of having an excitation, are small for a single event so the problem is usually handled using time-dependent perturbation theory, e.g. [25]. At first order we have

$$b_{if} = \frac{1}{i\hbar}\int_{-\infty}^{\infty} e^{i\omega t} dt \langle f \mid \mathcal{H}(t) \mid i\rangle \tag{1.29}$$

where $\mathcal{H}(t)$ is the interaction Hamiltonian and $\omega = (E_f - E_i)/\hbar$ the *nuclear frequency* of the transition. Considering a pure electric interaction the Hamiltonian is written

$$\mathcal{H}_E(t) = \int \rho\vec{r}\varphi(\vec{r},t)dr \tag{1.30}$$

where $\rho\vec{r}$ is the nuclear density charge operator and $\varphi(\vec{r},t)$ the Coulomb potential

$$\varphi(\vec{r},t) = \frac{Z_1 e}{|\vec{r}-\vec{r}_p(t)|} - \frac{Z_1 e}{\vec{r}_p(t)} \tag{1.31}$$

with $\vec{r}_p(t)$ the projectile position. A multipole expansion of the potential leads to

$$\mathcal{H}_E(t) = 4\pi Z_1 e \sum_{\lambda=1}^{\infty} \sum_{\mu=-\lambda}^{\lambda} \frac{1}{2\lambda+1} \vec{r}_p^{\,-\lambda-1} Y_{\lambda\mu}(\theta_p, \phi_p) \mathcal{M}^*(E\lambda, \mu) \tag{1.32}$$

where, assuming k point-like charges, the multipoles can be written

$$\mathcal{M}(E\lambda, \mu) = \sum_k e_k \vec{r}_k^{\,\lambda} Y_{\lambda\mu}(\theta_k, \phi_k) \tag{1.33}$$

with e_k and $\vec{r}_k$ the charge and the position of the k-th nucleon and $Y_{\lambda\mu}(\theta, \phi)$ the normalized spherical harmonics with origin in the center of mass and a fixed direction for the polar axis.
With eq. 1.32 the equation 1.29 becomes

$$b_{if} = \frac{4\pi Z_1 e}{i\hbar} \sum_{\lambda\mu} \frac{1}{2\lambda+1} \langle I_i M_i \mid \mathcal{M}(E\lambda, \mu) \mid I_f M_f \rangle S_{E\lambda,\mu} \tag{1.34}$$

where

$$S_{E\lambda,\mu} = \int_{\infty}^{\infty} e^{i\omega t} Y_{\lambda\mu}(\theta_p(t), \phi p(t)) \vec{r}_p(t)^{-\lambda-1} dt \tag{1.35}$$

are called *orbital integrals* and where the dependency of the initial $\langle i \mid$ and final $\mid f \rangle$ states on the total angular momentum I and its projection M is shown explicitly.

This formula holds when the main sources of interaction are the electric fields of the projectile and the target nuclei. This is true for low velocity where the magnetic fields generated by the moving charged particles are of second order and the transitions generated by the magnetic multipoles are orders of magnitude less probable than the corresponding electric ones. While in the radiative multipole expansion the magnitude of the electric and magnetic fields are equal, the ratio between the magnetic and electric field strength is v/c, so the magnetic excitation is reduced by a factor of $(v/c)^2$ with respect to the electric one. In figure 1.6 we have the theoretical excitation cross sections for Coulomb excitations of different multipole orders for protons bombarding a nucleus with $Z = 50$ and $A = 120$ and a transition energy of 200 keV. The figure is taken from Alder [25] p. 440. The experimental evidence points out that the strength of the $E1$ transition is much smaller than the one showed in the figure, and on the contrary, the $E2$ transitions are much more important. For these reasons, electric quadrupole transitions are of particular interest in the theory of Coulomb excitation and indeed they are the most frequently observed. Still, the transitions have to respect the selection rules and if an electric transition is forbidden, it is possible to observe transition of different order.

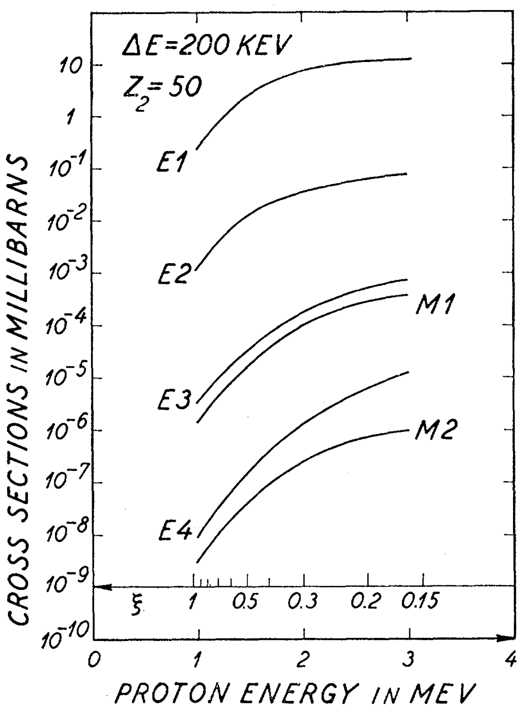

Figure 1.6: Theoretical excitation cross sections for a proton projectile and a $Z = 50$, $A = 120$ target as function of the proton energy. The energy of the transition is assumed to be 200 keV. The figure is taken from from Alder [25] p. 440.

Low-energy Coulomb excitation (few MeV/nucleon) has been used for many years to study nuclear structure of stable nuclei. On the other extreme at relativistic energies, around 300 MeV/nucleon, when η is much smaller than one, the interaction produces only a small distortion of the projectile wave. The trajectory of the projectiles can be described as straight lines. The relativistic retardation effect makes the interaction stronger than the one in the low energy case. Therefore, with the relativistic Coulomb excitation, states with energies up to 10/20 MeV are readily accessible, making Coulomb excitation a useful tool to study giant resonances. To make sure that the interaction is purely electromagnetic, we can limit our observation to very forward angles, corresponding to impact parameters larger than the sum of the radii of the two colliding ions. Such selection is performed in order to avoid violent nuclear reactions for which the angular distribution is not known with the same precision as in Coulomb excitation but only approximately. A detailed discussion can be found in ref. [26], which shows that it is possible to separate the interaction in electric and magnetic multipole contributions like in the non-relativistic case. Experimentally, the idea is to accelerate the nucleus of interest, to scatter it off a heavy target and detect the gamma radiation from the de-excitation in coincidence with the scattered particles. Because of the high energy of the projectile, the target can be very thick (500 mg/cm^2) resulting in a high excitation probability.

At intermediates energies, the situation is more complicated because the theory has to take into account both the bending of the trajectories typical of the low-energy regime and of the relativistic retardation effect. Having a reliable theory is very important because of the possibilities given by the radioactive beam facilities. When the nuclide of interest is produced in fragmentation and in-flight separation, the energy of the projectile is typically in the range of 30-300 MeV/nucleon ($v/c \approx 0.25 - 0.65$), which falls in the intermediate energy range. It has been shown that both low energies and relativistic approaches are not working in this range of energies, and a new theoretical framework has been established [27]. Like in the relativistic case, the experiments are carried out in inverse kinematics and the use of thick targets partially compensates for the lower beam intensity that is usually available with radioactive beams.

We will focus on Coulomb excitation at intermediate energies because in the two experiments that are the object of our work, the state of interest was populated using this mechanism. The scattered particles are usually detected with an annular detector. Using a segmented particle detector, we studied the effect that a selection on the azimuthal angle ϕ_P (fig.1.7 for details) would have on the angular distribution, looking for a better definition of the angular distribution.

The important quantities of an intermediate-energy Coulomb excitation experiment were calculated using the already cited ref.[27] and the code COULINT developed by C. A. Bertulani [24], who has in all cases considered a cylindrical particle detector. The theory and the code developed by A. E. Stuchbery [28] predicts the effect of breaking such azimuthal symmetry.

In fig.1.7 the reference frame that has been used for the calculations is presented. The z-axis is parallel to the beam direction and the x-axis is lying in the plane defined by the γ-ray detectors, coinciding with $\phi_P = 0$. The y-axis usually corresponds to the direction of the magnetic field. In this reference frame the angular distribution (ref.[25] eq. II.A.66 for details) is written

$$W(\theta_p, \phi_p, \theta_\gamma, \phi_\gamma) = \sum_{kq} a^\lambda_{kq}(\theta_p, \phi_p, \xi) A^{(\lambda)}_k Y_{kq}(\theta_\gamma, \phi_\gamma) \tag{1.36}$$

where θ_p, ϕ_p and $\theta_\gamma, \phi_\gamma$ are the coordinates of the emitted particle and γ-radiation, respectively, and

$$a^\lambda_{kq}(\theta_p, \phi_p, \xi) = \frac{b^\lambda_{kq}(\theta_p, \phi_p, \xi)}{b^\lambda_{00}(\theta_p, \phi_p, \xi)}. \tag{1.37}$$

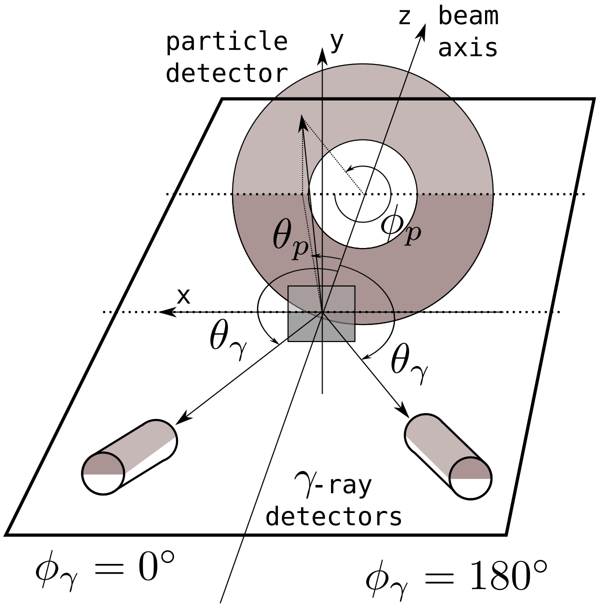

FIGURE 1.7: The reference system. The z-axis is chosen to be parallel to the beam direction. The x-axis ($\phi_P = 0$) is lying horizontally in the γ-ray detectors' plane. The coordinates of the γ-ray are $(\theta_\gamma, \phi_\gamma)$ and the ones of the particle (θ_p, ϕ_p).

Considering only the electric multipoles, the angular distribution coefficients $b^{E\lambda}_{kq}(\theta_p, \phi_p, \xi)$ are written

$$b^{E\lambda}_{kq}(\theta_p, \phi_p, \xi) = -\frac{1}{\sqrt{2k+1}} \begin{pmatrix} \lambda & \lambda & k \\ 1 & -1 & 0 \end{pmatrix}^{-1} \sum_{\mu\mu' q'} (-1)^{\mu} \begin{pmatrix} \lambda & \lambda & k \\ \mu & \mu' & q' \end{pmatrix}$$
$$\times Y_{\lambda\mu}(\frac{\pi}{2}, 0) Y_{\lambda\mu'}(\frac{\pi}{2}, 0) I(E\lambda, \mu) I(E\lambda, \mu') D^{k}_{q'q}(\frac{\pi}{2} + \frac{\theta_p}{2}, \frac{\pi}{2}, \phi_p - \frac{\pi}{2}). \tag{1.38}$$

The Wigner 3-j symbol formalism was used. $I(E\lambda, \mu)$ are the orbital integrals and $Y_{kq}(\phi, \theta)$ the spherical harmonics.

At low energies and in direct kinematics, if the measurement is performed without detecting the emitted particles, the formula 1.38 is integrated over the particle angles θ_p and ϕ_p to obtain the total cross section. At intermediate and relativistic energy a selection is imposed on the detection angle θ_p of the scattered particles, and this limits the integrals to a specific range.

1.3.2 Circular particle detector

In case of a ring detector, characterized by azimuthal symmetry, we have a fixed θ_p range and the only dependency from ϕ_p is coming from the rotation matrix $D^{k}_{q'q}(\frac{\pi}{2} + \frac{\theta_p}{2}, \frac{\pi}{2}, \phi_p -$

$\frac{\pi}{2}$). We need to integrate over the whole ϕ_p angle interval $(0, 2\pi)$. The integral to be evaluated is

$$\int_0^{2\pi} D^k_{q'q}(\alpha, \beta, \phi) d\phi = D^k_{q'q}(\alpha, \beta, 0) \int_0^{2\pi} e^{iq\phi} d\phi \tag{1.39}$$

where

$$\int_0^{2\pi} e^{iq\phi} d\phi = \frac{1}{iq}(e^{iq2\pi} - 1) = \delta_{q,0} 2\pi \tag{1.40}$$

with $\delta_{q,0}$ the Kronecker delta.

The rotation matrix can be written in terms of spherical harmonics

$$D^k_{q0}(\alpha, \beta, 0) = \sqrt{\frac{4\pi}{2k+1}} Y_{kq}(\beta, \alpha). \tag{1.41}$$

After the integration and the substitution of the spherical harmonics equation 1.38 becomes

$$\begin{aligned} b_k^{E\lambda}(\theta_p, \xi) = -\frac{4\pi\sqrt{\pi}}{\sqrt{2k+1}} \begin{pmatrix} \lambda & \lambda & k \\ 1 & -1 & 0 \end{pmatrix}^{-1} \sum_{\mu\mu' q'} (-1)^\mu \begin{pmatrix} \lambda & \lambda & k \\ \mu & \mu' & q' \end{pmatrix} \\ \times Y_{\lambda\mu}\left(\frac{\pi}{2}, 0\right) Y_{\lambda\mu'}\left(\frac{\pi}{2}, 0\right) I(E\lambda, \mu) I(E\lambda, \mu') Y_{kq}\left(\frac{\pi}{2}, \frac{\pi}{2} + \frac{\theta_p}{2}\right). \end{aligned} \tag{1.42}$$

These coefficients are evaluated by the GKINT code [29], with the proper integration on θ_p depending on the particle detector set-up, on the target thickness and on the energy loss in the target.

To obtain $W(\theta_\gamma)$ for a particular particle detection solid angle the general angular distribution $W(\theta_p, \phi_p, \theta_\gamma, \phi_\gamma)$ (eq. 1.36) is multiplied by the *differential excitation cross section*. This latter quantity, the probability of having an excitation as function of the scattering angle, can be estimated from the differential form of eq. 1.27

$$d\sigma = d\sigma_R P_{i\to f}. \tag{1.43}$$

The Rutherford cross section is well known

$$d\sigma_R = \frac{1}{4} \left(\frac{Z_1 Z_2 e^2}{m_0 v^2}\right)^2 \frac{1}{\sin^4(\theta_p/2)} d\Omega_p \tag{1.44}$$

with m_0 the reduced mass of the projectile-target nucleus system and Z their atomic numbers. The transition probability $P_{i\to f}$ is defined by eq. 1.28.

With the orthogonality relation

$$\sum_{M_i M_f} \begin{pmatrix} I_i & \lambda & I_f \\ -M_i & \mu & M_f \end{pmatrix} \begin{pmatrix} I_i & \lambda' & I_f \\ -M_i & \mu' & M_f \end{pmatrix} = (2\lambda+1)^{-1} \delta_{\lambda\lambda'} \delta_{\mu\mu'} \tag{1.45}$$

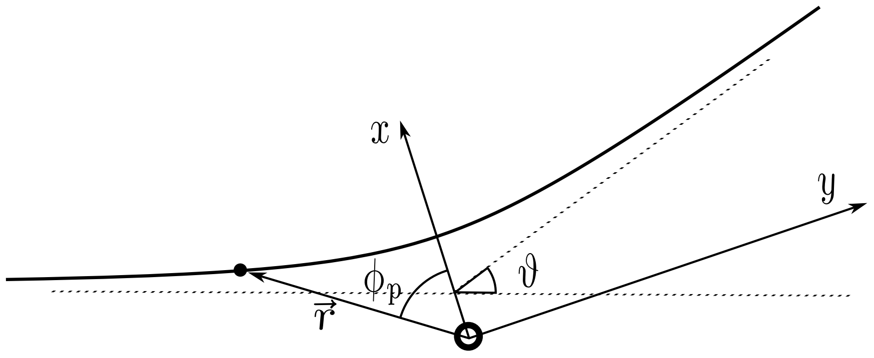

FIGURE 1.8: Focal reference system. The z-axis is pointing into the page. The particle position, defined by $\vec{r}(r_p, \theta_p, \phi_p)$, is in this reference system defined by the Cartesian coordinates $\vec{r}(x_p, y_p, z_p)$. The total deflection angle of the projectile is ϑ.

the differential excitation cross section eq. 1.43 can be written

$$d\sigma = \sum_{\lambda=1}^{\infty} d\sigma_{E\lambda} \tag{1.46}$$

with

$$d\sigma_{E\lambda} = \frac{4\pi^2 Z_1^3 Z_2 e^4}{\hbar^2 m_0 v^2} \frac{1}{\sin^4 \theta/4} \frac{B(E\lambda; I_i \to I_f)}{(2\lambda+1)^3} \sum_{\mu} \mid S_{E\lambda,\mu} \mid^2 d\Omega \tag{1.47}$$

where we have introduced the *reduced transition probability* $B(E\lambda; I_i \to I_f)$ defined as

$$B(E\lambda; I_i \to I_f) = \frac{|\langle I_i \| \mathcal{M}(E\lambda) \| I_f \rangle|^2}{2I_i + 1}. \tag{1.48}$$

This quantity is widely used in nuclear physics and it measures the 'ease' with which a level can be excited or it de-excites. For Coulomb excitation with $I_i = 0$ and $I_f = 2$, the excitation probability is five time bigger than for de-excitation.

The orbital integrals are most easily evaluated in the focal reference frame shown in figure 1.8, where the particle is individuated by (x_p, y_p, z_p) and the $S_{E\lambda,\mu}$ is written

$$S_{E\lambda,\mu} = Y_{\lambda\mu}\left(\frac{\pi}{2}, 0\right) \int_{-\infty}^{\infty} \frac{(x_p + iy_p)^{\mu}}{r_p^{\lambda+\mu+1}} e^{iwt} dt \tag{1.49}$$

with the orbit described by the parametric coordinates

$$x_p = a(\cosh w + \epsilon) \tag{1.50}$$

$$y_p = a\sqrt{(\epsilon^2 - 1)} \sinh w \tag{1.51}$$

$$z_p = 0 \tag{1.52}$$

$$r_p = a(\epsilon \cosh w + 1) \tag{1.53}$$

$$t = \tfrac{a}{v}(\epsilon \sinh w + w) \tag{1.54}$$

where $r_p = |\vec{r}|$ the distance between the two nuclei, v is the velocity of the particle, a is half the distance of the closest approach between projectile and target nucleus

$$a = \frac{Z_1 Z_2 e^2}{m_0 v^2} \tag{1.55}$$

and the *eccentricity* ϵ is related to the total scattering angle ϑ by

$$\epsilon = \frac{1}{\sin\left(\frac{\vartheta}{2}\right)}. \tag{1.56}$$

From the chosen parameterization it follows that $\theta_p = \pi/2$. The orbital integrals can be reduced to

$$S_{E\lambda,\mu} = \frac{1}{va^{\lambda}} Y_{\lambda\mu}\left(\frac{\pi}{2}, 0\right) I_{\lambda\mu}(\vartheta, \xi) \tag{1.57}$$

with

$$I_{\lambda\mu}(\vartheta, \xi) = \int_{-\infty}^{\infty} e^{i\xi(\epsilon \sinh w + w)} \frac{(\cosh w + \epsilon + i\sqrt{(\epsilon^2 - 1)} \sinh w)^{\mu}}{(\epsilon \cosh w + 1)^{\lambda+\mu}} dw \tag{1.58}$$

and the *adiabaticity* parameter ξ defined as

$$\xi = \frac{a\Delta E}{\hbar v} = Z_1 Z_2 e^2 \hbar v \frac{\Delta E}{m_0 v^2}. \tag{1.59}$$

Substituting eq. 1.57 in eq. 1.47 the differential excitation cross section becomes

$$d\sigma_{E\lambda} = \left(\frac{Z_1 e}{\hbar v}\right) a^{-2\lambda+2} B(E\lambda) df_{E\lambda}(\vartheta, \xi) \tag{1.60}$$

where the differential $df_{E\lambda}$ is written

$$df_{E\lambda}(\vartheta, \xi) = \frac{4\pi^2}{(2\lambda+1)^3} \sum_{\mu} \left| Y_{\lambda\mu}\left(\frac{\pi}{2}, 0\right)\right|^2 |I_{\lambda\mu}|(\vartheta, \xi)|^2 \sin^{-4}\left(\frac{\vartheta}{2}\right) d\Omega. \tag{1.61}$$

Finally, multiplying the coefficients $b_k^{E\lambda}(\xi)$ by the differential cross section we have

$$\begin{aligned} b_k^{E\lambda}(\xi) = {} & \frac{1}{\sqrt{2k+1}} \begin{pmatrix} \lambda & \lambda & k \\ 1 & -1 & 0 \end{pmatrix}^{-1} \sum_{\mu\mu'\kappa} (-1)^{\mu} \begin{pmatrix} \lambda & \lambda & k \\ \mu & -\mu' & \kappa \end{pmatrix} \\ & \times Y_{\lambda\mu}\left(\frac{\pi}{2}, 0\right) Y_{\lambda\mu'}\left(\frac{\pi}{2}, 0\right) \int_{\vartheta_{min}}^{\vartheta_{max}} I_{\lambda\mu}(\vartheta, \xi) I_{\lambda\mu'}(\vartheta, \xi) Y_{\lambda\mu'}\left(\frac{\pi}{2}, \frac{\pi}{2} + \frac{\vartheta}{2}\right) \frac{\cos(\vartheta/2)}{\sin^3(\vartheta/2)} d\vartheta \end{aligned} \tag{1.62}$$

where ϑ_{min} and ϑ_{max} are determined by the aperture of the particle detector.

The parameter calculated by the COULINT code is the *statistical tensor* ρ_{kq} defined as

$$\rho_{kq} = F_k(\lambda, \lambda, I_i, I_f) \frac{b_{kq}^{E\lambda}(\theta_p, \phi_p, \xi)}{b_{00}^{E\lambda}(\theta_p, \phi_p, \xi)} \tag{1.63}$$

with $F_k(\lambda, \lambda, I_i, I_f)$ the ordinary *geometrical factor*

$$F_k(\lambda, \lambda', I_i, I_f) = (-1)^{I_i+I_f-1}\sqrt{(2k+1)(2I_2+1)(2\lambda+1)(2\lambda'+1)} \\ \times \begin{pmatrix} \lambda & \lambda' & k \\ 1 & -1 & 0 \end{pmatrix} \begin{Bmatrix} \lambda & \lambda & k \\ I_f & I_f & I_i \end{Bmatrix} \tag{1.64}$$

and the Racah coefficients $W(j_1 j_2 l_2 l_1 \mid j_3 l_3)$ are written with the Wigner notation:

$$\begin{Bmatrix} j_1 & j_2 & j_3 \\ l_1 & l_2 & l_3 \end{Bmatrix} = (-1)^{j_1+j_2+l_1+l_2} W(j_1 j_2 l_2 l_1 \mid j_3 l_3). \tag{1.65}$$

The angular distribution as a function of the statistical tensor is written

$$W(\theta_\gamma, \phi_\gamma) = \sum_{kq} \sqrt{2k+1}\rho_{kq}(\theta_p, \phi_p) A_k(\delta, L, L', I_f, I_i) Q_k D^{k*}_{q0}(\phi_\gamma, \theta_\gamma, 0) \tag{1.66}$$

where the coefficients $A_k(\delta, L, L', I_f, I_i)$ define a γ-ray transition from the state I_i to the state I_f with multipolarities L and L' and mixing ratio δ [30], and are related to the F_k factors by

$$A_k(\delta, L, L', I_f, I_i) = \frac{1}{1+\delta^2} F_k(LLI_fI_i) + 2\delta F_k(LL'I_fI_i) + \delta^2 F_k(L'L'I_fI_i) \tag{1.67}$$

and where the total scattering angle notation ϑ was substituted by θ_p indicating the direction in which the particle is emitted. The factors Q_k are the attenuation coefficients that take into account the finite solid-angle opening of the γ-ray detectors.

If the spin distribution of the initial state and the particle detector share the same symmetry, as the case in Coulomb excitation experiments with a cylindrical particle detector, the statistical tensor elements vanish for $k \neq q$, so that $\rho_{kq}(\theta_p, \phi_p) = \delta_{q0}\rho_{kq}(\theta_p)$. But $D^{k*}_{00}(\phi_\gamma, \theta_\gamma, 0) = P_k(\cos\theta_\gamma)$ so eq. 1.66 reduces to

$$W(\theta_\gamma, \phi_\gamma) = \sum_{q} \sqrt{2k+1}\rho_k(\theta_p, \phi_p) A_k(\delta, L, L', I_f, I_i) Q_k P_k(\cos\theta_\gamma) \tag{1.68}$$

where $P_k(\cos\theta_\gamma)$ are the *Legendre polynomials.*

With the statistical tensors defined by eq. 1.63 and eq. 1.62 this formula can be used to evaluate the angular distribution of the de-excitation radiation in the case of inverse kinematics and a particle detector with a symmetry around the beam axis.

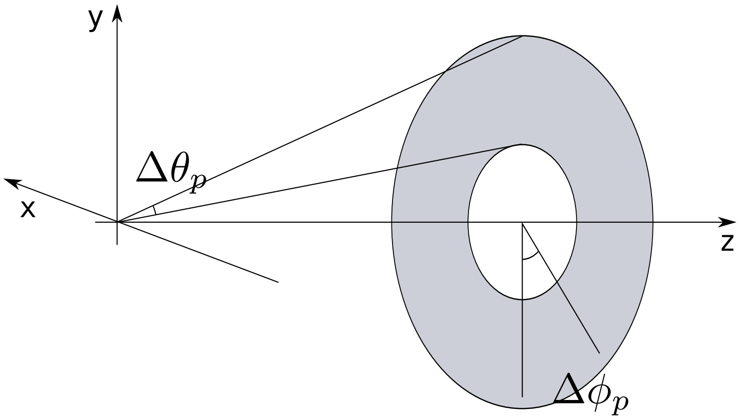

FIGURE 1.9: Break up of the azimuthal symmetry. The particle detector was composed of eight segments in order to discriminate the ϕ_p angle.

1.3.3 Segmented particle detector

Stuchbery [28] used the COULINT code to calculate the angular distribution coefficients in their most general form, eq.1.38, taking into account the target thickness and the energy loss. Integration over specific angles was performed afterward. This gave the possibility to calculate the angular distributions in the general case of a radially segmented particle detector.

Starting from the GKINT Stuchbery wrote a new code, called GKINT_phi, to calculate the angular correlation in case of radially segmented particle detector with arbitrary dimensions. The simulation considers a particle counter composed of n segments with $\Delta\phi_p$ aperture. The $\Delta\theta_p$ interval is treated like in the standard GKINT code. In fig.1.9 the geometry of the system is shown.

The code evaluates the angular distribution directly calculating the coefficients 1.38

$$\begin{aligned} b^{E\lambda}_{kq}(\theta_p,\phi_p,\xi) = &-\frac{1}{\sqrt{2k+1}}\begin{pmatrix}\lambda & \lambda & k\\ 1 & -1 & 0\end{pmatrix}^{-1}\sum_{\mu\mu'q'}(-1)^{\mu}\begin{pmatrix}\lambda & \lambda & k\\ \mu & \mu' & q'\end{pmatrix}\\ &\times Y_{\lambda\mu}\left(\frac{\pi}{2},0\right)Y_{\lambda\mu'}\left(\frac{\pi}{2},0\right)I(E\lambda,\mu)I(E\lambda,\mu')D^{k}_{q'q}\left(\frac{\pi}{2}+\frac{\theta_p}{2},\frac{\pi}{2},\phi_p-\frac{\pi}{2}\right). \end{aligned} \tag{1.69}$$

with the proper integration intervals.

The code outputs the statistical tensor $\rho_{kq}|^{\theta_{max}}_{\theta_{min}}$ calculated on the particle detector's opening angle $\theta_{min}-\theta_{max}$. The values are then put in the function 1.66

$$W(\theta_\gamma,\phi_\gamma)=\sum_{kq}\sqrt{2k+1}\rho_{kq}(\theta_p,\phi_p)|^{\theta_{max}}_{\theta_{min}}A_k(\delta,L,L',I_f,I_i)Q_kD^{k*}_{q0}(\phi_\gamma,\theta_\gamma,0). \tag{1.70}$$

The rotation matrix is converted to spherical harmonics with eq. 1.116 and eq. 1.117

$$W(\theta_\gamma, \phi_\gamma) = \sum_{kq} \sqrt{2k+1}\rho_{kq}(\theta_p, \phi_p)|_{\theta_{min}}^{\theta_{max}} A_k(\delta, L, L', I_f, I_i) Q_k \times (-1)^q \sqrt{\frac{4\pi}{2k+1}} Y^k_{-q}(\theta_\gamma, \phi_\gamma) \tag{1.71}$$

$$= \sum_{kq} \sqrt{4\pi}(-1)^q \rho_{kq}(\theta_p, \phi_p) A_k(\delta, L, L', I_f, I_i) Q_k Y^k_{-q}(\theta_\gamma, \phi_\gamma) \tag{1.72}$$

The sum contains only even k values because for k odd the statistical tensor are zero due to the symmetry of the electromagnetic interaction. Only values up to $k = 4$ are considered because an electromagnetic transition is fully described by the $k = 0, 2, 4$ three terms. The spherical harmonics are defined by

$$Y_l^m = (-1)^m \sqrt{\frac{2l+1}{4\pi}\frac{(l-m)!}{(l+m)!}} P_l^m(\cos\theta) e^{im\phi} \tag{1.73}$$

where $P_l^m(x)$ are the *associated Legendre polynomials*. The Condon-Shortley phase was used. The relation

$$P_l^{-m}(x) = (-1)^m \frac{(l-m)!}{(l+m)!} P_l^m(x) \tag{1.74}$$

is used for the $m < 0$ terms.

The angular distribution only depends on ϕ through the difference $\Delta\phi = \phi_\gamma - \phi_p$, because it is true that

$$\rho_{kq}(\theta_p, \phi_p) = \rho_{kq}(\theta_p) e^{-i\phi_p} \tag{1.75}$$

since the dependence of ρ_{kq} on ϕ is given by a rotation matrix, and we can bring the exponential in the definition of spherical harmonic

$$Y_l^m(\theta_\gamma, \phi_\gamma) e^{-i\phi_p} = (-1)^m \sqrt{\frac{2l+1}{4\pi}\frac{(l-m)!}{(l+m)!}} P_l^m(\cos\theta_\gamma) e^{im\phi_\gamma} e^{-i\phi_p} = Y_l^m(\theta_\gamma, \phi_\gamma - i\phi_p) \tag{1.76}$$

to obtain the final expression for the angular distribution

$$W(\theta_\gamma, \Delta\phi) = \sum_{kq} \sqrt{4\pi}(-1)^q \rho_{kq}(\theta_p) A_k(\delta, L, L', I_f, I_i) Q_k Y^k_{-q}(\theta_\gamma, \Delta\phi) \tag{1.77}$$

where $\Delta\phi = \phi_\gamma - \phi_p$ and $\rho_{kq}(\theta_p)|_{\theta_{min}}^{\theta_{max}}$ is determined by the particle detector's opening angle.

The used spherical harmonics are

$$
\begin{aligned}
Y_0^0\,(\theta,\phi) &= \frac{1}{2}\sqrt{\frac{1}{\pi}} && (1.78)\\
Y_2^{-2}\,(\theta,\phi) &= \frac{1}{4}\sqrt{\frac{15}{2\pi}}\sin^2\theta e^{-i2\phi} && (1.79)\\
Y_2^{-1}\,(\theta,\phi) &= \frac{1}{2}\sqrt{\frac{15}{2\pi}}\sin\theta\cos\theta e^{-i\phi} && (1.80)\\
Y_2^0\,(\theta,\phi) &= \frac{1}{4}\sqrt{\frac{5}{\pi}}(3\cos^2\theta-1) && (1.81)\\
Y_2^1\,(\theta,\phi) &= -\frac{1}{2}\sqrt{\frac{15}{2\pi}}\sin\theta\cos\theta e^{i\phi} && (1.82)\\
Y_2^2\,(\theta,\phi) &= \frac{1}{4}\sqrt{\frac{15}{2\pi}}\sin^2\theta e^{i2\phi} && (1.83)\\
Y_4^{-4}\,(\theta,\phi) &= \frac{3}{16}\sqrt{\frac{35}{2\pi}}\sin^4\theta e^{-i4\phi} && (1.84)\\
Y_4^{-3}\,(\theta,\phi) &= \frac{3}{8}\sqrt{\frac{35}{\pi}}\sin^3\theta\cos\theta e^{-i3\phi} && (1.85)\\
Y_4^{-2}\,(\theta,\phi) &= \frac{3}{8}\sqrt{\frac{5}{2\pi}}\sin^2\theta(7\cos^2\theta-1)e^{-i2\phi} && (1.86)\\
Y_4^{-1}\,(\theta,\phi) &= \frac{3}{8}\sqrt{\frac{5}{\pi}}\sin\theta(7\cos^3\theta-3\cos\theta)e^{-i\phi} && (1.87)\\
Y_4^0\,(\theta,\phi) &= \frac{3}{16}\sqrt{\frac{1}{\pi}}(35\cos^4\theta-30\cos^2\theta+3) && (1.88)\\
Y_4^1\,(\theta,\phi) &= -\frac{3}{8}\sqrt{\frac{5}{\pi}}\sin\theta(7\cos^3\theta-3\cos\theta)e^{i\phi} && (1.89)\\
Y_4^2\,(\theta,\phi) &= \frac{3}{8}\sqrt{\frac{5}{2\pi}}\sin^2\theta(7\cos^2\theta-1)e^{i2\phi} && (1.90)\\
Y_4^3\,(\theta,\phi) &= -\frac{3}{8}\sqrt{\frac{35}{\pi}}\sin^3\theta\cos\theta e^{i3\phi} && (1.91)\\
Y_4^4\,(\theta,\phi) &= \frac{3}{16}\sqrt{\frac{35}{2\pi}}\sin^4\theta e^{i4\phi} && (1.92)
\end{aligned}
$$

which are, in general, complex functions. Since the statistical tensor is complex as well, the following rules for the multiplication of complex numbers

$$(a+bi)(c+di) = (ac-bd)+(ad+bc)i \tag{1.93}$$

were used.

To separate the real and imaginary part of the spherical harmonics, using the Euler notation, the relations

$$
\begin{aligned}
\mathrm{Re}(e^{im\phi}) &= \cos(m\phi) && (1.94)\\
\mathrm{Im}(e^{im\phi}) &= \sin(m\phi) && (1.95)
\end{aligned}
$$

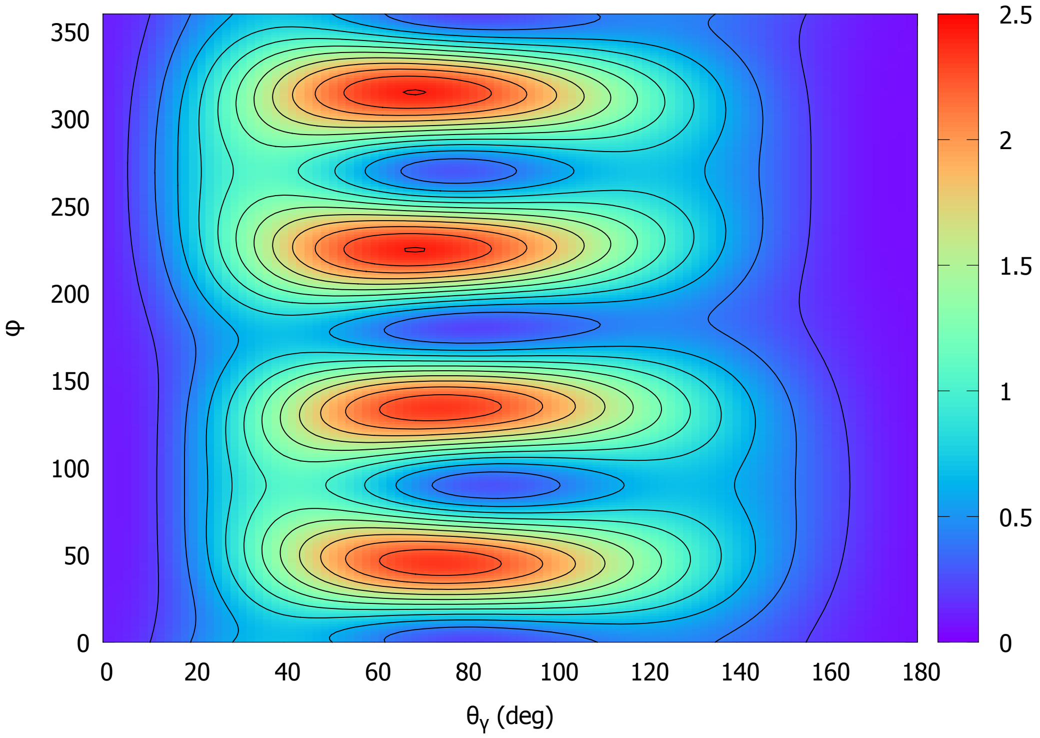

FIGURE 1.10: Calculated angular distribution for 40 MeV/nucleon ^{74}Ge projectile on a gadolinium target, particle detection angle interval $\theta_p = 4° - 6°$.

were used.

As an example, the bidimensional angular distribution for ^{74}Ge at 40 MeV/nucleon on a gadolinium target is plotted in figure 1.10, with the θ angle on the x-axis and ϕ on the y-axis. The anisotropy is clearly visible. In fig.1.11 is presented the angular distribution in the case of a particle detector radially divided into eight segments. With respect to the ring-like particle detector, the amplitude of the angular distribution is bigger in some cases. This would allow for a better precision in the measurement of magnetic moments via the integral perturbed angular correlation (IPAC, sect. 1.4), particularly sensitive to the derivative of the angular distribution. This is important for low intensity radioactive-ions beams (RIB), where a lower counting rate in the detectors can not be compensated by a higher rate of incident particles, although the RIV effect can have a destructive effect, as shown in section 1.3.7.

1.3.4 Lorentz correction

Since the de-excitation γ-rays are emitted by particles in motion with speed comparable to the speed of light, the relativistic boost effect take place: the direction in the rest-reference frame of the particle $(\theta_{nuc}, \phi_{nuc})$ is not the same as the one measured in the

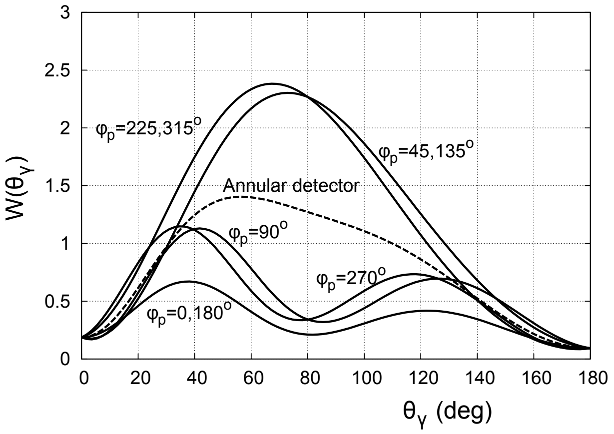

FIGURE 1.11: Calculated angular distribution for 40 MeV ^{74}Ge projectile on a gadolinium target, particle detection angle $\theta_p = 4° - 6°$. Dashed line is the case of a particle detector azimuthally symmetrical. Solid lines are for point-like particle detectors positioned at the corresponding ϕ_p angles, defining $\phi_p = 0°$ lying horizontally.

laboratory reference frame $(\theta_{lab}, \phi_{lab})$.

The two pair of angles are related by the expressions

$$\cos\theta_{lab} = \frac{\cos\theta_{nuc} + \beta}{1 + \beta\cos\theta_{nuc}} \tag{1.96}$$

$$\phi_{lab} = \phi_{nuc}. \tag{1.97}$$

where $\beta = v/c$ is the speed of the particle along $\theta = 0°$.

We have to insure that the flux of emitted γ-rays is constant

$$\int_{4\pi} W_{lab}(\theta_{lab})d\Omega_{lab} = \int_{4\pi} W_{nuc}(\theta_{nuc})d\Omega_{nuc} \tag{1.98}$$

for which we need the differential of the transformation

$$d\Omega_{lab} = \frac{1-\beta^2}{(1+\beta\cos\theta_{nuc})^2}d\Omega_{nuc}. \tag{1.99}$$

The angular correlation in the laboratory reference frame is then obtained applying the transformation 1.96 and multiplying by the ratio of the two solid angles

$$W_{lab}(\theta_{lab}) = W_{nuc}(\theta_{nuc})\frac{d\Omega_{nuc}}{d\Omega_{lab}} \tag{1.100}$$

where the ratio is retrieved from 1.99.

When calculating the precession angle, the effect of the Lorentz boost must be taken into account. The asymmetry ϵ (eq. 1.23) and the slope S (1.22) are calculated from the angular distribution measured in the laboratory reference frame. The asymmetry is not affected by the change of reference frame, as it will be shown. It can be written as

$$\epsilon = \frac{W(\theta_\gamma, \downarrow) - W(\theta_\gamma, \uparrow)}{W(\theta_\gamma, \downarrow) + W(\theta_\gamma, \uparrow)} \tag{1.101}$$

so when the condition 1.100 is imposed the differential in eq. 1.99 cancels out: $\epsilon_{nuc} = \epsilon_{lab}$. The slope must be computed at angles in the rest-reference frame of the nucleus:

$$S_{nuc} = \frac{1}{W(\theta_{nuc})} \frac{dW(\theta_{nuc})}{\theta_{nuc}} \bigg|_{\theta_\gamma\ nuc} \tag{1.102}$$

where θ_{nuc} are calculated inverting eq. 1.96

$$\cos\theta_{nuc} = \frac{\cos\theta_{lab} - \beta}{1 - \beta\cos\theta_{lab}}. \tag{1.103}$$

1.3.5 Precession calculation

The code GKINT calculates also the transient-field precession. It evaluates $\Phi(\tau)$, the precession angle per units of g-factor [31]:

$$\Phi(\tau) = \frac{\Delta\theta}{g} = -\frac{\mu_N}{\hbar} \int_{t_{in}}^{t_{out}} B_{TF}(v(t)) e^{-t/\tau} dt \tag{1.104}$$

where τ is the excited state lifetime, g its g-factor, t_{in} and t_{out} the interaction start and stop times and $B_{TF}(v(t))$ the transient field strength as function of the time. The interaction starts when the state of interest is Coulomb excited, after the projectile enters the ferromagnetic layer of the target, and it finishes when the projectile leaves it or decays.

The average interaction time is calculated with the formula

$$t_{eff} = \tau(e^{-t_{out}/\tau} - e^{-t_{in}/\tau}) \tag{1.105}$$

from which is possible to derive the average interaction velocity

$$\langle v \rangle = \frac{1}{t_{eff}} \int_{t_{in}}^{t_{out}} v e^{-t/\tau} dt. \tag{1.106}$$

If the lifetime of the state is much longer than the interaction interval the two relations reduce to

$$t_{eff} = t_{out} - t_{in} \tag{1.107}$$

$$\langle v \rangle = \frac{L}{t_{eff}} \tag{1.108}$$

where L is the target thickness.

The rotated statistical tensor is

$$\rho_{kq}(\theta_p,\phi_p,\Delta\theta)=\sum_{q'}\rho_{kq'}(\theta_p,\phi_p)D^k_{qq'}(\tfrac{\pi}{2},\pm\Delta\theta,-\tfrac{\pi}{2}) \tag{1.109}$$

where the sum is performed on $|q'|\leq k$. The rotation matrix can be explicitly written

$$\begin{aligned}\sum_{|q'|\leq k}D^k_{qq'}(\tfrac{\pi}{2},\pm\Delta\theta,-\tfrac{\pi}{2}) &= \sum_{|q'|\leq k}D^k_{q0}(\tfrac{\pi}{2},\pm\Delta\theta,0)e^{-iq'\frac{\pi}{2}} &(1.110)\\ &= D^k_{q0}(\tfrac{\pi}{2},\pm\Delta\theta,0)\sum_{|q'|\leq k}e^{-iq'\frac{\pi}{2}} &(1.111)\\ &= D^k_{q0}(\tfrac{\pi}{2},\pm\Delta\theta,0)\cdot 1. &(1.112)\end{aligned}$$

Then because of the cylindrical symmetry it is true that

$$\begin{aligned}\rho_{kq}(\theta_p,\phi_p,\Delta\theta) &= \rho_{k0}(\theta_p,\phi_p)D^k_{q0}(\tfrac{\pi}{2},\pm\Delta\theta,0) &(1.113)\\ &= \rho_{k0}(\theta_p,\phi_p)D^k_{q0}(\pm\tfrac{\pi}{2},\mid\Delta\theta\mid,0) &(1.114)\\ &= \rho_{k0}(\theta_p,\phi_p)\sqrt{\frac{4\pi}{2k+1}}Y^k_q(\mid\Delta\theta\mid,\pm\tfrac{\pi}{2}) &(1.115)\end{aligned}$$

where in the last passage the rotation matrix-spherical harmonic equivalence

$$D^k_{q0}(\alpha,\beta,0)=\sqrt{\frac{4\pi}{2k+1}}Y^k_q(\beta,\alpha) \tag{1.116}$$

was used.

To get the rotated angular distribution we substitute the rotated statistic tensor eq. 1.115 in eq. 1.66 and we use the relation

$$Y^{k*}_q(\beta,\alpha)=(-1)^qY^k_{-q}(\beta,\alpha) \tag{1.117}$$

obtaining

$$\begin{aligned}W(\theta_\gamma,\phi_\gamma,\Delta\theta)=\sum_{kq}(-1)^q\frac{4\pi}{\sqrt{2k+1}}\rho_{kq}(\theta_p,\phi_p,\Delta\theta)A_k(\delta,L,L',I_f,I_i)Q_k\\ \times Y^k_q(\mid\pm\Delta\theta\mid,\tfrac{\pi}{2})Y^k_{-q}(\theta_\gamma,\phi_\gamma).\end{aligned} \tag{1.118}$$

In this equation we have to include the terms for the evaluation of the recoil-in-vacuum de-orientation, discussed in the next section.

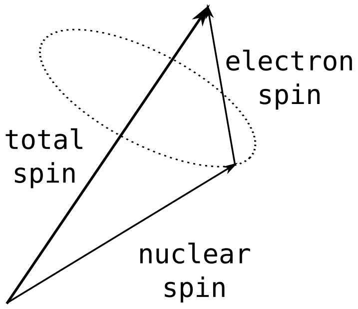

FIGURE 1.12: Spin coupling: nuclear spin is aligned from the reaction, electron spin is isotropic. The two spins precess about the total spin.

1.3.6 Recoil-in-vacuum attenuation

When emerging from the secondary excitation target, the hyperfine field generated by the electrons surrounding the excited nucleus makes the nuclear spin precess. The rotation is about the total spin generated by the coupling of the atomic spin with the nuclear one, following the usual spin coupling rules (fig. 1.12). The atomic spin is isotropic, i.e. there are no preferred directions, while the nuclear spin is oriented during the Coulomb excitation process. The result of this interaction is to lower the degree of alignment of the initial spin ensemble, resulting in a damping of the amplitude of the angular distribution. The recoil-in-vacuum deorientation magnitude is function of the charge state distribution of the ions exiting the target, so it depends on their velocity, and on the spins of the atomic levels occupied by the electrons. Other factors influencing the RIV are the g-factor of the nuclear state and the interaction time, connected with the state life-time.

A calculation from first principles is, like in the case of the transient field, not possible. The charge state distribution of the ions exiting the target can be evaluated from stripping foil studies, while the in flight precession mechanism is still under development. Stuchbery and Stone are working in this direction, ref. [15] contains a discussion on the recoil-in-vacuum (RIV) effect.

The effect is taken into account including a factor G_k to the angular distribution Eq. 1.118:

$$\begin{aligned} W(\theta_\gamma, \phi_\gamma, \Delta\theta) = \sum_{kq} (-1)^q \frac{4\pi}{\sqrt{2k+1}} \rho_{kq}(\theta_p, \phi_p, \Delta\theta) A_k(\delta, L, L', I_f, I_i) \\ \times G_k Q_k Y^k_q(\mid \Delta\theta \mid, \pm\tfrac{\pi}{2}) Y^k_{-q}(\theta_\gamma, \phi_\gamma). \end{aligned} \tag{1.119}$$

The code GKINT evaluates these factors from experimental data. The evaluation is based on the assumptions that the deorientation effect is dominated by the magnetic field from the electrons in the ground state and that H-like electron configuration ions are the most important contributors. This latter assumption is sustained by the fact that the magnetic field of the electron at the nucleus is

$$B_{ns} = 16.7Z^3/n^3 \quad [T]. \tag{1.120}$$

and that for exiting velocities around v_K the charge state distribution is dominated by H-like ions. The vacuum deorientation for a pure $1s$ configuration is [29]

$$G^k_{1s} = 1 - b_k \frac{(\omega_L \tau)^2}{1 + (\omega_L \tau)^2} \tag{1.121}$$

where ω_L is the Larmor frequency, τ is the state life-time and b_k is written

$$b_k = \frac{k(k+1)}{(2I+1)^2}. \tag{1.122}$$

If the product $\omega_L \tau$ is small the recoil-in-vacuum is small as well, because the precession does not act for a long time (small τ) or because the g-factor is small (small ω_L). As the quantity $\omega_L \tau$ is growing, G_k approaches an asymptotic value called *hardcore* value, which is the maximum deorientation the system can undergo.

For $I = 2$ the parameters are $b_2 = 0.24$ and $b_4 = 0.80$ so the hardcore values are ${}^{hc}G^{1s}_2 = 0.76$ and ${}^{hc}G^{1s}_4 = 0.20$. In practice for any life-time longer than a picosecond and even for small g-factor the hyperfine field is so strong that the approximation G^{1s}_k holds.

At lower velocities, the $3s$ contribution could be important. We can write the total deorientation coefficients in terms of the fraction of charge states for H-like and Li-like ions Q_H Q_{Li}

$$G_k = (1 - Q_H - Q_{Li}) + Q_H G^{1s}_k + Q_{Li} G^{3s}_k \tag{1.123}$$

which reduces to

$$G_k = 1 - Q_H b_k \frac{(\omega_L \tau)^2}{1 + (\omega_L \tau)^2} - Q_{Li} b_k \frac{(\omega_L \tau/8)^2}{1 + (\omega_L \tau/8)^2} \tag{1.124}$$

GKINT uses experimentally evaluated charge state [32] distributions to calculate G_k.

1.3.7 RIV attenuation: effect on ϕ

When breaking the azimuthal symmetry, the recoil in vacuum effect have a more profound impact on the angular distribution compared to the symmetric case, described in the previous sections. I analyze in more detail the phenomenon finding that the impact of the RIV effect is not the same on the θ and ϕ angles. This result give a physical motivation to assume the dependence on the ϕ angle completely lost and it is important to explain the results from the experiment described in Chap. 4.

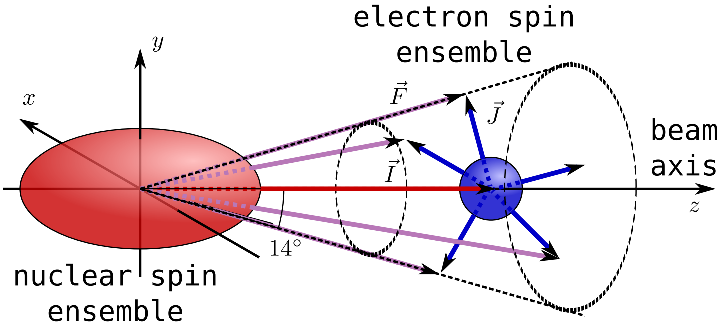

FIGURE 1.13: Recoil-in-vacuum and effect on ϕ dependence in Coulomb excitation. In red,; on the left, we have the prolate nuclear angular momentum $\vec{I}$ ensemble, and in blue, on the right, the isotropic electron spin $\vec{J}$ ensemble. If we consider only electrons in their ns states, their spin will be small ($J = 1/2$) than the nuclear angular momentum of the state (generally $I = 2$). The resultant spin $\vec{F}$ will have the same prolate orientation that characterizes the nuclear spin ensemble. To first approximation, we consider the precession axis parallel to the z-axis.

Coulomb excitation, when the impact parameters are sufficiently small (in the hard-spheres model, the sum of the two radii plus few fm) and for excitation energies up to few MeV, produces well-oriented prolate spin distributions [33]. Typically the excited state will have an angular momentum $I = 2$, while the electrons in their ground states will have $J = 1/2$. Assuming the nuclear spins all directed along the z-axis and the electons' spins isotropically distributed, the resulting total angular momentum F will be directed in a solid angle with an aperture of 14° with respect to the beam axis, as illustrated in figure 1.13. This angle is small enough to allow us to consider as first approximation the precession due to the RIV hyperfine fields along the z-axis.

According to this assumption, each ion exiting from the target will be rotated about the z-axis at a random angle φ. We now assume that an angle $\varphi = \pi$ rad is enough to wash out completely the sensitivity of the angular distribution to the angle ϕ. We can estimate the fields necessary to have such an angle from the formula 1.20

$$\varphi = -g\frac{\mu_N}{\hbar}B_{HF}\Delta t \tag{1.125}$$

from which, expressing the field strength in kT and the interaction time in ps, it follows

$$B_{HF} = 0.0209\frac{\varphi}{g\Delta t}. \tag{1.126}$$

Considering $\varphi = \pi$ rad and $\Delta t = 20$ ps we infer that fields of ≈ 10 kT are enough to wash out the information on the ϕ angle.

Are the electrons' hyperfine fields strong enough? The field at the nucleus of the ns electrons is (eq. 1.120)

$$B_{ns} = 16.7Z^3/n^3 \quad [T]. \tag{1.127}$$

n	1	2	3	4	5	6
B_{TF} [kT]	780	97	29	12	6	4

Table 1.1: Field at nucleus for ns electrons as function of the principal quantum number. $n = 1$ corresponds to ions with charge state 1, H-like, $n = 2$ to charge state 3, Li-like and so on.

which for a nucleus with $Z = 36$ gives the result shown in Tab. 1.1. We point out that up to $n = 5$ the hyperfine fields are strong enough to have a destructive effect on the ϕ dependence of the angular distribution. The charge-state distribution is playing an important role, depending on the experimental conditions. In Chap. 4 it will be shown that despite the extreme crudeness of the proposed explanation, the observed results for ^{78}Kr and ^{74}Ge confirm it.

1.3.8 Finite beam spot size

All the theoretical work in this section considered the spot of the beam impinging on the target to be point-like. We now examine the effect of having a beamspot of finite size. It was imagined that the anisotropy of the angular distribution could be damped, but it was unknown to what extent. A code was developed by Stuchbery [34] to simulate the case. The results are visible in figure 1.14. The enhancement of the angular distribution is only apparent, because the effect is due to the not-centered beam spot. What must be noticed is the damping of the anisotropy: while in the point-like case the difference between the two peaks and the trough is ≈ 0.35, in the finite size case it is ≈ 0.25. It must be noticed that the effect of the recoil-in-vacuum deorientation is substantially similar, so, since we don't have any information about the beam spot size, retrieving informations about the RIV effect becomes very difficult.

1.4 Transient Magnetic Field

A transient magnetic field (TF) arises from the hyperfine interaction between a moving ion and its electronic cloud. Only inner-shell electrons are contributing to the magnetic field. When a considerable part of the microscopic field is oriented in a particular direction, the total effect is like an external magnetic field that reaches a strength of tens of kT.

It was in 1966 when the MIT-Wisconsin group [35] noticed that the measurements of the magnetic moments were systematically different if the excited state was embedded in the ferromagnetic target where it would experience the static hyperfine field (e.g. melted together or thermodiffused) or if it was implanted following a violent nuclear reaction.

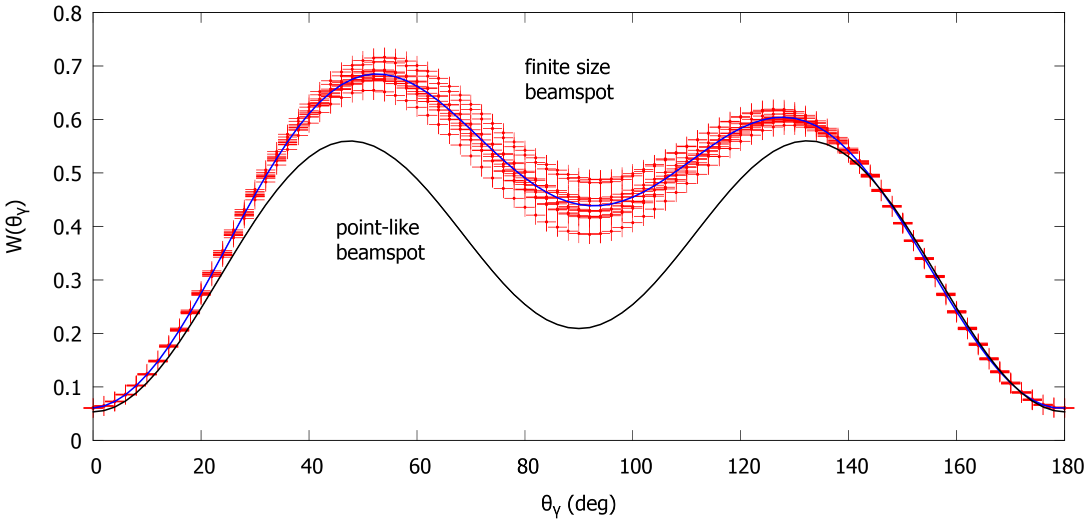

FIGURE 1.14: Finite size beamspot. The Monte Carlo simulation was performed with the code [34] for a ^{74}Ge projectile at 40 MeV/nucleon energy on a gadolinium case. The beam spot is 1×1 cm shifted 5 mm positive x-axis direction and 5 mm up. The particle detector has an angular opening of $\Delta\theta = 4° - 6°$ and $\Delta\phi = 30°$ and is positioned at 90° (segment number 5 of the eight-segment particle detector). Lorentz boost is not implemented and the asymmetry is due to the shift of the beam spot. The blue curve is the average of ten Monte Carlo runs. For comparison, the black curve is the centered point-like beamspot.

In the latter case, there was always a component of the magnetic field parallel to the external magnetic field that was generating the precession effect. Since the static hyperfine field is in some cases parallel to the external polarizing magnetic field and in others – antiparallel, this effect had to have a different origin, unknown at that time. It was then realized that a magnetic field acts on the excited states while they are moving in the ferromagnet, during the process of slowing down. Since the slowing down interval is typically of the order of few picoseconds, it was realized that the field must be very strong.

The consequences of this discovery were immediately perceived: a whole new range of nuclear states with half-lives of less than a ns became accessible for the measurement of magnetic moments. A theory was needed to allow for a proper exploration of the possibilities given by the TF. In 1971 Lindhard and Winther [36] proposed that the TF originated from the Coulomb scattering of electrons in the ferromagnet off the bare charge of the moving ion. This scattering causes the electron density at the nucleus to increase, and a net magnetic field to appear, since the electrons in the target are polarized by the external magnetic field. The Lindhard and Winther (LW) model had only one parameter that was fitted to the data then available, and predicted the TF to have a $1/v$ trend, i.e. the faster the ion the smaller the effect. Already three years later, in 1974 [37], the model needed an adjustment (indeed, it was then called Adjusted LW, ALW) because the newly available data at higher velocities showed an increased magnetic field.

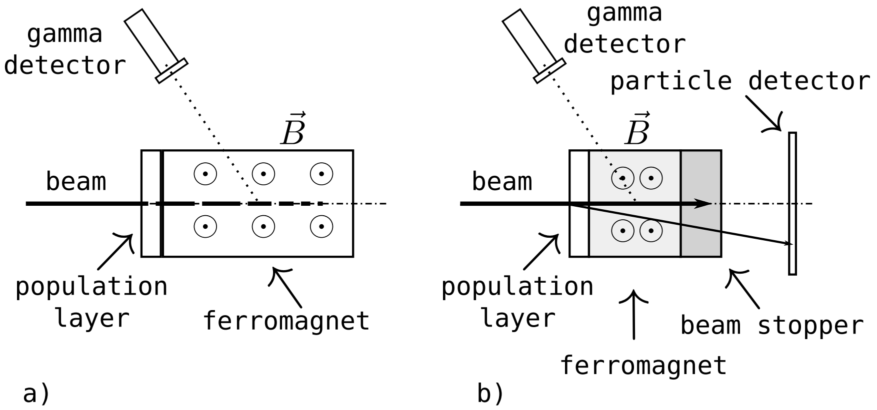

FIGURE 1.15: Transient field technique: experimental set-up. a) two-layer target: the probe is populated in the first layer and interacts with the TF field in the second ferromagnetic target, where it is stopped. Among other quantities, stopping powers of both material has to be well known in order to get a good estimation of the interaction time. b) three-layer target: the thickness of the ferromagnet is lowered to allow the beam and the products of the reaction to pass through, a third layer is added with a thickness calculated to stop the beam particles and let the products reach the particle detector.

The data used for this new parametrization were all taken at relatively low velocity, at about 1% of the speed of light. In 1975 the Bonn-Strasbourg group [38] using Oxygen probes at higher velocity ($v/c \approx 0.02$) showed that the field was considerably larger than predicted by the ALW. Other experiments followed [39–41] that confirmed the discovered trend: the TF magnitude was rising with the increased velocity. A direct proportionality with the velocity rather than an inverse one was found.

Let us give a few more details on how these first experiments were carried out. The target consisted usually of two layers: a thin production layer, where the state is populated, and a thick ferromagnetic layer, where the probe experiences the TF and then stops. The angular distribution showed both the effect of the TF and of the static hyperfine fields. The lifetime of the probe, the stopping power and the possible radiation damage effects, with their uncertainties, must all be well known to give reliable and precise results, and this was usually not the case. The experimental set-up is sketched in fig. 1.15. A great improvement was possible using a differently structured target, with three-layers. The first one was the usual population layer. The second ferromagnetic layer was made thinner to allow the particles to go through. The third and final layer was a beam stopper with a carefully calculated thickness to stop the direct beam and to let the products of the reaction of interest pass through to a particle detector. In this way the interaction time of the probe with the TF is easily and exactly calculated from the kinematics and the static effects are completely cut out. This represented a real breakthrough in the technique, allowing for the measurement of nuclear states populated in heavy-ion reactions, which are characterized by high recoil velocities. In 1980 Benczer-Koller [42] wrote a review of the state of the TF technique, where the challenges this field presented were thoroughly described.

Still, a new model was needed, probably very different from the Coulomb scattering suggested by the LW model, which proved to be very convincing, but wrong. Three new empirical parametrization were proposed, first the linear parametrization [43], then the Rutgers [44] and the Chalk-River [45]. They were more parameterizations than models, meaning that a suitable formula was used to fit the experimental data.

New experimental evidence showed that the TF arises from the capture of ns spin-polarized electrons by the probe. To show an effect the probe must capture, in its ns state, one of the ferromagnet's electrons polarized by the external magnetic field. The electron Fermi contact field is well known to scale with $(Z/n)^3$, with Z the atomic number of atom and n the principal quantum number of the electron. This field then ranges from the kT for light nuclei ($Z \approx 8$) to the MT of heavier nuclei ($Z \approx 90$). From the same microscopic model, we can predict that the TF strength should increase with the speed, since the ionization of the probe proceeds from the outer shells (high n) to the inner ones (low n) with the increase of the projectile speed, up to a maximum when the $1s$ shell is ionized, which happens for $v_{probe} \approx v_K$ where $v_K = Zv_0$ is the velocity of the electrons in the K-shell and $v_0 = e^2/(\hbar 4\pi\epsilon_0) = c/137$ is the Bohr velocity. The TF intensity is then expected to drop until it no longer has no effect, corresponding to an ion that is traveling so fast that is unable to pick up electrons. This behavior was experimentally verified [46] using as probing state the first 2^+ of ^{12}C with an iron target. The microscopic model was then proposed

$$B_{TF} = \sum_n p_{ns}(v_{probe}, Z, host) q_{ns}(v_{probe}, Z) B_{ns}(Z) \tag{1.128}$$

where the sum n is on the principal electronic quantum number, q_{ns} the fraction of ions with a single ns electron, p_{ns} the fraction that is polarized and B_{ns} the electron Fermi contact field at the nucleus. Stuchbery [47] recently proposed a parametrization based on this model. For velocities above the electron velocity of the L-shell $v_L = 1/2 v_K$ the TF should arise predominantly by the $1s$ electrons in the K-shell. Eq. 1.128 then becomes

$$B_{TF} = p_{1s}(v_{probe}, Z, host) q_{1s}(v_{probe}, Z) B_{1s}(Z). \tag{1.129}$$

The Fermi field is well known to be [48]

$$B_{1s} = 16.7 Z^3 R(Z) [tesla] \qquad \text{with} \qquad R(Z) \approx 1 + \left(\frac{Z}{84}\right)^{2.5} \tag{1.130}$$

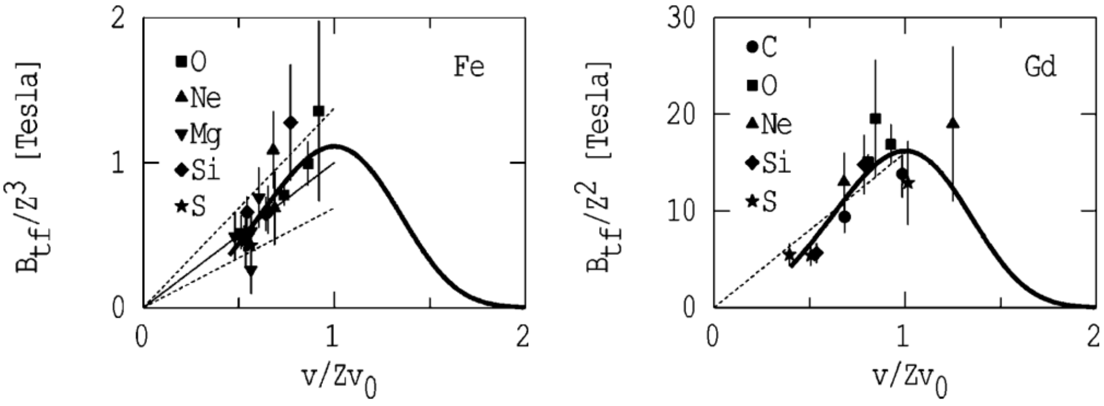

FIGURE 1.16: Transient field parametrization. Based on eq.1.129, Stuchbery [47] fitted all the high-velocity transient field strength experimental data available in the literature for Fe and Gd targets (left and right, respectively). The solid line is the proposed parametrization and the dashed one a linear parametrization. The quality of the fit is much worse in the latter case.

where $R(Z)$ is the relativistic correction factor. The fraction of polarized ion is supposed to be insensitive to the probe velocity (repeatedly observed experimentally for light ions [48–52]) and parametrized as

$$p_{1s}(v_{probe}, Z, host) = p_{1s}(Z) = A_p Z^{Z_p} \tag{1.131}$$

while the single K-vacancy fraction is expected to behave like the Hydrogen-like charge fraction of ions recoiling in vacuum,

$$q_{1s}(v_{probe}, Z) = \frac{1}{2}\sqrt{e}\left(\frac{v}{Zv_0}\right)^2 e^{-(v/Zv_0)^4/2} \tag{1.132}$$

as theoretically [48] and experimentally demonstrated [48, 53, 54]. Eq.1.129 then becomes

$$B_{TF} = A_p Z^{Z_p}\left(\frac{v}{Zv_0}\right)^2 e^{-(v/Zv_0)^4/2} \tag{1.133}$$

where A_p incorporates all the numerical factors. In fig.1.16 we have the results of this parametrization after fitting the measured transient field strengths. We can observe the bell-shaped behavior with the maximum of the field occurring for v/Zv_0.

The idea behind a magnetic moment measurement with the TF technique is the following: the precession effect $\Delta\theta$, proportional to the magnetic moment and to the field strength, is measured. B_{TF} is derived from the parametrization and consequently μ is calculated. Unfortunately a derivation of the TF strength from first principles is impossible due to a number of unknown quantities. This means that the calibration of the

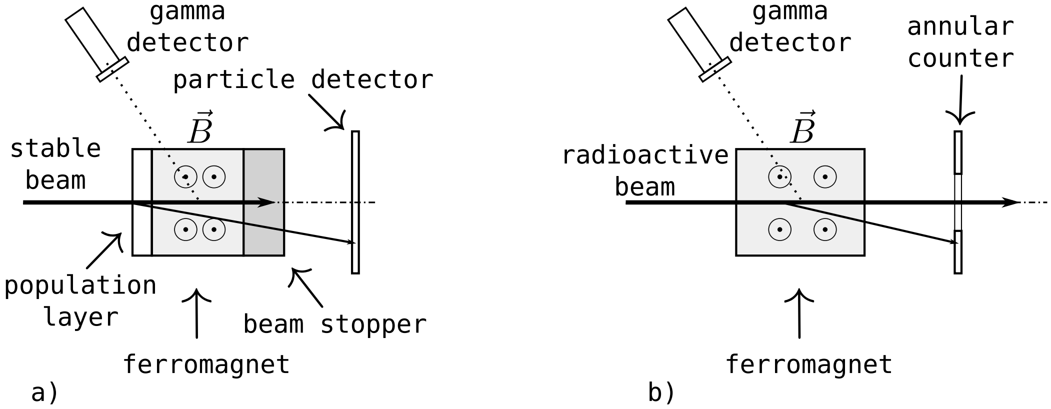

FIGURE 1.17: Transient field technique: different set-up geometries. *a)* the probe is populated in a nuclear reaction between the population target and the stable beam. The products are selected as illustrated in fig. 1.15. *b)* the radioactive beam is sent onto the ferromagnetic target, typically gadolinium, where it undergoes a Coulomb excitation. Proper angular selection of the scattered particles ensures a purely electromagnetic interaction.

field magnitude has to be extracted from neighboring nuclei with well known g-factors, in similar experimental conditions. It appears immediately obvious that the better and the more reliable the parametrization, the smaller the errors and the more robust the measurement.

Stuchbery makes it clear that the proposed parameters extracted from the experimental values [47], for which the two curves in fig.1.16 are plotted, are valid only in a determined Z range. In fact, the polarization-transfer mechanism could be different, and less efficient, when moving to higher Z probes, as already observed for Cr [55], Ge and Kr (in this work). For Cr (Z=24) a field 5 times less intense than predicted was observed, while for Ge and Kr (Z=32,36 respectively) the field drop is a factor of 10.

The TF at high velocities interests physicists for two reason: it is in principle possible to obtain higher fields than in the standard case and it is possible to use the TF technique with projectile-fragmentation products. Moreover, the higher energy allows for the use of thicker targets, compensating for the shorter time the ions would spend in a thin target. Usually after an in-flight fragment separators the ions are traveling very fast, at energies of about 30-300 MeV. The stronger magnetic field would allow larger precession effects, resulting in a more precise measurement with less statistics. This is very appealing considering that radioactive beams are orders of magnitude less intense than stable ones. In specific cases, depending on the Z of the ions of interest, it would be necessary to slow the projectiles to velocities around v_K, but this is preferable than slowing them to $\beta \approx 0.01$.

Using radioactive beams a different set-up is often preferable. The radioactive probe is

	Z	v cm/ns	E MeV/A	β
p	1	0.2	0.03	0.007
^{12}C	6	1.3	0.9	0.043
^{24}Mg	12	2.6	3.6	0.088
^{32}S	16	3.5	6.4	0.117
^{72}Zn	30	6.6	23	0.219
^{74}Ge	32	7.0	27	0.233
^{78}Kr	36	7.9	34	0.262

TABLE 1.2: Energies and velocities at $v = v_K$ for a selection of elements. The speed of light c is ≈30 cm/ns.

sent on a target to populate the state of interest through Coulomb excitation or particle transfer. With transfer reactions it is possible to go even further from the valley of stability, e.g. making a neutron pick-up using a neutron rich projectile. Then, using an annular particle detector, a selection on the particle scattering angle is performed, to exclude violent nuclear reactions. This arrangement is called *inverse kinematics*, opposed to the direct kinematics of the experiments described so far. Figure 1.17 illustrates the two different cases. In Tab. 1.2 the energies and velocities for $v = v_K$ are shown for some isotopes. The energy necessary to reach the maximum of B_{TF} increases steeply with Z.

An additional parameter is the element used as ferromagnetic target. The most often used are iron and gadolinium, but all ferromagnetic materials are in principle possible. The two materials have different characteristics. Due to the difference in Z (26 and 64 respectively) the stopping power of the first is higher than the second. If the probe has a very high velocity and a short life time, it has to be slowed down very quickly and a high stopping power is an advantage. On the other hand, the gadolinium allows for the use of thicker targets, corresponding to longer interaction time and bigger precession effect. Gadolinium with its higher Coulomb barrier, has a lower cross-section for nuclear reactions, which results in lower background. From the technical point of view, gadolinium has a Curie temperature of 282 K [56] so it is not ferromagnetic at room temperature. The need for on-line cooling make its use more complex.

Chapter 2

The N=40 region

Depuis l'origine de la physique nucléaire il est remarqué que certains noyaux exhibent une configuration particulièrement stable, avec des énergies de liaison élevées entre les nucléons. Une analyse plus approfondie révéla que cette stabilité mettait en évidence certains nombres de protons et neutrons, appelés nombres magiques. En 1934, Elsasser proposa une explication basée sur des fermetures de couches nucléaires en parallèle avec le modèle en couche atomique. Cette approche fut ensuite développée indépendamment par Goeppert-Mayer et Haxel, Suess et Jensen. La validité de ces nombres magiques ne fut discutée qu'après les années 70, quand il a été démontré que $N = 20$ *perdait sa magicité pour les noyaux les plus exotiques. Aujourd'hui il est montré que, lorsqu'on s'éloigne de la vallée de la stabilité, des nombres magiques disparaissent et d'autres apparaissent. Cet effet est la manifestation de mécanismes nucléaires qui selon les niveaux occupés par les protons et neutrons amènent à différents écarts d'énergie entre les niveaux et donc différentes fermetures de couche. Dans cette thèse une attention particulière est prêtée à la région autour du* ^{68}*Ni. La chaine isotopique du nickel est intéressante parce qu'elle contient trois isotopes magiques. Du coté des noyaux riches en protons il y a le* ^{48}*Ni, important pour la radioactivité à deux protons et pour être le seul noyau doublement magique avec un noyau miroir, le* ^{48}*Ca. Il y a ensuite le* ^{56}*Ni qui est un noyau auto conjugué. Du coté des noyaux riches en neutrons il y a le* ^{78}*Ni, important dans le processus d'intérêt astrophysique de capture rapide de neutrons. Au milieu il y a le noyau semi-magique,* ^{68}*Ni, qui exhibe des caractéristiques de noyau doublement magique par rapport aux autres isotopes du nickel, comme par exemple une énergie du premier niveau excité très élevée et une faible probabilité de transition. Par contre, l'énergie de liaison des nucléons ne dévie pas de la valeur prévue pour un noyau non-magique. On s'est donc interrogé sur la magicité du nombre* $N = 40$*. Pour ça on a étudié les noyaux autour du 68Ni, notamment les chaines isotopiques du cuivre et du cobalt, à un proton de distance,* *et du zinc. La structure du ^{72}Zn peut donner beaucoup d'information sur la dynamique nucléaire dans cette région, le moment magnétique est mesuré dans ce but.*

2.1 The shell model

Since the early age of nuclear physics, it has been noted that certain nuclei with a special number of protons or neutrons exhibit a particularly stable configuration. One quantity that measures this stability is the nucleon binding energy, the energy necessary to remove a proton or a neutron from the nucleus. This quantity is related to how strongly the nucleons are bound together.

In 1934 W. Elsasser [57] explained those numbers following the example of the atomic Bohr model as shell closures in a model of non-interacting nucleons occupying energy levels generated by a central potential. It was then assumed that the interaction energy between the nucleons is negligible compared to the energy of the average potential the nucleons are moving in. The first assumption for such potential was that it should be function of the coordinates of the particles only and an infinite well was chosen first, leading to a series of degenerate levels to be filled with nucleons according to Pauli's principle. As in the atomic case, the stability was the effect of a particularly wide gap between two levels: when the lower one was filled, the result was interpreted as a shell closure. This model did not convince the physicists of the time, to the point that Eugene Wigner called the numbers generated by the shell closure *magic numbers* [58]. In particular, it was not believed that the strong nuclear interaction would average out in such simple way. Moreover, the scarceness of the experimental data did not give credibility to the theory.

A prominent personality in nuclear physics, Niels Bohr, did not believe in the validity of the shell model, in the beginning. His argument was that much experimental evidence showed that the nuclear force was saturating, i.e. that the interaction between the nucleons was of the same order of magnitude as the interaction between the nucleon and the nucleus. For Bohr, this meant that it was not possible to consider the nucleons as separate entities with characteristic angular momentum and energy but that a collective approach was needed. His adaptation of the Gamow's liquid-drop model to his compound nucleus approach, for which nuclear excitations were attributed to "some quantized collective type of motion of all the particles" [59], explained the nuclear fission and terminated further development of the shell model.

With time, more experimental data became available. In 1948 M. Goeppert-Mayer [60] extensively reviewed nuclear properties for heavy elements and discovered a series of special numbers, the same for proton and neutrons, for which nuclei were particularly stable. The result was achieved through the analysis of the isotopic abundances. This first set of numbers was 20, 50, 82 and, for neutrons only, 126. To these numbers it must be added 2 and 8, which were not taken into account in Mayer's paper but which were well known for their stability, for example in $^{4}_{2}He_{2}$ and $^{16}_{8}O_{8}$. At that moment only the lower three could be explained as solutions of a simple potential well, while the others needed an *ad hoc* tuning of the level ordering. One year later Mayer [61] in America, following Enrico Fermi's suggestion [58], and at the same time the group formed by Haxel, Suess and Jensen [62] in Germany independently found the solution to the problem: they discovered that the inclusion in the potential of a velocity dependence term could lead to an explanation for all the discovered magic numbers. This term was called *spin-orbit coupling* and is the scalar product of two momenta: the intrinsic nuclear spin of the nucleon and the angular momentum of the level. From the spin-orbit coupling arose a new magic number, 28, which was not clearly identified before. This discovery was a real breakthrough in the understanding of nuclear structure.

A great deal of work was done in the following years. Brueckner [63] laid the theoretical basis showing that the short-ranged nuclear interaction and the Pauli principle combine together to give an almost independent particle motion. Nowadays this early model is called *independent particle model* (IPM) or *naïve shell model*. The model was tuned with the experimental results from the nuclei in the vicinity of three important doubly magic nuclei, ^{16}O, ^{40}Ca and ^{208}Pb. The farther the nuclei from those doubly magic configurations, the more important it is to take into account a correction due to the residual two-body interaction between the particles outside the inert core. This task, conceptually simple, in practice loses it simplicity very fast with the number of valence particles. As reported by Weidenmüller [64], Jensen himself, one of the creators of the shell-model, "…never lost his skeptical attitude towards the extension of the single -particle model to include the dynamics of several nucleons outside closed shells in terms of a residual interaction". In any case, all the developments were pursued taking into account a persistence of those numbers through all the nuclear chart.

The validity of the magic numbers in all the regions of the nuclear chart was not questioned for several decades. However, with the technical development of particle accelerators, it became possible to get a deeper insight of nuclei far from the valley of stability. The first magic number put to this test was N=20 [65]. It was shown that the shell closure was not preserved going further away from stability. Several mechanisms were taking part to modify the energy gaps between the nuclear levels, the same gaps that created the magic numbers. This discovery triggered a theoretical and experimental pursuit of the evolution of magic numbers far from the valley of stability. New magic numbers were found, e.g. $N = 16$ for $Z < 14$ [66] which results from the same mechanisms that lead to the reduction of the $N = 20$ shell closure for neutron-rich nuclei. The $N = 8$ shell closure disappears as soon as two protons are removed from the ^{14}C, with respect to ^{12}B. All this cases can be explained by the proton-neutron spin-isospin interaction which induce a reordering of the levels and the reduction of the shell gaps. Detailed references in [67–69] for the $N = 8$ case.

At present, we can count on many radioactive beam facilities, and the efforts are directed in both regions of instability of the nuclear chart, the proton-rich side and the neutron-rich one.

2.1.1 Tensor part of the nuclear force

Despite the fact that the shell model shows that somehow the strong nuclear interactions between the particles average out to a central potential, inside the nucleus nucleon-nucleon (NN) interaction cannot always be neglected. In the early age of nuclear physics, in 1935, Yukawa [70] proposed that the interaction is originated by a meson exchange process. The tensor-force part is one of the most distinct manifestations of meson exchange currents and it affects many aspects of nuclear structure. Its effect on the spin-orbit splitting was investigated by Arima and Terasawa [71] and on the nuclear binding energies by Pudliner *et al.* [72], for A <7. The way the tensor force influences the ordering of the orbitals was discussed by Otsuka *et al.* [73] in recent years. In this section we will dig more into this latter work because of its importance to understand the physics of the nuclear chart's region in which we are interested.

One-pion exchange is at the origin of the tensor force. This process is formalized as

$$V_T = (\vec{\tau}_1 \cdot \vec{\tau}_2)([\vec{s}_1 \cdot \vec{s}_2]^{(2)} \cdot Y^{(2)})f(r) \tag{2.1}$$

where $\vec{\tau}_{1,2}$ and $\vec{s}_{1,2}$ are respectively the isospin and the spin of the nucleon 1 and 2, $[\quad]^{(K)}$ represent the coupling of two operators to an angular momentum (K), Y are the familiar spherical harmonics, $\cdot$ is the scalar product and $f(r)$ a function of the relative distance between the two nucleons.

Following Otsuka's notation, we define j as the total angular momentum of the first particle and j' of the second. If we first consider the case of a single particle coupled to a core, its energy is determined by its kinetic energy and the effects of the inert core on the orbit j. When the second particle is added the energy of the first particle is changed. Limiting our interest to the monopole component of the interaction, using [74] we can write

$$V^T_{j \cdot j'} = \frac{\sum_J (2J+1)\langle jj'|V|jj'\rangle_{JT}}{\sum_J (2J+1)} \tag{2.2}$$

where $\langle jj'|V|jj'\rangle_{JT}$ is the diagonal matrix element of the state where the two nucleons are coupled to an angular momentum J and to an isospin T. In the summation J must take values that satisfy the antisymmetrization of the wave function.

With the two-body matrix elements 2.2 a monopole interaction V_M is constructed. This

interaction does not depend on the total angular momentum J, averaged out in the summation, but it does depend on the isospin T, so on the nature of the nucleons.
Let's consider now a number $n_n(j')$ of neutron in the j' orbit and a proton in the $j \neq j'$ orbit. The single particle energy of the proton is given by

$$\Delta\epsilon_p(j) = \tfrac{1}{2}(V^{T=0}_{j\cdot j'} + V^{T=1}_{j\cdot j'})n_n(j'). \tag{2.3}$$

Of course the same effect is affecting the neutrons when the proton orbitals are filled with $n_p(j)$ particles, with a corresponding energy shift $\Delta\epsilon_n(j')$. When we have more than two particles, the effect of all the nucleons in the orbits $j', j'', j''' \dots$ are summed up together. The single-particle energy taking into account this shift is called *effective single particle energy* (ESPE). We point out that if the neutrons and protons are occupying the same orbital, i.e. $j = j'$, Eq. 2.3 becomes more complicated because isospin symmetries must be taken into account. Another property of the tensor force is that it is zero for the spherical orbitals, i.e. when j or j' are $s_{1/2}$. It can also be shown [73] that if both orbitals j and j' are fully occupied the total tensor-force effect vanishes.
Otsuka then points out that the monopole tensor interaction, because of it isospin dependence, does not apply only to the proton-neutron orbitals but it is of neutron-neutron and proton-proton nature as well. From Eq. 2.1 it can be shown that the proton-neutron interaction is twice as strong as the other cases.
We now can proceed to analyze how the tensor force is affecting ESPE. Let's consider the case of protons in j orbital and neutrons in j'. For both of them we define $j_> = l + 1/2$ and $j_< = l - 1/2$. We consider the particles to be lying near the Fermi surface. Otsuka gives an intuitive interpretation: "a nucleon in $j_<$ is colliding with another in $j'_>$. Because of the high relative momentum between them, the spatial wave function of their relative motion is narrowly distributed in the direction of their collision which is basically the direction of the orbital motion. [...] the tensor force works attractively. [...] On the other hand the tensor force produces a repulsive effect for two nucleons in $j_>$ and $j'_>$ (or vice versa), because the wave function of the relative motion is stretched in the direction of the collision. Thus, we can obtain a robust picture that $j_<$ and $j'_>$ (or vice versa) orbits attract each other, whereas $j_>$ and $j'_>$ (or $j_<$ and $j'_<$) repel each other". In Fig. 2.1 an example is shown. The effect is stronger when the radial wave function of the two orbitals is similar. This happens when both orbitals are near the Fermi level, because the radial wave function has a sharp peak near the surface. From the same explanation we can argue that the effect grows more important with larger l and l', because the total angular momentum in the collision is larger.

In the cited paper [73] the analysis is taken to the phenomenological level analyzing the effect of the shell filling for different cases. The one in which we are particularly interested is the effect on the proton pf-shell from ^{68}Ni to^{78}Ni as the neutron $\nu g_{9/2}$ is

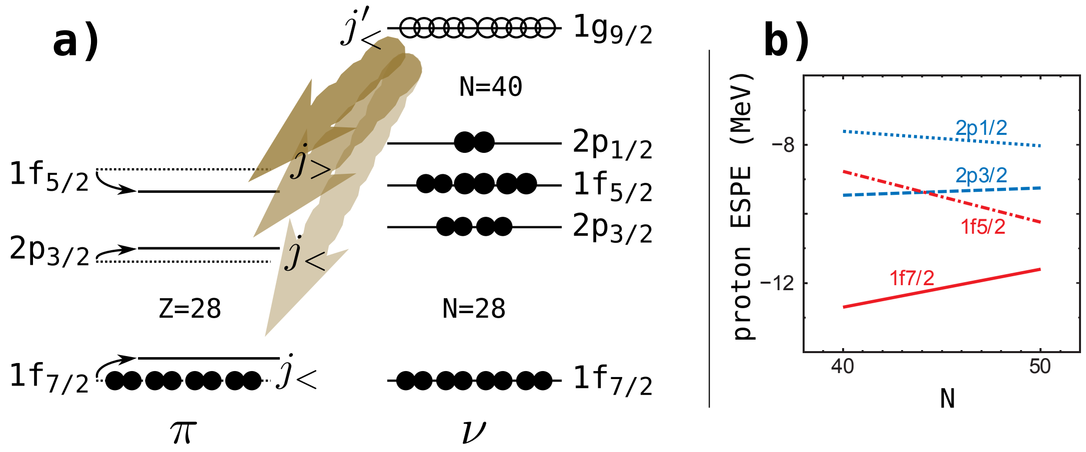

Figure 2.1: Effect of tensor force. *a*) the enregy of the orbital changes according to their spin: if the spins are antiparallel ($j_>$ and $j'_<$) the tensor force is attractive, leading to a lower ESPE, if the two spins are parallel ($j_<$ and $j'_<$) the force is repulsive and the ESPE is higher. *b*) evolution of the proton single particle orbitals when filling the $\nu g_{9/2}$, as calculated by Otsuka *et al.* [73]. Right picture from [73].

filled. In Fig. 2.1*b* the results for ESPE shell-model calculations are shown. With the increase of the neutron number the $\pi f_{5/2}$ is pulled down while $\pi p_{3/2}$ is lifted up, reaching a point where the two orbitals are crossing. We can notice that the effect on the ESPE (the slope of the curve in figure) is smaller for the p orbitals than for the f ones, which have a larger angular momentum. From the same figure we can observe how the tensor force affects the magnitude of the shell gaps: for ^{78}Ni it becomes much smaller. In the next section we will see the effects of the monopole tensor force on the nuclear properties.

2.1.2 Characterization of a shell closure

Grawe and Lewitowicz [75] claim the second difference in binding energy as the most sensitive and direct way to detect a shell closure. The quantity is defined for neutrons (protons) as

$$\delta_{2n(p)}(Z,N) = S_{2n(p)}(Z,N+2) - S_{2n(p)}(Z,N) \tag{2.4}$$

where the first mass derivative $S_{2n(p)}(Z,N)$, called also two neutron (proton) separation energy, are calculated from the binding energies

$$S_{2n(p)}(Z,N) = BE(Z,N) - BE(Z,N-2). \tag{2.5}$$

When filling a shell, the two nucleon separation energy is generally decreasing linearly with the number of particles, hence the second difference is constant. When a shell closure is reached, the enhanced stability of the nucleus makes subsequent particle removal less difficult and a singularity appears in the two-nucleon separation energy. This is

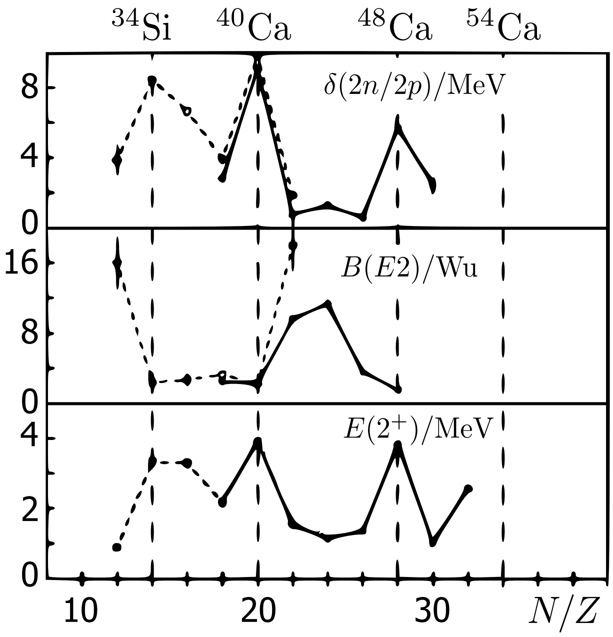

FIGURE 2.2: Second differences of the ground state binding energies δ_{2n} and δ_{2p}, excitation probabilities $B(E2; 2^+ \rightarrow 0^+)$ and their excitation energies of the first 2^+ state of the N=20 isotones and Z=20 isotopic chains. The graphic is taken from [75].

reflected by a sudden decrease of its value.

Other signs of an enhanced stability are higher excitation energy of the first 2^+ excited state $E(2^+)$ and low transition probability $B(E2; 2^+ \rightarrow 0^+)$ compared to the neighbor nuclei. In Fig. 2.2 the $N = 20$ and $Z = 20$ isotopic and isotonic chains are presented. The discontinuities in presence of ^{40}Ca and ^{48}Ca are well visible.

Although it must be pointed out that all those quantities, in particular the latter two, are also sensitive to other changes in the underlying nuclear structure. For example, quadrupole or octupole correlations can severely distort the two nucleon separation energy.

2.2 The neighbors of ^{68}Ni in the N=40 region

The region around the neutron-rich ^{68}Ni aroused interest because of the supposed doubly-magicity of this nucleus. Nickel presents a proton closed shell at $Z = 28$. It is the only element with three doubly magic nuclei in its isotopic chain. On the proton-rich side we have the ^{48}Ni which is interesting because of its double-proton radioactivity [76] and because it is the only double-magic nucleus with a known mirror partner ^{48}Ca, giving unique chance to study isovector effects. Then ^{56}Ni, a self-conjugated $N = Z$ nucleus with high δ_{2n} and excitation energy but high $B(E2; 2^+ \rightarrow 0^+)$ as well. Lastly there is

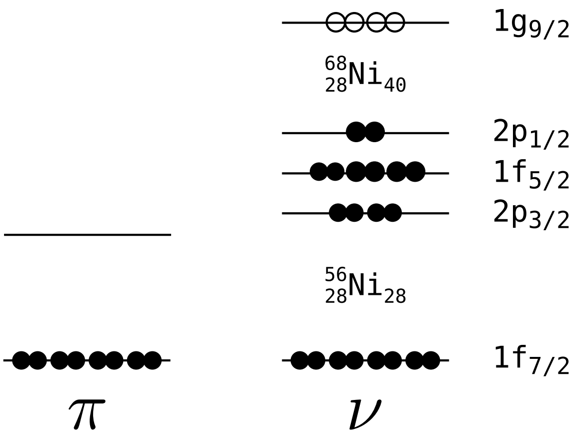

FIGURE 2.3: $_{28}$Ni Shell Model configuration. The N=28 shell closure is generated by the spin orbit interaction which has the effect of repel the $f_{7/2}$ from the $p_{3/2}$. The origin of the N=40 sub-shell closure is still debated but it may be related to the tensor component of the nuclear force [73].

^{78}Ni, an extremely neutron-rich nucleus of particular interest to the astrophysical rapid neutron-capture process [77].

The ordering of the shell orbitals is shown in Fig. 2.3. Nickel presents a full proton $\pi f_{7/2}$ shell followed by the two nearly-degenerate $\pi p_{3/2}$ and $\pi f_{5/2}$. The lowest neutron shell $\nu f_{7/2}$ is occupied between ^{48}Ni and ^{56}Ni, then the remaining fp shell up to^{68}Ni and the $\nu g_{9/2}$ up to ^{78}Ni.

N=40 was not included in the initial series of magic numbers, but when spectroscopic data for ^{68}Ni became available it raised the question whether if this nucleus can be considered doubly-magic or not. Bernas *et al.* [78] found in the beginning of the eighties that the first excited state of this nucleus was a 0^+ and not a 2^+ as expected. This was a first sign of possible magicity that was strengthened by the measurement of a particularly high energy (2.033 MeV) for the 2^+ state [79]. A few years later it was the turn of the transition probability $B(E2)$. The measured value [80, 81] is the smallest of the isotopic chain and it is comparable to the cases of ^{16}O,^{40}Ca and ^{48}Ca, well known for their double magicity.

However, other observations contradicted the presumed double-magic nature of this nucleus. In the isotopic chain the second difference δ_{2n} of ^{56}Ni stands out clearly while there is no sign of deviation for ^{68}Ni. The low transition probability was interpreted as a sign of the predominant neutron-excitation character of the state and not of a particularly wide energy gap [82]. Studying the parity of the neutron orbitals we notice that when filling the odd-parity fp shell, in order to maintain the parity of the 2^+ state at least two neutrons have to be excited to the intruder $g_{9/2}$ state. The absence of a peak in the δ_{2n} of the chain can be instead explained with quadrupole correlations. While

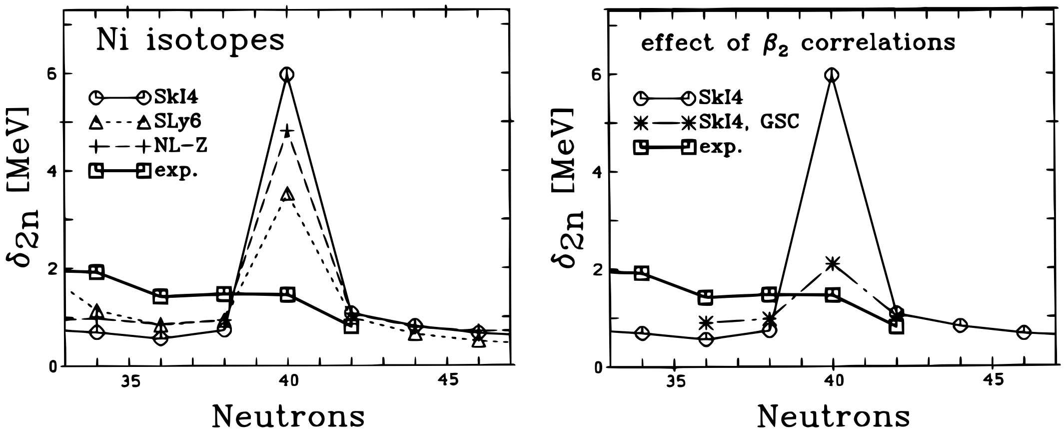

FIGURE 2.4: Mean field calculations for the second difference δ_{2n} for the isotopes around ^{68}Ni. In the left picture several approaches are tried, all leading to an observed peak. In the right picture quadrupole correlations are introduced. The agreement with the experimental data is better. Picture from [83].

most mean-field calculations predict the presence of a peak, the inclusion of quadrupole correlations [83] makes this peak disappear, Fig. 2.4.

An analysis of ^{68}Ni neighbors shows that the sub-shell closure is very localized and moving one or two protons away we observe that the low energy states are exhibiting collective or deformed behavior, as it will be illustrated in the next sections. The first excited state of ^{67}Co, a proton away from ^{68}Ni, is a proton intruder state of well deformed character [84]. Two protons below we have ^{66}Fe, which was interpreted as being well deformed [85]. Adding a proton we have ^{69}Cu, where the first excited state is assumed to be a $\pi f_{5/2}$ single-particle level [86]. Two protons above ^{70}Zn exhibits collective properties, such as a magnetic moment compatible with the hydrodynamical limit.

2.2.1 The Ni isotopic chain: evolution of the $Z = 28$ shell gap

The evolution of the Ni isotopic chain is related to the one of $Z = 28$ shell gap. As the number of neutrons varies, the proton-neutron interaction changes as well. Comparing the two even-N isotopes around ^{68}Ni, we can observe that the situation is not the same for the two isotopes. The difference in binding energy is lower in the less neutron-rich ^{66}Ni compared to ^{70}Ni. This leads to a higher excitation energy for the first 2^+ excited state and a lower transition probability. This behavior can be interpreted as an increase of collectivity for the more neutron-rich isotope, induced by the protons of the fp shell and the neutrons in the $\nu g_{9/2}$ orbital. In fact, the filling of the $\nu g_{9/2}$ orbital induces a reduction of the $\pi f_{5/2} - \pi f_{7/2}$ spin-orbit splitting, due to the nature of the tensor part of the nuclear force, attractive for the parallel $\pi f_{7/2} - \nu g_{9/2}$ and repulsive for the antiparallel $\pi f_{5/2} - \nu g_{9/2}$. This interpretation is supported by the observation of a constant lowering of $E(2^+)$ for $^{72-76}$Ni that can not be explained solely by neutron excitations in the $\nu g_{9/2}$ shell [87].

The large transition probability $B(E2; 2^+ \rightarrow 0^+)$ for ^{70}Ni can be interpreted in light of the other transition probabilities of the 8^+, 6^+, 4^+, 2^+ and 0^+ $\nu g^2_{9/2}$ multiplet when $J_{final} = J_{initial} - 2$. Because a spin 8^+ state cannot be built only with the protons in the fp shell, the wave function of this state is expected to be of mainly neutron nature. The $B(E2; 8^+ \rightarrow 6^+)$ is then taken as the reference point of the weakest core polarization. The measured transition probabilities [88–91] are compared to shell model calculations [92] in which the valence space is restricted to a pure neutron p, $f_{5/2}$, $g_{9/2}$ model space. The calculation for the $B(E2; 8^+ \rightarrow 6^+)$, $B(E2; 6^+ \rightarrow 4^+)$ and $B(E2; 4^+ \rightarrow 2^+)$ are in good agreement with the measured values while the $B(E2; 2^+ \rightarrow 0^+)$ is considerably underestimated. In order to increase this latter transition probability, proton-core interaction must be taken into account.

Sorlin and Porquet [93] explain the increased collectivity with the decrease of the $Z = 28$ shell gap by the attractive $\pi f_{5/2} - \nu g_{9/2}$ and the repulsive $\pi f_{7/2} - \nu g_{9/2}$ tensor-force interaction: "on the whole, the tensor term $\pi f - g_{9/2}$ would reduce both the $Z = 28$ gap and the $\pi f_{5/2} - \pi f_{7/2}$ splitting".

The analysis of the copper $Z = 29$ and cobalt $Z = 27$ isotopic chains gives important information about this proton-neutron interaction.

2.2.2 The Cu isotopic chain: monopole migration

Franchoo *et al.* [87] studied the neutron rich part of the $^{69-73}$Cu isotopic chain in a β-decay experiment from $^{68-74}$Ni produced in proton induced fission. The spectroscopic results were explained with the shell model. It was found that for all three odd isotopes the ground state had $3/2^-$ spin, explained with a dominating $\pi p_{3/2} \nu p^2_{1/2}$ wave function in ^{69}Cu, $\pi p_{3/2} \nu g^2_{9/2}$ in ^{71}Cu and $\pi p_{3/2} \nu g^4_{9/2}$ in ^{73}Cu. The first excited state is in all cases of $5/2^-$ spin-parity, but its energy drops sharply from 1214 keV in ^{69}Cu to 534 keV in ^{71}Cu and to 166 keV in ^{73}Cu. This behavior is particularly interesting if we consider that the energy of the $5/2^-$ level remains rather constant around 1 MeV for all the other stable and proton-rich Cu isotopes. The explanation for this behavior lies in the nature of this state. Shell model calculations showed that this level's wave function is of predominant single-particle nature, largely dominated by the $\pi f_{5/2}$ component. This phenomenon of systematic energy shift for single-particle levels was reported by several authors in different regions and for different shell closures [94–96] and it is called *monopole migration*. It finds its origins in the multipole expansion of the residual proton-neutron

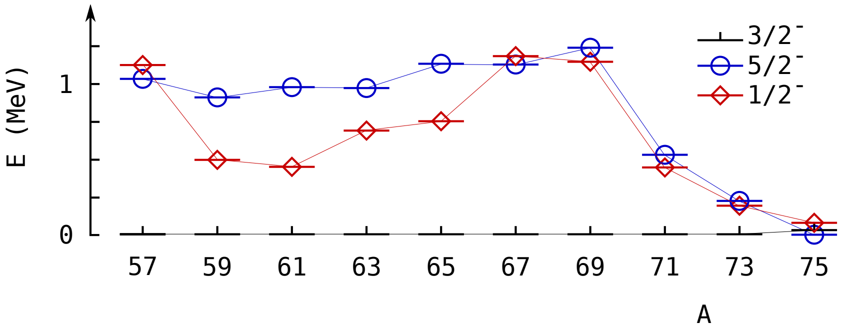

FIGURE 2.5: Monopole shift of the first $5/2^-$ excited state in the Cu isotopic chain. The single particle state energy is staying rather constant around 1 MeV up to ^{69}Cu. When the $\nu g_{9/2}$ starts being filled the level experiences a sudden drop in energy. Figure adapted from [87], ^{75}Cu data from [98].

interaction. Here the attractive interaction is between the $\nu g_{9/2}$ and the $\pi f_{5/2}$. While the neutron $g_{9/2}$ shell is filled the $f_{5/2}$ proton shell is pushed down and the energy of the first excited level, of single-particle origin, goes down, as shown in Fig. 2.5. Finally this could lead to an inversion of $\pi f_{5/2}$ and $\pi p_{3/2}$, theoretically expected for ^{75}Cu [97], which would change the spin of the ground state from $3/2^-$ to $5/2^-$, as shown in Fig. 2.6. In a recent experiment at ISOLDE, Flanagan *et al.* [98] measured the spin and the magnetic moment of the ground states of the radioactive ^{71,73,75}Cu with a very good precision. It was indeed shown that the ground state's spin changes to $5/2^-$ for ^{75}Cu.

The copper isotopes are not the only ones where the monopole migration is ruling the evolution of the level structure. When protons are filling the $\pi g_{9/2}$ shell, in between ^{91}Zr and ^{101}Sn, the energy of the single particle levels generated by the neutrons in the $\nu g_{7/2}$ shell drops sharply compared to all the others having $50 < N < 82$. Another example of a neutron state pushing down a proton state is in the antimony (Z=51) chain: when the $\nu h_{11/2}$ is filled, the $\pi g_{7/2}$ is pulled down. The contrary happens in the $N = 83$ isotones, where the $\nu h_{9/2}$ energy decreases with the number of protons occupying the $\pi h_{11/2}$.

This monopole migration for the copper isotopes is supported by two different shell model calculations for the $N = 50$ isotone. The first approach, tried by Ji and Wildenthal [99] adds protons to a ^{78}Ni core, while Sinatkas, Skouras, Strottman, and Vergados [100] (S3V) add holes to a ^{100}Sn core. In both cases, in order to reproduce the structure of the known nuclei, it was necessary to set the $\pi f_{5/2}$ orbital of ^{79}Cu well below the $\pi p_{3/2}$ one. An experimental proof is the observed $3/2^-$ spin for the ground state of ^{85}Br and ^{87}Rb, implying an $\pi f_{5/2}$ orbital already filled and lying beneath the $\pi p_{3/2}$.

A different approach was tried by Oros-Peusquens and Mantica with a particle-core model [101]. Using this model one can extract the exact single particle energies from the experimental data taking into account the quadrupole and octupole interaction (see the last paragraph of 2.1.2). The work of the two authors predicts the $\pi f_{5/2}$ to be 2 MeV under the $\pi p_{3/2}$ for ^{78}Ni. In the already cited work of Flanagan *et al.* [98] a

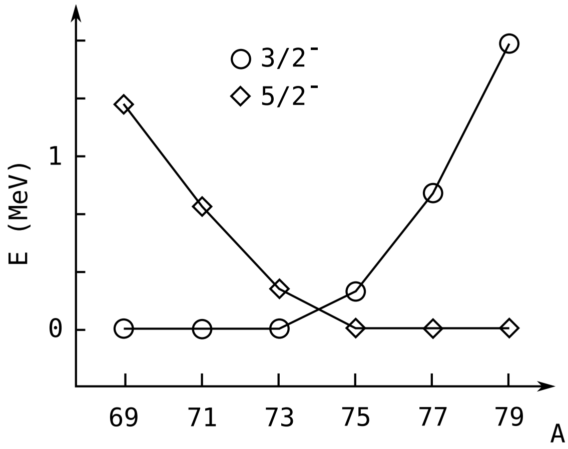

FIGURE 2.6: Energy of the $3/2^-$ and $5/2^-$ levels from S3V shell model calculations. An inversion of the ground state spin is expected after ^{75}Cu. Figure adapted from [87].

very interesting explanation of the nuclear structure of the copper isotopes is made using the synergic interpretation of energy of the states, transition probabilities and magnetic moments. It was observed by Stefanescu *et al.* [86, 102] that the excited $1/2^-$ state's energy drops sharply from ^{69}Cu onwards. While the $5/2^-$ energy drop has been explained with proton-neutron interaction, as shown in this chapter, the $1/2^-$ case can not be interpreted in the same way. The situation gets more clear if the measured magnetic moments are compared to the theoretical ones, as in Fig. 2.7. Starting from ^{69}Cu, which has a ground state of clearly single-particle nature, a good agreement with the effective Schmidt value is expected. In fact, with $g_s = 0.7g_s^{free}$, the experimental value is reproduced perfectly. When more neutrons are added, a deviation of the experimental magnetic moments from the Schmidt limit is observed. For ^{75}Cu the magnetic moment is even lower than the effective Schmidt value for $\pi f_{5/2}$ configuration. This behavior could be explained with an increase in collectivity for the ground state, for which the hydrodynamical limit is $\mu = Ig = I\frac{Z}{A} \approx 1.0\mu_N$ [98]. However, the small transition probability $B(E2; 5/2^- \rightarrow 3/2^-)$ [86] suggests that the collective component is not so developed. Flanagan *et al.* [98] propose a ground state wave function with a single-particle proton state coupled to vibrational excitations, $\pi 2p_{3/2} \oplus \nu(2^+, 4^+)$ for ^{73}Cu with 30% of vibrational component and 86% of protons in the $p_{3/2}$ orbital. Moreover, a lowering of the $\pi p_{1/2}$ state energy would lower the calculated energy for the $1/2^-$, explaining the puzzle of the sudden drop in energy for that state, and would lead to a larger fraction of $p_{1/2} \oplus \nu(2^+)$ configuration in the wave function of the ground state. Consequently, the resulting magnetic moment would be lower as well, explaining its overestimation in the calculations.

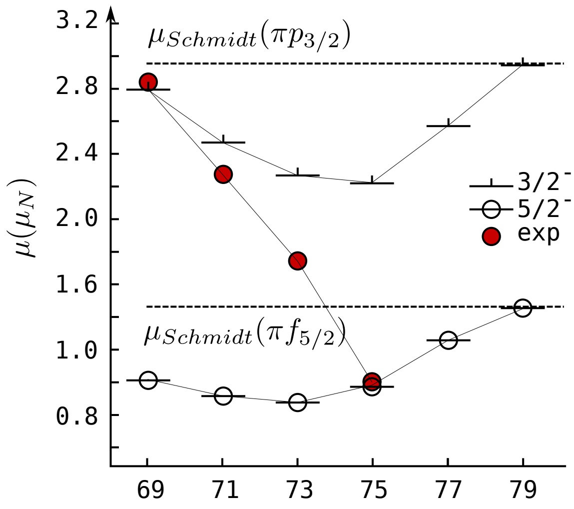

FIGURE 2.7: Magnetic moment of Cu isotopic chain. The dashed lines are the effective Schmidt limits for the two $\pi p_{3/2}$ and $\pi f_{5/2}$ orbitals with $g_s = 0.7 g_s^{free}$, dash and circles are shell model calculations [98] respectively for $3/2^-$ and $5/2^-$ levels, red circles are experimental data. Figure adapted from [98].

2.2.3 The Co isotopic chain: shape coexistence

At $Z = 27$, one proton less than nickel, we have the cobalt isotopic chain. Recently Pauwels *et al.* [103] studied experimentally the neutron rich ^{65,67}Co isotopes in the vicinity of ^{68}Ni. Those data are of great importance for the comprehension of the nuclear dynamics in the region. Cobalt is in the middle of a path that leads from the spherical shape of ^{68}Ni to deformation, first in the excited states of ^{66}Fe and reaching the proposed deformed ground state of ^{64}Cr [104–106]. Pauwels claims that “because the onset of deformation below $Z = 28$ is understood only qualitatively, it is not clear *a priori* how the cobalt isotopes are behaving, since the deformation mechanism depends critically on the values of the $N = 40$ and $N = 50$ gaps”.

The structure of the cobalt isotopes can be explained with a nickel core coupled to a proton hole in the $\pi f_{7/2}^{-1}$ orbital. The spin of the ground state is $7/2^-$ in all cases. Indeed the low energy structure of ^{67,69}Ni and $^{68-70}$Cu is well explained with a coupling between the single-particle valence nucleon and the excited states of the ^{68}Ni core. In Fig. 2.8 the level schemes of the two isotopes are presented, together with that of ^{68}Ni. The first excited level ($1/2^-$ at 492 keV) of ^{67}Co arises from excitation across the $Z = 28$ shell, with a $\pi f_{7/2}^{-2} \pi p_{3/2}^{+1}$ configuration that has no correspondence in ^{68}Ni. Such level is present in ^{65}Co at higher energy (1095 keV). In both isotopes there is a low-lying $3/2^-$ level that is not present in ^{68}Ni and that Pauwels explains as the first rotational band member of the $1/2^-$ proton intruder state. For the neutron-rich cobalt isotopes we have then several spherical states and at least a deformed excited state. This phenomenon is called *shape coexistence*.

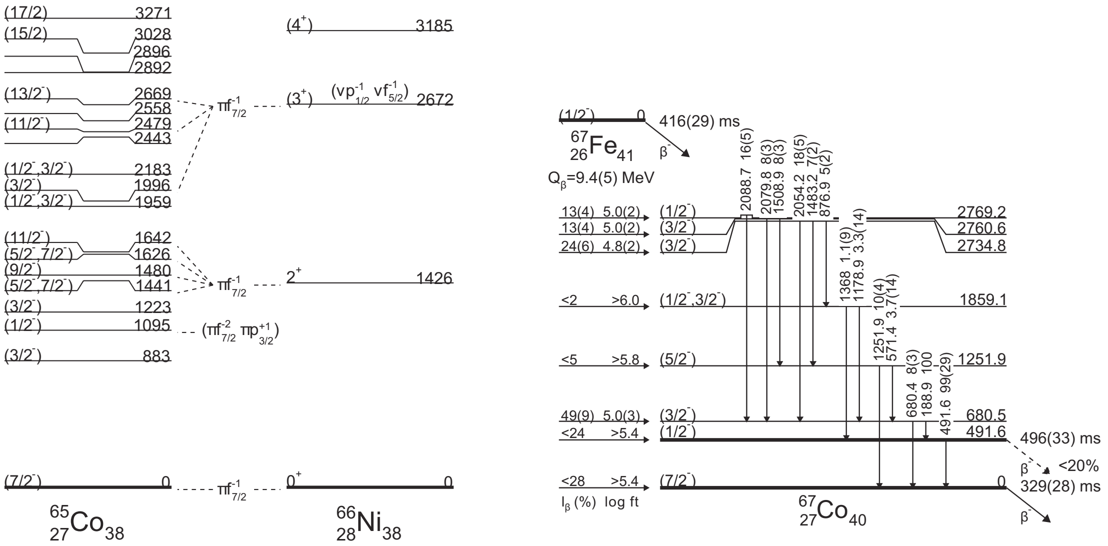

FIGURE 2.8: Co level scheme as reconstructed by Pauwels [103]. On the left the ^{65}Co is presented, together with the ^{68}Ni level scheme for comparison. On the right the ^{67}Co. In both cases are present the low-lying $1/2^-$, explained as proton excitation across the $Z = 28$ shell closure, and the $3/2^-$ (at 1223 keV in ^{65}Co), interpreted as first rotational band of the $1/2^-$ deformed state.

Pauwell concludes the analysis with the remark that the proton intruder configuration is clear evidence for the fragility of the $N = 40$ sub-shell closure.

2.2.4 The Zn isotopic chain: between magicity and collectivity

The zinc ($Z = 30$) isotopic chain is in a transitional region between the spheric nickel ($Z = 28$) isotopes and the deformed Ge ($Z = 32$).

In the region $N \approx 40$ the collective behavior of Ge is well known and is indicated by a low energy of the first excited state and a high transition probability. However, it must be mentioned that a recent work [107] proposed that the shape of ^{74}Ge is more spherical than deformed, while for ^{72}Ge a shape mixing is suggested. The shape of the nuclei is explored combining the results from fusion reactions and Coulomb excitation. These experimental results confirm calculations that were performed in the past with different approaches: Skyrme Hartree-Fock for Dobaczewski *et al.* [108] and relativistic mean field for Sharma *et al.* [109]. Other works [110, 111] propose a shape transition of the ground state with the increment of the neutron number, from spherical (or oblate) for ^{70,72,73}Ge to prolate for ^{74,76}Ge.

For the zinc isotopes the situation is more complicated. A different kind of large-scale shell model (LSSM) calculations were performed in order to obtain a good agreement with the experimental data. While the structure of $^{62-66}$Zn could be explained by LSSM, which does not include the $g_{9/2}$ orbital, it appeared that the restriction of the configuration space to the fp shell orbit should be relaxed and particle excitation across the $N = 40$ shell gap should be allowed with the inclusion of the $g_{9/2}$ orbital in order to reproduce the behavior of ^{68,70}Zn.

Speidel, Kenn and Nowacki [49] and more recently Mücher *et al.* [112] and Moschner *et al.* [113] obtained a good agreement with the lighter Zn-isotope experimental data points considering a ^{40}Ca core with the valence orbitals $0f_{7/2}$, $1p_{3/2}$, $1p_{1/2}$, $0f_{5/2}$. The level scheme and the g-factor are well reproduced while the transition probabilities $B(E2; 2^+ \rightarrow 0^+)$ and $B(E2; 4^+ \rightarrow 2^+)$ are constantly underestimated. This is a sign that some collective mechanisms are neglected. The same calculation foretells an extraordinary uprising of the g-factors of the heavier isotopes, reflecting the sub-shell closure in the limited fp valence space. It appeared obvious then that in order to get satisfactory results for the $^{68-72}$Zn isotopes the $g_{9/2}$ orbital must be included, allowing both for proton and neutron excitation.

A ^{56}Ni core coupled with the $1p_{3/2}$, $1p_{1/2}$, $0f_{5/2}$ and $0g_{9/2}$ valence orbital was then considered. For the heavier isotopes, the agreement with experiment is much better than in the previous case, showing the importance of the $g_{9/2}$ orbital. The energy of the first excited levels and the $B(E2; 2^+ \rightarrow 0^+)$ are also well accounted for. In particular for ^{70}Zn it was noted [112] that ”the wave function that emerge in the present calculation is very fragmented; the 0^+_1, 2^+_1, 2^+_2 and 4^+_1 wave functions have at least 25 different shell model configurations components of over 1% intensity, but no components is as large as 10% in intensity. This fragmentation suggests that the structure of ^{70}Zn approaches that of a collective system with wave functions that incorporate many spherical shell-model configurations”. It was also noted that the number of neutrons occupying the $g_{9/2}$ is much higher than the number of protons, between three and four and 0.13 respectively, making proton excitations less important than what was suggested [114]. The experimental data and the results of the calculations are shown in figures 3.7 and 3.8 on pages 72 and 73.

It can be concluded that neutron excitations through the presumed $N = 40$ sub-shell closure are playing an important role in the zinc isotopic chain, showing the softness of that shell closure. Moreover, despite the sign of collectivity showed by the $E(4^+_1)/E(2^+_1)$ ratio and the transition probability $B(E2; 4^+ \rightarrow 2^+)$, the single particle nature is quite evident, as is expected by a nucleus with two protons out a proton closed shell. For ^{72}Zn we expected increased importance of the neutron $g_{9/2}$ orbital, which, with its negative Schmidt value $g_{Schmidt}(g_{9/2}) = -0.424$, would contribute to a deviation from the Z/A limit. The measurement of this g-factor allows for a more precise determination of the wave function composition, especially of the neutron single particle component.

2.2.5 The island of isomers around ^{68}Ni

It is a well known fact that nuclear isomers appears in the vicinity of closed shells. One famous case is the proton-rich region $N \approx 50$, $40 < Z < 50$, as described in [115]. In this region the isomerism is generated by the $\pi g_{9/2}$ orbital with two mechanisms: *seniority*, with a stretched $\pi g^{n}_{9/2}$ configuration and *single-particle* configuration, when the large spin difference with the $\pi p_{1/2}$ orbital below hinders the decay. In the $N = 50$ isotone, seniority is responsible for the 8^+ isomers in ^{92}Mo, ^{94}Ru, ^{96}Pd and ^{98}Cd while the second one gives rise to the well known $\pi p_{1/2} - \pi g_{9/2}$ $M4$ isomerism.

The interest lying in this region is due to the fact that it is the valence mirror of the neutron-rich region around ^{68}Ni, with protons and neutrons in exchanged roles. This region has been explored later because of the difficulty of producing neutron-rich states compared to proton-rich ones.

The region around $Z = 28$ and $N = 40$ is not an exception, many isomers were identified. In particular, the same 8^+ isomer of the $N = 50$ region was observed in ^{70m}Ni. Such high-spin isomers result from the coupling of two identical particles lying in the same orbital j to the maximum allowed spin of $J = 2j - 1$. In this case two neutrons are in the configuration $(\nu g_{9/2})^{+2}_{J=8^+}$. The reason of the isomerism is the non-collective nature of the state, which means low transition probability, and the small energy difference with the 6^+ state underneath. The same isomer was expected in other nickel isotopes but none were observed. Ref. [116] explains this by a lower-lying 6^+ state generated by the coupling of four neutrons. This state, in ^{70}Ni above the 8^+, offers a favorable channel with a higher transition probability due to the increased collectivity. The predicted lifetime is $\approx$ 6ns, out of reach for most of the currently applied experimental techniques in this region. The second 6^+ is expected to return above the 8^+ in ^{76}Ni, so a strong isomerism is expected to be present again. Indeed an 8^+ isomer with half-life $T_{1/2} = 0.59^{+18}_{11}$ μs was observed in ^{76}Ni [117, 118]. The reasons leading to such different nuclear structure for the nickel isotopes are still unknown. A deeper insight could come from the odd-even nickel isotopes, where a long-lived $1/2^-$ and several short-lived isomers are expected. The same experiment that led to the measurement of the ^{76}Ni isomer [117] could not reveal the existence of any isomer in ^{71,73,75}Ni. The origin of the isomerism for these nuclei is still far from being understood.

Another isomer is found in ^{67}Ni with spin $9/2^+$ at 1007 keV. The g-factor was measured [119] with high enough precision to guess the composition of the wave function. The calculations carried out for the case of a pure single-neutron-hole state in fact were not in agreement with the measured g-factor value, but allowing for proton excitation through the $Z = 28$ shell, with a 2% addition of $\pi(f^{-1}_{7/2} f_{5/2})_1$ to the $\nu g_{9/2}$ state, would be sufficient to obtain a good agreement with the measured g-factor .

The same $9/2^+$ isomer was found in ^{65}Ni at 1017 keV. The g-factor measurement [120] is this time in good agreement with the neutron $g_{9/2}$ orbital g-factor .

The g-factor measurement of two isomeric states in the nickel chain, the $9/2^+$ state in ^{65}Ni [120] and the $5/2^-$ in ^{63}Ni) [121], helps understanding the evolution of the proton $Z = 28$ shell. In both cases the measured g-factors are reproduced with LSSM calculations allowing for proton excitations though the $Z = 28$ shell gap. The results are in agreement with a predominant proton character of the nuclear wave function, showing the extreme fragility of the $Z = 28$ shell closure.

Chapter 3

$g(2^+)$ of neutron rich ^{72}Zn

Le facteur gyromagnétique a sa sensibilité maximale lorsque les particules de valence sont en nombre réduit, voire unique, tel que montré par les valeurs de Schmidt. Pour cette raison, il est intéressant d'explorer les moments magnétiques des noyaux qui sont proches d'une couche externe remplie, parce que dans ce cas la les particules de valence(s) conditionne le comportement du noyaux.

Nous avon choisi la région autour de $N = 40$ *du* ^{68}*Ni en raison de l'incertitude sur la nature de ce nombre semi-magique.* $N = 40$ *n'appartient pas à l'ensemble des nombres magiques original, mais la nature présumée double magique du* ^{68}*Ni a soulevé la question de savoir si ce nombre doit être considéré comme quasi-magique ou si la stabilité accrue est seulement une caractéristique de cet isotope particulier de Ni.*

Le moment magnétique du ^{72}*Zn a été mesurée avec la technique du champe transitoire à haute vitesse. Le premier niveau excité du* ^{72}*Zn a été choisi parce que c'est le premier noyau de la chaîne isotopique à remplir le niveau* $\nu g_{9/2}$ *des neutrons. Tous les* $g(2^+)$ *de Zn connus sont en accord avec la limite hydrodynamique* Z/A*, signe d'un comportement collectif. Différents calculs du modele en couches à grande échelle ont été effectuées pour prédire* $g(2^+)$ *de* ^{72}*Zn et tous s'accordent sur un écart par rapport au limite* Z/A*, un signe que les neutrons dans le niveau* $\nu g_{9/2}$ *jouent un rôle important dans la détermination du comportement du noyau.*

La valeur mesurée pour ^{72}*Zn suggère une légère déviation par rapport à cette limite, qui peut être expliqué avec une configuration dominée par des neutrons. Dans cette expérience, une connaissance approfondie du champ transitoire dans le domaine des haute vitesse en utilisant des ions lourds a également été obtenue. La faisabilité de cette technique pour la mesure des moments magnétiques dans le voisinage de* $Z = 30$ *a été montré, permettant potentiellement la mesure de nombreux états auparavant inaccessibles. Il a été constaté que l'intensité du champ transitoire était beaucoup plus faible qu'attendu. Un effet net nul a été mesurée en utilisant du fer ferromagnétique.*

3.1 Physics case

As explained in Chap. 1.2, magnetic moments are very sensitive to the nuclear wave function composition and to its degree of collectivity. The difference in magnitude of the proton and neutron g-factors makes them the ideal candidates to understand the ratio of the components in the nuclear wave function. The g-factor has its maximum sensitivity when the valence particles are reduced in number, or even only one, as shown by the Schmidt values (section 1.2.2). For this reason it is interesting to explore the magnetic moments of nuclei in the vicinity of closed nuclear shells, because the single valence particle(s) are supposed to rule their behavior. In our case we choose the $N = 40$ region around ^{68}Ni because of the uncertainty on the nature of this semi-magic number. $N = 40$ does not belong to the set of original magic numbers, but the presumed double-magic nature of ^{68}Ni raised the question if this number must be considered quasi-magical or if the enhanced stability is a characteristic only of that particular Ni isotope and is due to different reasons.

The first excited level of ^{72}Zn was chosen because this is the first nucleus of the isotopic chain to fill the $\nu g_{9/2}$ neutron level. All the known $g(2^+)$ of Zn are in agreement with the hydrodynamical limit Z/A, a sign of a collective behavior. Different large scale shell-model calculations were performed to predict the $g(2^+)$ of ^{72}Zn and all of them agree on a deviation from the Z/A limit, a sign that the neutrons in the $g_{9/2}$ level play an important role in determining the behavior of the nucleus.

A detailed discussion of the characteristic of the region and of the results obtained from this experiment can be found in section 3.4.3 in this chapter.

3.2 Experimental set-up

The neutron-rich ^{72}Zn beam was produced by intermediate-energy fragmentation at the Grand Accélérateur National d'Ions Lourds (GANIL, Caen, France). For the experiment we needed a ^{72}Zn beam with an energy of about 40 MeV/nucleon, corresponding to a velocity $v \approx v_K$ where the transient field is expected to exhibit the maximum strength. The intensity and the purity of the beam were also constraining the choice of the accelerator.

Going to the neutron-rich side of the valley of stability is not an easy task since there are essentially only four production techniques:

1. single and multi-nucleon transfer reactions: the disadvantage of this technique is that it does not allow going much further from stability, transferring only few nucleons at most, and that the cross sections are quite low. The big number of

channels opened in the reaction induce a very high background that can make the measurement very difficult;

2. deep-inelastic reactions: in this kind of reaction it is possible to go very far from stability, with the exchange of many nucleons between the target and projectile nuclei. On the other hand, the cross sections are even lower than in the previous case and the background contaminants can compromise the measurement;

3. induced fission and spallation: an intense proton or heavy ion beam is sent on a thick target. In this case a wide variety of nuclei can be produced, but at very low energies. In some facilities the radioactive beam is post-accelerated, like at ISOLDE (CERN), ISAC (TRIUMF) and HRIBF (ORNL), but the obtainable energies, of few MeV/nucleon, are too low to reach the needed velocity, around v_K. Beam intensities are not very high as well;

4. fragmentation reactions: an intense beam of heavy ions is hitting a target and the fragments are selected with a spectrometer. There are few such facilities in the world, but the energy of the fragments is too high (MSU) or even relativistic (GSI, RIKEN) and the ions must be slowed down to enter the transient field velocity regime. This task is very difficult to accomplish and adds a serious challenge to the experiment. At GANIL instead the energy of the fragments was exactly what was needed, with higher intensity compared to the other laboratories.

The GANIL facility met all the requirements for the beam: energy, purity and intensity.

3.2.1 production of ^{72}Zn at GANIL

The radioactive nuclides of interest were produced from the fragmentation of a stable ^{76}Ge beam with an intensity of 1μA. The Ge was accelerated to an energy of 59 MeV/nucleon with the two CSS (Cyclotron à Secteur Separés) and sent on a 500 μm rotating Be target. A wide range of nuclides was produced in fragmentation reactions in the primary target. The nucleus we were interested in was produced with the removal of two protons and two neutrons from the projectiles. The fragments, lighter than the primary beam, continued in the forward direction and entered the Ligne d'Ions Super Epluchés (LISE) spectrometer [122], where ^{72}Zn was selected. After a first $B\rho$ selection with a dipole magnet, a purification of the beam was obtained by means of a 416 μm Be wedge degrader, positioned in the intermediate dispersive focal plane, which allowed for a A/Q selection. The wedge degrader was followed by another dipole magnet. The intensity of the radioactive beam at the secondary target was $2.8{\cdot}10^5$ particles per second and the energy was 38 MeV/nucleon. The purity of the beam was of 75%. A schematic view of the facility is given in Fig. 3.1.

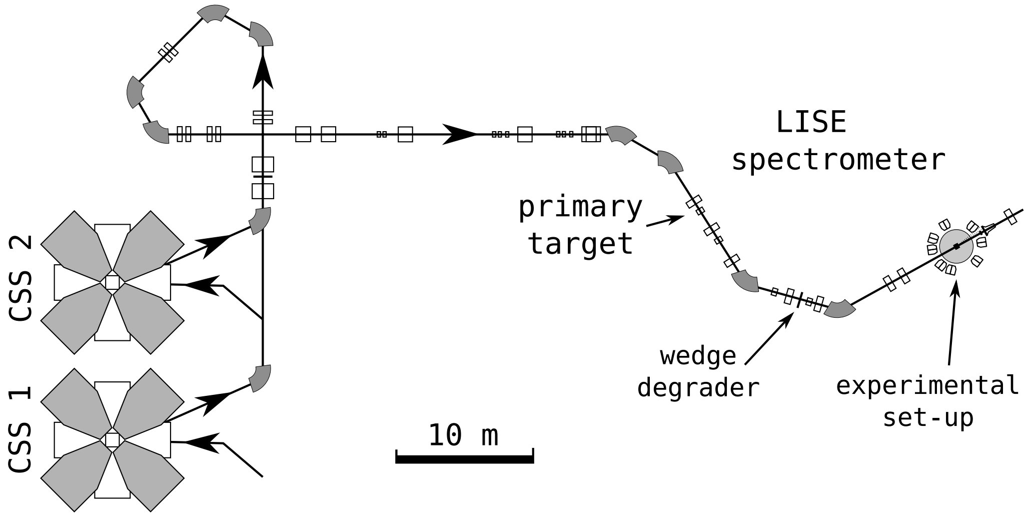

FIGURE 3.1: Accelerators and spectrometer facilities at GANIL. In this experiment we used both CSS cyclotros coupled with the LISE spectrometer.

3.2.2 In the experimental hall

After the selection of the nuclide of interest, the ions interacted with the secondary target. Two targets were used:

1. ^{208}Pb 91 mg/cm^2 layer coupled with a ferromagnetic layer of annealed iron 94.3 mg/cm^2 thick. For a better mechanical cohesion, 300 μg/cm^2 of indium was interposed. The lead layer was used for the population of the 2^+ state via Coulomb excitation, where approximately 60% of the total excitation was taking part. Iron served as ferromagnetic host for the interaction between the excited nuclei and the transient field;

2. single-layer of Gd 204 mg/cm^2 thick, used both for the population of the 2^+ states and as ferromagnetic layer. In order to establish the ferromagnetic properties of the gadolinium, the target was cooled well below its Curie temperature of 282 K [56] by means of liquid nitrogen.

Both targets were polarized with an external vertical magnetic field $B_{ext} \approx 1$ kG provided by an electromagnet. The direction of the field was reversed every 200 s to minimize systematic errors.

The scattered Zn particles were detected with a plastic scintillator detector covering angles between 3° and 5.5° with respect to the beam axis, measured in the laboratory reference frame. This angular-selection of the scattered particles favored Coulomb excitation with respect to Rutherford scattering [123]. Suppression of direct beam ($\theta_p < 3°$)

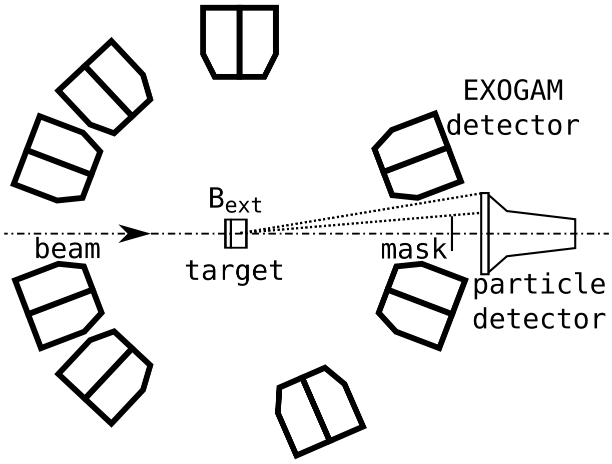

FIGURE 3.2: Experimental set-up, from above. B_{ext} is perpendicular to the page.

was done by placing a mask in front of the particle detector. The upper limit of the angular coverage of the particle detector (5.5°) was chosen in order to select only events of "safe" Coulomb excitation, avoiding impact parameters for which nuclear interaction between the beam and the target can occur.

The angular distribution $W(\theta)$ in Coulomb excitation can be calculated by first principles, as explained in Chap. 1.3, with the only exception of the recoil in vacuum (RIV) component. Selecting only safe Coulomb excitation events allow us to avoid the uncertainties due to the experimental determination of $W(\theta)$.

The target chamber was surrounded by eight EXOGAM detectors [124], fig. 3.2. Each of them is composed of four HPGe crystals with four-fold segmentation. This allows for an enhanced angular granularity and consequently improved Doppler correction. The detectors were positioned in a horizontal plane at distances of 24.5 cm from the target position. The total photo-peak efficiency of the set-up was estimated to be $\varepsilon_\gamma \approx 4.0\%$. Six detectors were placed at angles with the highest sensitivity to the precession effect (refer to Chap. 1.4 for more details) (±25°, ±125° and ±155°) while the two remaining detectors were used for a verification of the angular distribution of the emitted radiation (positioned at +90° and -60°).

The time of flight (ToF) of each event was measured with respect to the radio frequency (RF) of the cyclotron. The data acquisition was triggered by particle-γ coincidences. The ToF allowed us to distinguish between real and random coincidences. Energy and ToF were stored for each event.

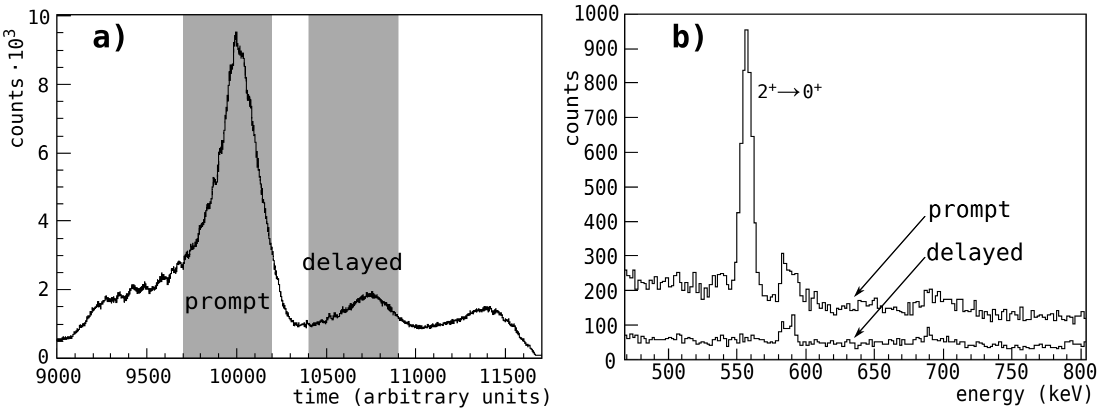

FIGURE 3.3: *a)* Total time spectrum of all the detectors. The two gray zones denote the conditions used in the random event subtraction. The time structure with several small peaks is due to the beam structured in micro-bunches coming every 30 ns where the probability for a random coincidence is higher. *b)* Prompt and delayed Doppler-corrected γ-ray spectra in the ^{76}Ge line. (Full statistics for one detector.)

3.3 Analysis

The aim of the analysis was to measure the intensity of the $2^+ \rightarrow 0^+$ 562 keV transition as a function of the angle of detection θ and of the field direction.

Various techniques were used to enhance the signal-to-noise ratio. Since we were looking for a single γ-ray transition, a γ-ray-multiplicity-equal-one filter was imposed, rejecting the events where high energy levels were populated by reaction mechanisms different from Coulomb excitation. About one-half of the recorded events survived this selection, with an improvement in the peak-to-background ratio of the Coulomb excitation line.

As following step, random event subtraction was performed. Using the recorded timing information, a time of flight (ToF) spectrum was recorded for each of the 32 crystals of the Ge array. In fig. 3.3 *a)* we have a typical ToF spectrum. The ToF is the time difference between the RF of the accelerator and the γ-ray detection and is used to discriminate between real and random coincidences. Looking at the structure of the spectrum, a prompt peak and a random background can be distinguished. Setting the right prompt and delay conditions and gating on them, one can observe in figure 3.3 *b)* that the real Coulomb excitation events are only the ones in the prompt ToF peak and that in the delay-conditioned spectra only the long-lived contaminant peaks are present. As further enhancement, the delayed energy spectrum can be subtracted from the prompt one, a random events subtraction is performed, as well as cleaning the energy spectrum from contaminant lines to get a better peak-to-background ratio.

Finally, the intensity of the photopeak is determined by integrating the line. A background subtraction is performed estimating the background level taking integrals on both sides of the line. The statistics of the crystals with the same θ_γ angle are summed.

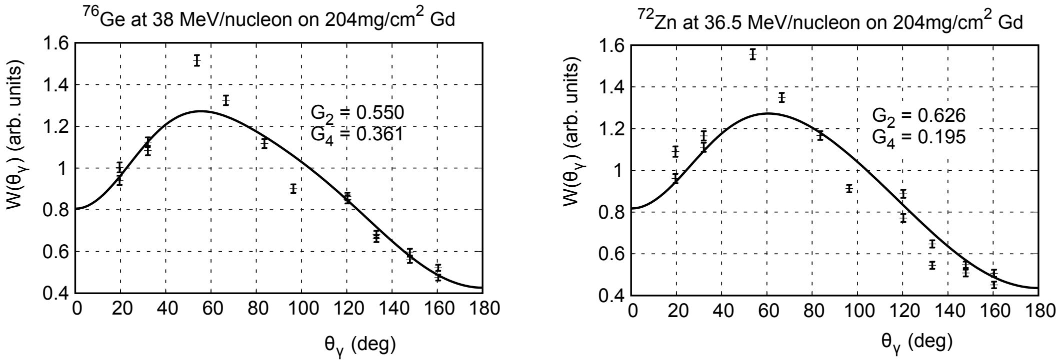

FIGURE 3.4: Angular distribution of ^{76}Ge (left) and ^{72}Zn (right).

3.3.1 Angular correlation

The particle-γ angular correlation for a particle detector with cylindrical symmetry is expressed by the equation

$$W(\theta_\gamma) = 1 + A_2^{exp} P_2(cos\theta_\gamma) + A_4^{exp} P_4(cos\theta_\gamma) \tag{3.1}$$

where $A_{2,4}^{exp} = \rho_{2,4}^0 A_{2,4} G_{2,4}$, as developed in Chap. 1.3. Equation 3.1 is then used to fit the measured angular correlation (fig. 3.4). The agreement between theory and experiment is satisfactory. The only parameters left free are G_2 and G_4, the two recoil-in-vacuum parameters. In Tab. 3.1 we have the comparison between the GKINT values and the fitted ones. The comparison shows that the program underestimates the RIV effect. In fact the program considers as only source of deorientation the ions in H-like and Li-like charge states, for which the electrons are in the ground state. This simplification comes from the assumption that the pairs of electrons, e.g. in He-like ions, couple themselves to a total spin of zero. This assumption, seemingly trivial in nuclear physics, is not always true in atomic physics where electrons often align their spins parallel to the others. This experimental result shows that even the electrons different from the considered ones can have an effect on the deorientation and that the model is too crude.

		theory	experiment
^{76}Ge	G_2	0.891	0.550
^{76}Ge	G_4	0.637	0.361
^{72}Zn	G_2	0.886	0.626
^{72}Zn	G_4	0.619	0.195

TABLE 3.1: GKINT estimations and experimental values for the vacuum deorientation parameters.

	^{76}Ge	^{72}Zn
det	$\Delta\theta$ (mrad)	$\Delta\theta$ (mrad)
1	-21 ± 18	-31 ± 15
2	-18 ± 16	12 ± 16
3	-30 ± 16	-22 ± 18
4	-2 ± 17	0 ± 16
5	-25 ± 22	-13 ± 28
6	-35 ± 17	-8 ± 19
average	22 ± 7	10 ± 7

Table 3.2: Precession angles for the two cases. The first column is the γ-ray detectors couple's index. The difference in magnitude is due to higher velocity and a bigger g-factor for Ge.

3.3.2 Precession angle

Following the steps described in section 1.2.7, the precession angles in Tab. 3.2 are calculated. The slope S is calculated from the angular distribution at the detector angles θ_γ in the nuclear frame.

In order to extract the g-factor from the precession angle, we must calibrate the transient field parametrization with the case of ^{76}Ge and apply it to ^{72}Zn.

3.3.3 Transient field calibration

The transient field parametrization was calibrated using the ^{76}Ge run. The TF strength B_{TF} can be calculated using the formula 1.20

$$\Delta\theta = -g\frac{\mu_N}{\hbar}B_{TF}\Delta t \tag{3.2}$$

where the precession angle, the g-factor of the state and the interaction time are known. The precession angle was calculated in section 3.3.2 to be 22 ± 7 mrad, the g-factor $g(2^+)$ is 0.383(20) [24] and the interaction time is calculated from the kinematics with GKINT to be 2.235 ps. From those values, we get an average magnetic field strength of $\langle B_{TF}\rangle = 0.54 \pm 0.18$ kT. The average velocity, calculated with the GKINT code, is $\langle v\rangle = 0.875 Z v_0$. With the parametrization proposed in section 1.4, Eq. 1.133, the calculated precession angle for g-factor unit $\Phi = \Delta\theta/g$ equals the experimentally determined one $\Phi^{cal}_{Ge} = \Phi^{exp}_{Ge} = 57(18)$ mrad for $A_p = 0.0269$ and $Z_p = 3$. The same parameters were used to calculate the precession effect for the Zn case, giving $\Phi^{cal}_{Zn} = 48$ mrad.

3.3.4 $g(2^+)$ of ^{72}Zn

Assuming that the parameters for the transient field are the same for the two species, we can write the following set of equations

$$\Phi_{Ge}^{cal} = \Phi_{Ge}^{exp} = \frac{\Delta\theta_{Ge}^{exp}}{g_{Ge}} \qquad \Phi_{Zn}^{cal} = \frac{\Delta\theta_{Zn}^{exp}}{g_{Zn}} \tag{3.3}$$

from which we can derive

$$g_{Zn} = \frac{\Phi_{Ge}^{exp}}{\Phi_{Zn}^{cal}} \frac{\Delta\theta_{Zn}^{exp}}{\Delta\theta_{Ge}^{exp}} g_{Ge} \tag{3.4}$$

where the ratio $\Phi_{Ge}^{exp}/\Phi_{Zn}^{cal}$ is 1.18. This difference is due to the different velocity regime of the two ions and the Z dependency of the transient field. The final value obtained for the g-factor is $g_{Zn}(2^+) = 0.21(16)$.

3.3.5 Errors

Two are the causes of the error on the g-factor of ^{72}Zn: *a)* the calibration of the transient field and *b)* the statistical uncertainty on the precession angle in the Zn case. The uncertainty on *a)* have different origins: firstly, the g-factor of Ge as experimentally determined in ref. [24] is 0.383 ± 0.020, a relative precision of 5%.

Secondly, the error on the determination of the precession angle in the Ge case. Here the uncertainty is due to the statistic fluctuations in the peak content and to the error on the determination of the slope S values. The first one introduces a relative error of 48% and can be reduced increasing the collected statistic while the second one is more sensitive to systematic errors. In fact when fitting the measured angular distribution $W(\theta)$ with the theoretical model, from which the S values are calculated, the errors on the fitted factors G_k will introduce an uncertainty σ_S which is not only function of the available statistics but of the quality of the fit as well. σ_S is responsible for an increase of the error on $\Delta\theta$ of the 7%.

Lastly, the Z dependency of the transient field intensity is not well known for such heavy elements. In the B_{TF} parametrization $Z_p = 3$ is assumed, but, as will be shown in chap. 4, the validity of such parameter can be questioned. An error of $\sigma_{Z_p} = 1$ is estimated, which corresponds to a ratio $\Phi_{Ge}^{exp}/\Phi_{Zn}^{cal} = 1.18 \pm 0.24$ and a relative error of 20%. The precision on this calibration can be increased performing more and more experiments with stable beams, probing the transient field strength of heavy elements at high velocities.

The last source of error *b)* is the incertitude on the precession angle in the Zn measurement, for which apply the considerations we did for the Ge case: the statistical error is of 50% while the error induced by σ_S is negligible.

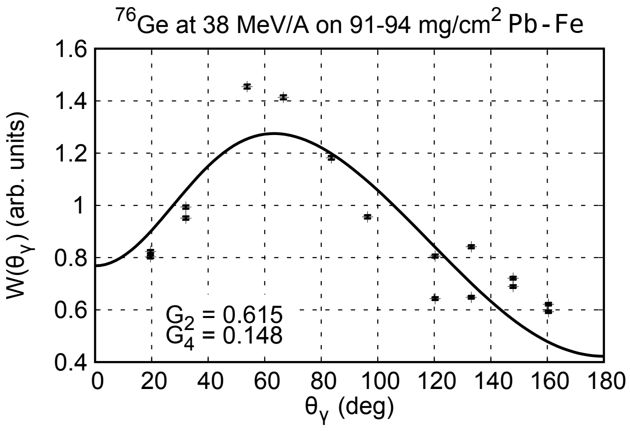

FIGURE 3.5: Angular distribution of ^{76}Ge at 38 MeV/nucleon on the Pb-Fe target.

An increase of statistic of ten times would be required to reduce the error on the precession angle to 20% in the Ge case and of four times to reach the 30% in the Zn case. The actual statistics were collected in 4.5 hours for the Ge (30 hours for the Zn). Running with the same beam intensities as in the current experiment, it would translate to 45 hours of collection for the Ge (120 for the Zn). With the same beam intensity in seven days of data collection the error on the measurement of the *g*-factor of Zn would be reduced to 30% from the actual 110%.

3.4 Results

Aside from the measurement of the unknown *g*-factor of the radioactive ^{72}Zn, in this experiment a deep insight in the high velocity transient field using heavy ions was obtained. The feasibility of this technique for the measurement of magnetic moments in the neighborhood of $Z = 30$ was shown, potentially allowing for the measurement of many states previously unaccessible. With this success, we point out the necessity of having a reliable parametrization of the transient field strength using stable beams. For experiments with radioactive beams it is then preferable to calibrate the parametrization with the same element that will be studied but with one of the stable isotopes, for which is usually possible to get high intensity and a corresponding high precision in the measurement.

3.4.1 Iron target

During the experiment, the lead-iron target was first used because of the technical difficulties with the use of a gadolinium target. In fact, the necessity of an on-line cooling

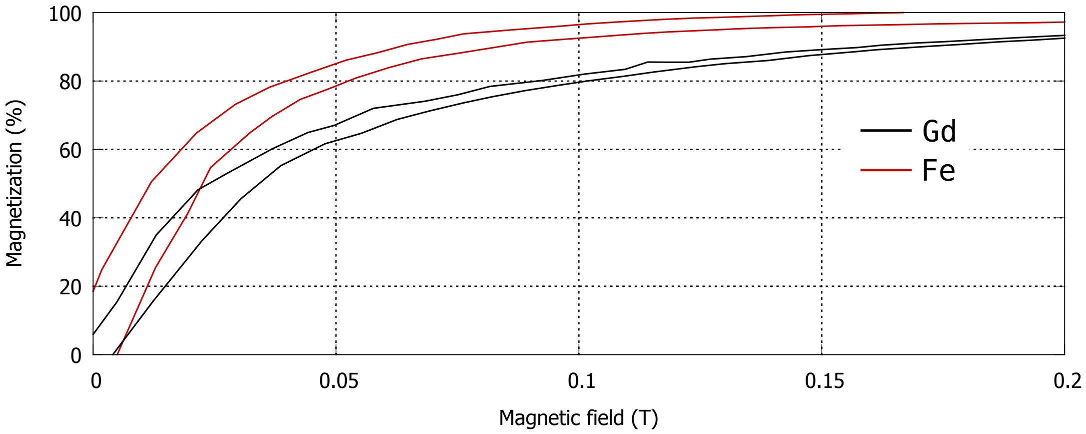

FIGURE 3.6: Magnetization curve for the iron and gadolinium targets used for the experiment, measured at KU Leuven.

and the higher external magnetic field necessary to polarize the material (see figure 3.6 for a comparison between the Fe and Gd targets) made the use of the iron target preferable. In fact, a rough on-line analysis performed during the data-taking revealed that no precession effect was observable.

The accurate off-line analysis carried out later-on showed that despite the favorable experimental conditions, the measured precession effect is compatible with zero. The high statistics allows good precision and, after the same analysis as described for the Gd target, the final result is $\Delta\theta = 2.5 \pm 2.8$ mrad. Assuming a g-factor of 0.397(20), using the weighted average of the two measurements in [125] and [126] and calculating an interaction time $\Delta t = 1.86$ ps, the resulting magnetic field strength is $\langle B_{TF} \rangle = 70 \pm 80$ T. The causes for this result are still to be investigated, but they could be attributed to physics rather than to technical issues.

This result is very important for the development of the TF technique for heavy ions at high velocities, leading to the conclusion that iron is not a suitable ferromagnetic host under this experimental conditions.

3.4.2 Transient field parametrization

While we were studying the feasibility of the experiment, we had to estimate the transient field strength for the Zn and Ge projectiles at high-velocities. As explained in Chap. 1.4, this is due to the impossibility to derive it from first principles and the complete lack of experimental data for a calibration of the parametrization. Although, the TF technique with heavy ions at low velocities is well established, we expected it could be used at higher velocities.

The parameters in [47] were derived as a starting point, even if the experimental data from which they were taken was only composed of light ions, up to $Z = 16$. The author

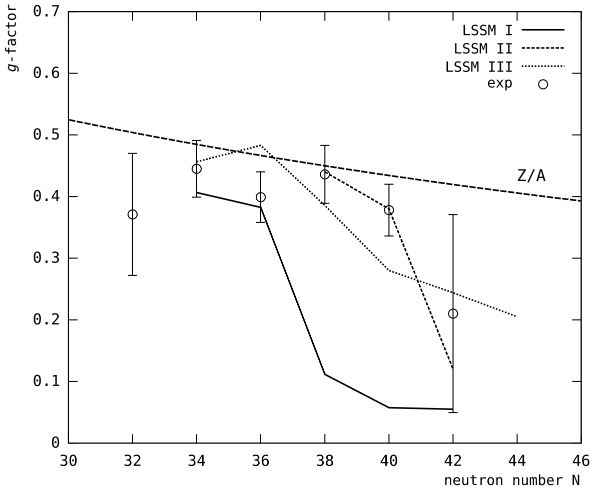

FIGURE 3.7: Large-Scale Shell Model calculations of the g-factors for the first 2^+ state compared to experimental values [127] in the Zinc isotopic chain. In LSSM I [128, 129] and LSSM II [92] a ^{56}Ni core is used with different interactions. In LSSM III [130] the possibility of proton excitations is taken into account via the use of a ^{48}Ca core.

himself warned us that this parametrization should not be used outside of the range of the experimental points. In fact, it was found that the parameters reproducing the observed transient field were much smaller than the proposed ones. Assuming a Z dependence $Z_P = 2$, which suits the gadolinium target for light ions, the intensity is $A_P = 0.35$ instead of the proposed $A_P = 26.7$.

A possible explanation is that for heavy ions, the mechanism of transfer of polarization from the target's electrons to the projectile's, is different than for light ions. This would be due to the fact that the electronic levels responsible for the hyperfine interaction are somehow different in the two cases. Another possible reason lies in the parametrization itself, and particularly in the choice of the Z_P parameter, which carries the Z dependency of the transient field. The chosen value of $Z_P = 2$ suited the region $8 \leq Z \leq 16$ but when going to $Z \approx 30$ the consistency is no longer assured and the deviation can be very important. To explore the , a campaign of exploratory experiments was run as described in the following chapter.

3.4.3 Nuclear structure of ^{72}Zn

Different Large Scale Shell Model (LSSM) calculations were performed to predict the behavior of the g-factor of Zinc as function of the neutron number. They are shown in fig. 3.7. In the first model (LSSM I) ^{56}Ni is considered as an inert core deriving the two body matrix elements (TBME) from CD Bonn interaction. The second (LSSM II) uses the same core but derives the TBME from global fitting of the experimental data in the region. In the third model (LSSM III) the possibilities for proton excitations across the

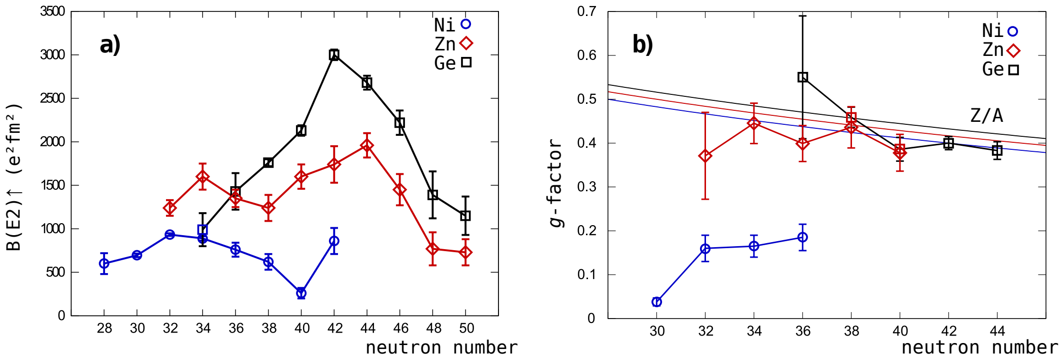

FIGURE 3.8: Transition probabilities $B(E2; 2^+ \rightarrow 0^+)$ [131] *a)* and g-factors *b)* of Ni, Zn and Ge isotopic chains. In *b)* the hydrodynamical Z/A limits are shown as well.

Z=28 shell gap are considered by reducing the inert core to ^{48}Ca. All these models show that a deviation from the hydrodynamical limit Z/A is expected in the region. The main difference between them is where exactly this deviation should take place and how strong it is.

More information can be obtained studying the transition probabilities $B(E2; 2^+ \rightarrow 0^+)$ and the g-factors of the isotopic chains of Ni (Ge), shown in fig. 3.8, which represent two protons less (more) than Zn. Nickel is a closed proton shell, with $Z = 28$. The transition probabilities show two minima, at $N = 28$ and $N = 40$, with typical mid-shell behavior in between. For $N = 42$ the transition probability value is comparable to the mid-shell one at $N = 32$, indicating the strongly localized effect of the $N = 40$ sub-shell closure. The known g-factors present a strong deviation from the Z/A limit [132]. In ^{58}Ni, with only two valence neutrons, this can be explained by neutron excitations [132], while in the heavier isotopes the deviation is mitigated by particle-core excitations [132], due to

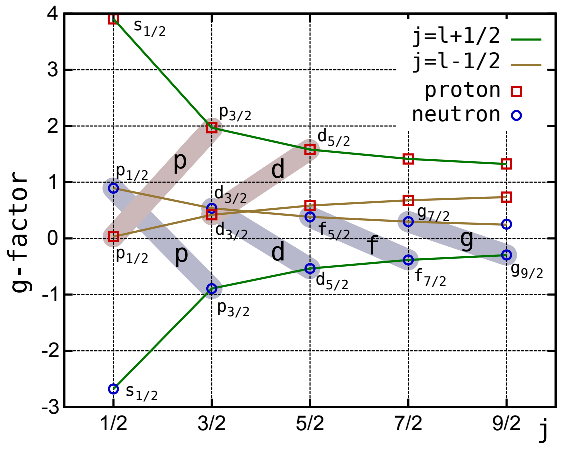

FIGURE 3.9: Extreme single-particle model Schmidt g-factors, from Eq. 1.4 and effective values $g_s^{eff} = 0.7 g_s^{free}$ versus the nucleon total spin $j = l \pm s$. The different levels are indicated.

level	$g_{Schmidt}$ free	$g_{Schmidt}$ eff
$2p^{\pi}_{3/2}$	2.53	1.97
$2p^{\nu}_{3/2}$	-1.28	-0.89
$1f^{\nu}_{5/2}$	0.35	0.58
$2p^{\nu}_{1/2}$	-0.53	0.03
$1g^{\nu}_{9/2}$	-0.43	-0.30

Table 3.3: Schimdt values for the levels filled by the Ni, Zn and Ge isotopic chains. In the *free* column are the results from Eq. 1.4 and free nucleons g-factors from Eq. 1.5. For the *effective* parameters, the g_s is multiplied by a factor 0.7.

the higher number of valence particles. Sorlin and Porquet [93] pointed out that the Ni isotopes do not deviate from a spherical shape, as expected for semi-magical nuclei.

For Ge, the behavior of the state is consistent with the collective model due to the presence of four valence protons and many valence neutrons. The transition probabilities are increasing up to $N = 42$ and then decreasing until $N = 50$, due to the $g_{9/2}$ shell closure. There are no indications of the $N = 40$ sub-shell closure. The g-factors are in good agreement with the Z/A limit [134, 135], with small deviations due to the neutron excitation. Together with the high transition probabilities [136] values and low excitation energy $E(2^+)$, a clear indication of collective behavior is shown.

The behavior of the $B(E2)$ values in the Zn isotopic chain shows similarities with the Ni in the $N = 34 - 38$ region. At $N = 38$ the $B(E2)$ starts increasing and reaches the maximum at $N = 44$. This behavior has been interpreted as the onset of deformation by Leenhardt et al. A sign of $N = 40$ sub-shell closure can not be observed, the only hint being the presence of a local minimum at $N = 38$. The two valence protons are responsible for the higher $B(E2 : 0^+_1 \rightarrow 2^+_1)$ values with respect to Ni. The g-factors are in agreement with the Z/A limit. The measured value for ^{72}Zn suggests a slight deviation from this limit, which can be explained with a neutron-dominated configuration [133]. In fact, the calculated Schmidt values for the levels in the fp shell are all positive while the one of $\nu g_{9/2}$ is negative. With respect to ^{70}Zn, ^{72}Zn starts filling the $\nu g_{9/2}$ level with two neutrons. If, at $N = 40$, a shell-closure is present, the g-factor is dominated by these two neutrons, so it will diverge from $g(^{70}Zn)$. In Tab. 3.3 and figure 3.9 we have the Schmidt values for the g-factors of the levels.

Chapter 4

Development of the HVTF technique for heavy ions

Comme discuté dans le premier chapitre de cette thèse, les champs transitoires à haute vitesse pour des ions lourds est encore terra incognita. *Un certain nombre de questions ont été soulevées par l'observation expérimentale que la force TF pour les ions lourds à haute vitesse est beaucoup plus faible que prévue. Pour clarifier le problème, nous avons proposé de mesurer l'intensité du champ transitoire pour des ions lourds à des vitesses élevées, en utilisant l'excitation Coulombienne en cinématique inverse pour la population du niveau. Le choix s'est porté sur le premier état excité* 2^+ *du* ^{74}*Ge et* ^{78}*Kr. L'énergie du faisceau choisie est de 40≈MeV/nucléon, le maximum réalisable avec le cyclotron du Laboratoire National del Sud (LNS, Catane, Italie). Cette energie est adaptée à notre but car à cette énergie les vitesses des ions sont juste au-dessus de* v_K*. Afin de vérifier les résultats théoriques du chapitre 1, une sélection sur l'angle azimutal de diffusion a été réalisée, à l'aide d'un masque dans l'expérience avec le krypton et avec un détecteur de particules segmenté dans l'expérience avec le germanium. On a découvert que l'alignement du faisceau joue un rôle crucial dans telles expériences et que l'effet du recul dans le vide etait différent pour l'angle azimutal et la polaire.*

4.1 Physics case

As discussed in the first chapter of this thesis, transient fields at high velocities for heavy ions is still *terra incognita*. A number of questions arose after the experimental observation that the TF strength for heavy ions at high velocities is much lower than expected. Speidel *et al.* [55] measured the Cr case and proposed an explanation in terms of beam-induced attenuation [49]. It was suggested that the attenuation is not

		Z	E(2^+) keV	$t_{1/2}$ ps	B(E2;$0^+ \to 2^+$) e^2fm^4	g(2^+)
Run I	^{74}Ge	32	596	12.41(9)	3040(22)	0.43(2)
Run II	^{78}Kr	36	455	21.7(7)	6700(300)	0.43(1)

TABLE 4.1: Characteristics of the probes. The aim was to use a probe heavier than Cr, with well known g-factor, high excitation probability and with a half-life larger than 3 ps. The values are from http://www.nndc.bnl.gov

generated by the probing ion but by the others projectiles and is of dynamic nature i.e. no permanent damage is caused to the ferromagnet. The phenomenon is function of the beam intensity but is not due to thermal effects. However this explanation is not widely accepted. As Stuchbery [47] pointed out, the attenuation could be an effect of the polarization transfer mechanism from the ferromagnet to the probe, which differs for light and heavy ions.

To shed light on the problem we proposed to measure the transient field strength for heavy ions at high velocities, using Coulomb excitation in inverse kinematics. The choices for the probes were the first 2^+ excited state of ^{74}Ge and ^{78}Kr. In tab. 4.1 we summarize the characteristics of the probes: the magnitude of the g-factors, the lifetimes, the 2^+ energies and the excitation probabilities were all satisfying our requirements. The energy of the beam was chosen to be 40 MeV/nucleon, the maximum obtainable with the cyclotron of Laboratori Nazionali del Sud (LNS, Catania, Italy), suitable for our purpose since at this energy the velocities of the ions are just above v_K.

4.2 Experimental set-up

The experiment consisted of two runs, the first one (Run I) in February 2010 with the krypton beam, used seven HPGe detectors and a circular particle detector, and the second one (Run II) held in May 2010 with the germanium beam, employed eight HPGe detectors and a segmented particle detector. The geometry of the two runs is very similar, only major differences in the set-up will indicated.

The accelerated beam from LNS was impinging on the gadolinium target, used both for the Coulomb excitation and as ferromagnet. In both runs, two different target thickness were used: a thick (197 mg/cm^2) target and a thin (79 mg/cm^2) one. In all cases the targets were cooled well below the Curie temperature. In addition, we used during run I the same lead/iron target as in the measurement of ^{72}Zn, to cross-check the results in chap. 3. The target was polarized with an electromagnet providing a field of 1000 G. The direction of the field was reversed every 10 minutes approximately.

The γ-radiation was detected by HPGe detectors placed in the plane defined by the beam direction and perpendicular to the magnetic field. The detectors were pointing at the

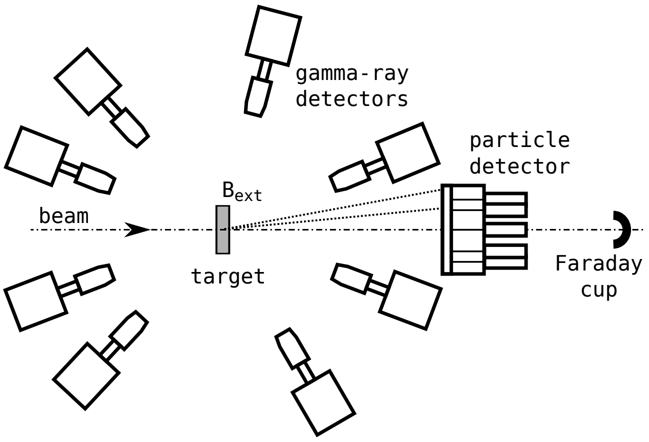

FIGURE 4.1: Experimental set-up of the two experiments held at Laboratori Nazionali del Sud (LNS, Catania, Italy). The external magnetic field for the polarization of the ferromagnet is perpendicular to the page. The annular particle counter allowed for the unscattered beam to pass through and to stop in a passive Faraday cup located further away along the beamline, far from the γ-ray detectors.

target and positioned at a distance of 24 cm (20 cm during run II), as shown in fig. 4.1. The total photo-peak efficiency of the set-up was estimated with GEANT simulations to be $\varepsilon_\gamma \approx 1.0\%$. In run I, six out of seven detectors were arranged in three pairs positioned symmetrically with respect to the beam direction, two at backward angles and one at forward angles, and the last detector was positioned at 60° for a better determination of the angular distribution. During run II, the detector arrangement was kept the same and an eighth detector was added at 75°. The detector pairs were used to measure the precession effect and positioned so as to have the best compromise between the slope and the intensity of the angular distribution $W(\theta)$, while the uncoupled detectors were

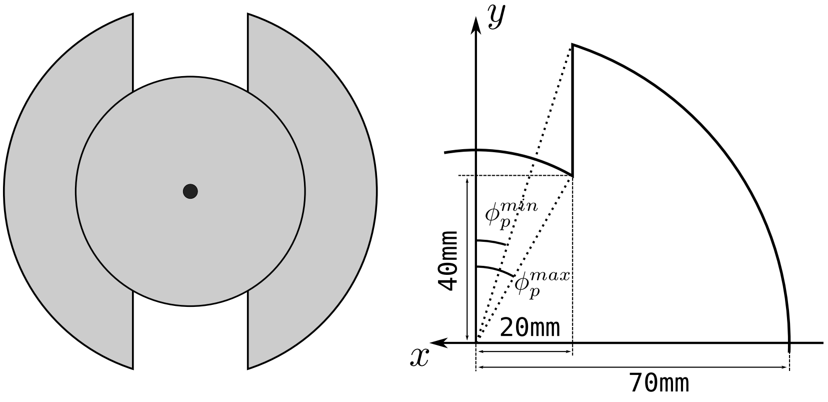

FIGURE 4.2: Run I, particle detector mask. The mask was positioned in front of the 140 mm circular particle scintillator. $\phi_p^{max} = 30°$ and $\phi_p^{min} = 17°$ about the vertical axis.

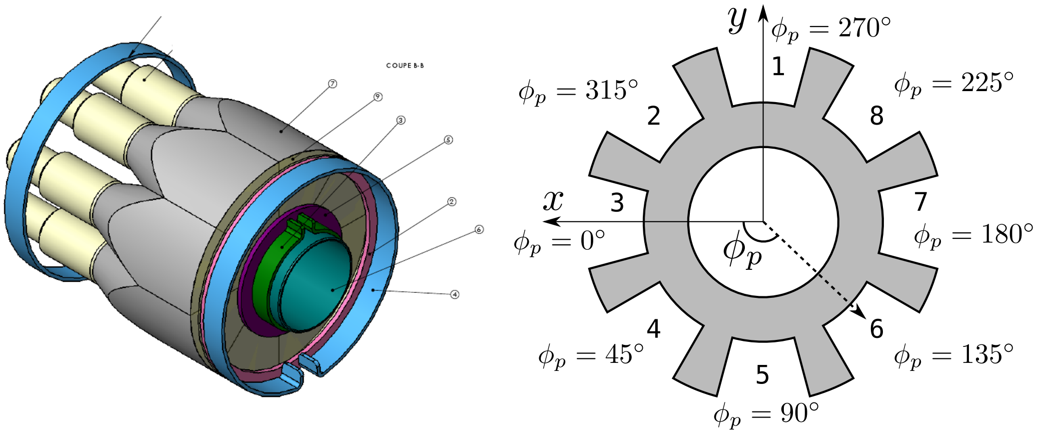

FIGURE 4.3: Run II, particle detector. The ring plastic scintillator was segmented in eight parts, each of which coupled to the photomultiplier with a light guide. On the right, the radial mask used to cover part of the segments and step down the ϕ_p interval to 30°. The design and realization were done at CSNSM.

at angles near the maximum intensity of $W(\theta)$.

Downstream, an annular plastic scintillator counter was used to detect the particles scattered within the interval 4°-6°. The selection on the particle scattering angle θ_p was chosen to ensure safe Coulomb excitation reactions. In this way all possible violent nuclear reactions were eliminated, and the angular correlation of the emitted γ radiation was well determined. The main difference between the set-ups of the two runs was the particle detector. In run I, a 140-mm circular detector was used, as for the ^{72}Zn measurement (chap. 3). An aluminum H-shaped mask was placed in front to protect it from direct, unscattered beam. The mask was also used to perform a selection on the ϕ_p angle. Due to the shape of the cut, the azimuthal opening angle $\Delta\phi_p$ was varying from 60° for $\theta_p = 4°$ to 34° for $\theta_p = 6°$ (fig. 4.2). For run II we used an eight-fold segmented plastic detector (fig. 4.3). A mask in front reduced the angular coverage of each segment from 45° to 30°, to enhance the effect of the segmentation. The annular shape allowed the beam to pass through the detector and to stop in a Faraday cup positioned downstream far from the Ge detectors, in order to decrease the background radiation. The N102 scintillator was 3 mm thick, coupled to Photonis XP1981 photomultipliers.

4.2.1 Electronics and data acquisition

A fully digital acquisition system was used, composed of five TNT2D cards. These cards were designed to work directly with the signals from the preamplifiers of the Ge detectors, sampling the input signals with a frequency of 100MHz, corresponding to a sample each 10 ns. The signal of the plastic detector, only a few ns wide, was shaped with a timing filter amplifier (TFA) to make it long enough to be accepted by the cards. The great flexibility of the cards made it possible to arrange the coincidences between the signals of the eight plastic detector segments and the eight γ-detectors with only one external coincidence NIM module. In Fig. 4.4 the logical scheme of the experiment is presented. In *a)* we have the particle-γ coincidence: each TNT2 card has four inputs and the signals are divided by type: two cards for the eight γ-ray detectors and two for the particle detectors. A card can output the OR of the triggers of the input signals. The particle-γ coincidence is realized taking the OR of the two Ge cards, using an external coincidence module, and using it as gate for the digitally delayed particle signals. In *b)* the procedure to get the magnetic field informations in the data acquisition is sketched. In order to have a pulsed signal that could be used during the data analysis to get informations about the magnetic fields direction, the current out of the magnet was shunted with a proper sized resistance to output +0.8 V (NIM standard) and -5 V (TTL standard), respectively for the two field directions. The TTL was then translated to NIM. The two logical signals were ORed with a 200 Hz pulser supplied by the TNT2 cards themselves and sent as inputs to card n. 5. It can be noted that we were sensitive to the *absence* of magnetic field as well.

4.3 Analysis procedure

The data acquisition (ACQ) system was triggered by γ-particle coincidence, to ensure a pure Coulomb excitation and to clean the energy spectra from the random background. The time difference between the detection of the γ-ray and of the particle was calculated for each event in coincidence. Building the matrix time difference versus Ge energy for each Ge detector-particle segment pair it was possible to estimate precisely the prompt conditions and to cut out all the random coincidences recorded in the coincidence window. The same method was used to gate the energy of the particle detector, cutting out what could be an effect of cross-talk between different segments. This effect was first observed with an alpha source during the test of the detector, when it was also noticed that the ratio between the amplitudes of the two signals generated by the same particle was, in the worse case, of ten to one. It was then judged that this effect was not problematic and that a discrimination of the energy of the particle signal would eliminate it completely. Multiplicity-one filter and random events subtraction following time gating was also performed (refer to section 3.3 for more details.)

Proper efficiency calibration, necessary to obtain a reliable angular distribution, was performed before and after the experiment with a ^{152}Eu source positioned in the reaction chamber at the target position. The activity of the source was such that the average

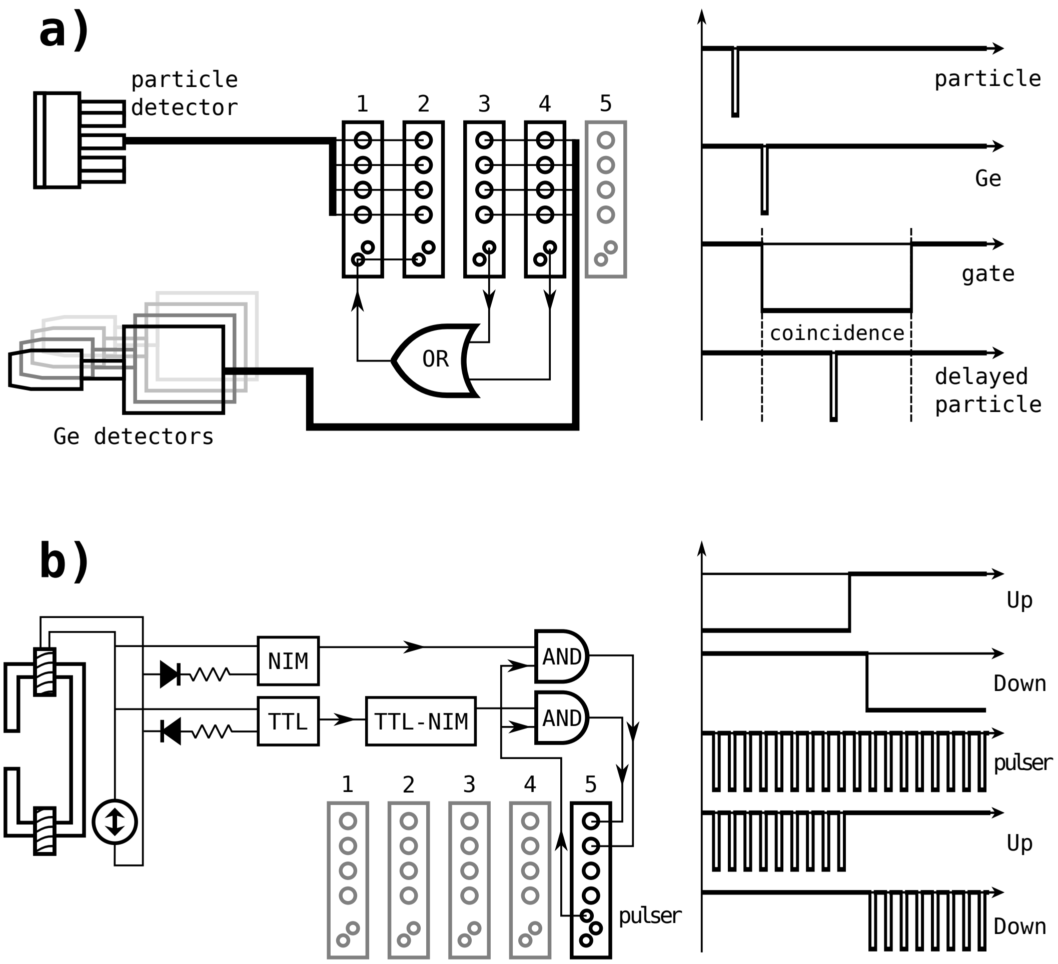

FIGURE 4.4: Logical scheme of the experiment. *a)* γ-particle coincidence: the signal from the particle detector is digitally delayed using a feature of the TNT2 cards. The OR of the Ge detectors open the gate for the delayed particle signal. The width of the coincidence window is 200 ns. *b)* Magnetic field direction information: the current from the coils is shunted and translated in logical signals. These signals are ANDed with a 200 Hz pulser and sent to the TNT2 inputs. The signals are written on disk every 50 ms.

counting rate in the germanium detectors was ≈ 1000 counts per second.

In Fig. 4.5 some examples of time and energy spectra for run I and run II are given.

4.4 Simulations

In chapter 1.3 we calculated the expected angular distribution for the two experiments. Now we shall verify the predictions first comparing the theoretical results to the experimental ones and then fitting the latter ones to obtain the value of the slope S that will

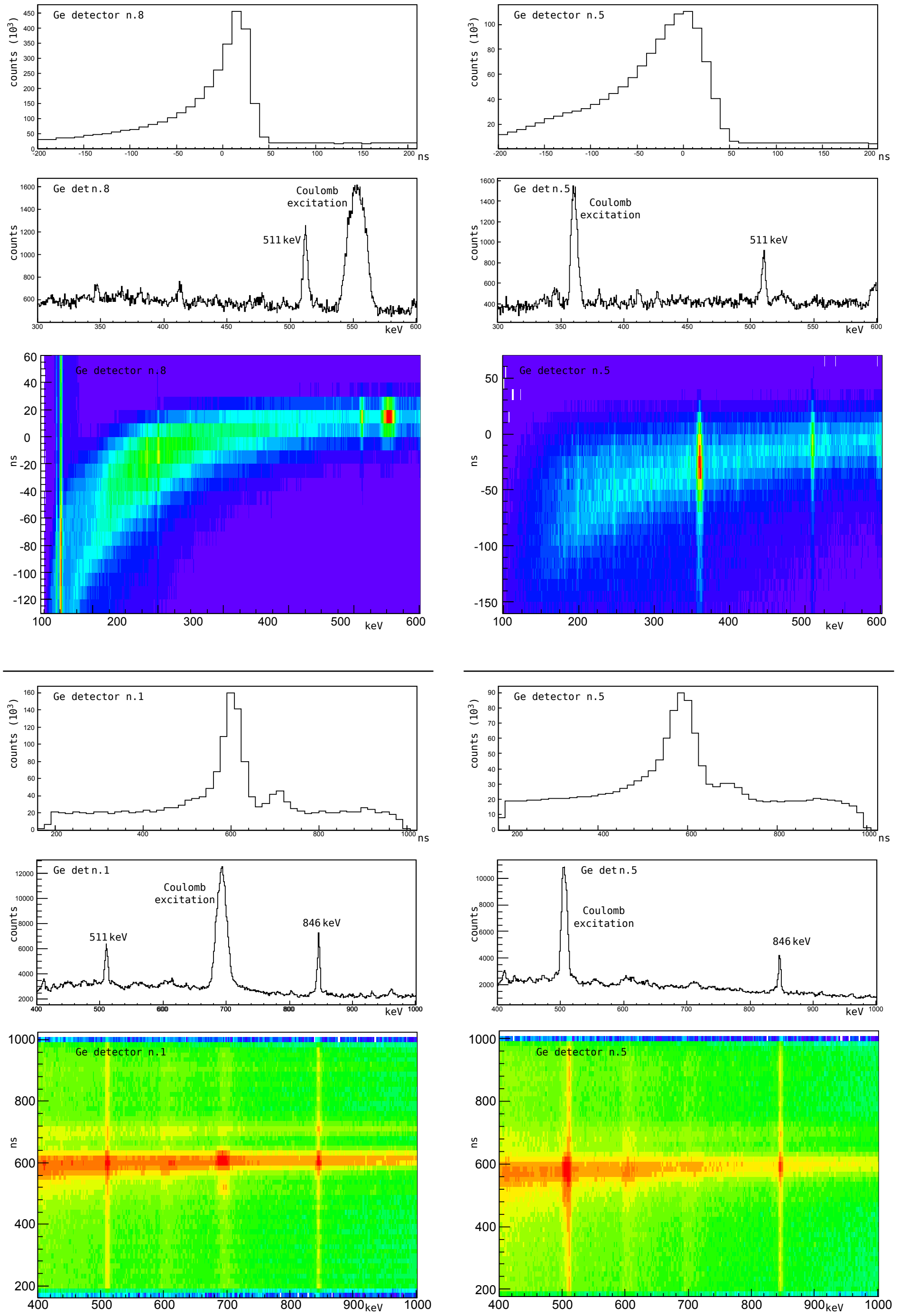

Figure 4.5: Example of spectra for run I (top three rows) and run II (bottom three rows). The column on the left is a detector in forward direction at 30°, the one on the right is in backward direction at 155°. The first rows in each set are the time spectra on which the prompt and random events selection is performed. The second rows are the energy spectra after the random event subtraction. In the last rows are the Energy versus ToF matrices (logarithmic scale on the z-axis for run II).

θ_p	$\Delta\phi_p$	$\langle\Delta\phi_p\rangle$	$\sigma_{theo}^{int\ 1}$ cst/h^4	$\sigma_{theo}^{int\ 2}$ cst/h	$\sigma_{theo}^{int\ 3}$ cst/h
4° - 4.5°	60 ° - 49.8°	55 °	35.6	19.1	16.8
4.5° - 5°	49.8° - 42.6°	46.2°	32.8	17.6	15.5
5° - 5.5°	42.6° - 37.4°	40 °	30.8	16.6	14.6
5.5° - 6°	37.4° - 33.2°	35.4°	29.3	15.8	14

[1] Target: 197mg/cm^2 Gd; [2] Target: 79mg/cm^2 Gd; [3] Target: 91-96mg/cm^2 Pb-Fe;
[4] Counts per hour with a 1000 pps beam.

TABLE 4.2: The four regions of the particle detector used in the simulation of the angular distribution.

lead us to the measurement of the precession angle.

4.4.1 Run I

For the parametrization of the active surface of the particle detector GKINT_phi [28] uses the two angles θ_p and ϕ_p. In our case the used mask lacked radial symmetry, making the calculation not straightforward. The simulation was carried on in separate steps. Four radial regions were defined to approximate the mask's opening (Fig. 4.6). A simulation for each region was run. Two slits were considered, one at $\phi_p = 90°$ and the other at $\phi_p = 270°$. The resulting angular distributions were summed up using as weight factors the correspondingly integrated production cross section. The details of the four regions are in Tab. 4.2. The so-obtained angular distribution was compared to the experimental results (Fig. 4.7). There is a discrepancy between the two, especially for

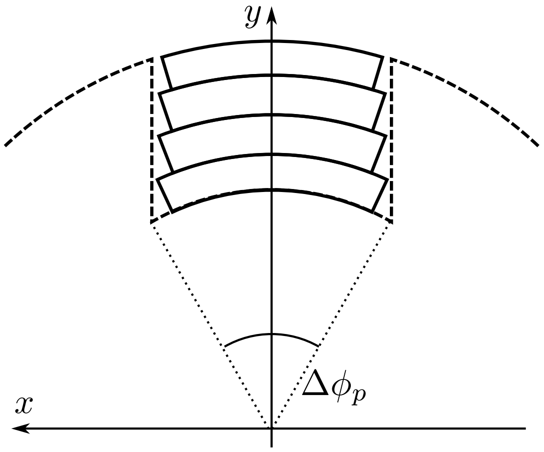

FIGURE 4.6: Run I. Due to the particular shape of the mask in front of the particle detector, with no radial symmetry, the simulation was carried out in two steps. First, four different regions were delineated and a simulation for each region was run. Then the resulting angular distributions were summed up and weighted with their respective integrated cross sections.

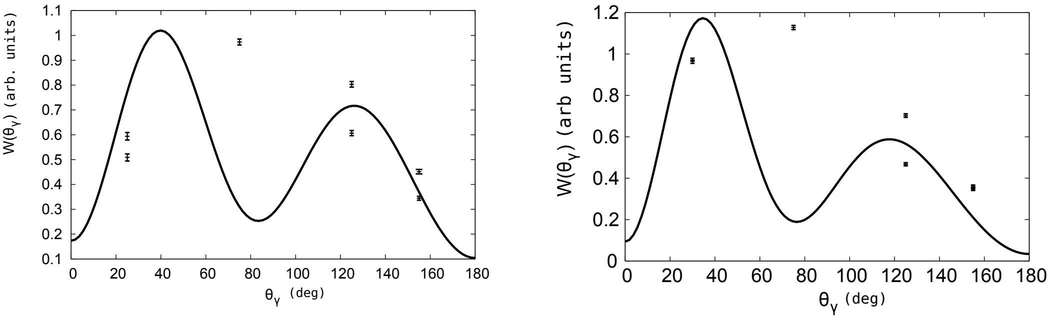

FIGURE 4.7: Run I. Comparison between the calculated angular distribution and the measured one for the thick target case (left) and the thin target (right). The recoil-in-vacuum deorientation parameters G_k are calculated with the program GKINT: $G_2 = 1$ and $G_4 = 1$ for the thick target and $G_2 = 0.881$ and $G_4 = 0.605$ for the thin one.

the point at $\theta_\gamma = 75°$. As determined during the analysis phase, the theoretical angular distribution does not reproduce the experimental results because the effect of the recoil in vacuum on the ϕ angle was considerably underestimated. As thoroughly described in chapter 1.3.7 the azimuthal asymmetry is completely washed out by this effect. An approach to this problem is proposed in section 4.5.2 together with the obtained results.

4.4.2 Run II

The results of the simulations of the angular distribution are shown in Fig. 4.8. We can observe that the selection of the ϕ_p angle has a dramatic effect, leading to major differences from the annular detector case. In particular, in four cases (45°, 135°, 225° and 315°) the angular distribution's amplitudes are larger than in the ring case. The

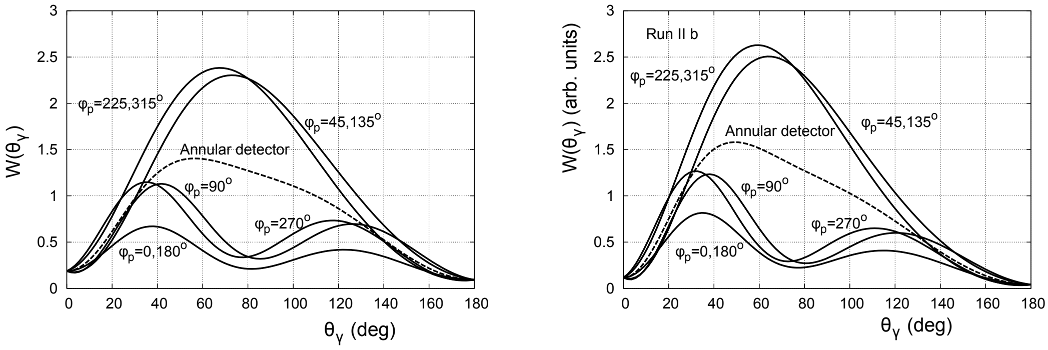

FIGURE 4.8: Calculated angular distribution for run II, the thick target (left) and the thin target (right) simulation. In both cases a mask reducing the azimuthal angle to $\Delta\phi_p = 30°$ was considered. In solid line the segments with the corresponding ϕ_p angle and dashed the annular particle detector case. The system present an up-down symmetry, the angular distributions for the segments' pairs 45°-135°, 225°-315° and 0°-180° are the same.

advantages are a better definition of the angular distribution and the increased slope, which means a bigger effect ϵ. When comparing the experimental results to the simulated angular distributions (Fig. 4.9), the result is clearly unsatisfactory. The simulations show a clear difference between the behavior of the angular distribution for a different selection of the ϕ_p angle. This difference is not observed in the experimental results. For the $\phi_p = 0°, 90°, 180°, 270°$ segments the observed angular distribution shows no 'double-hump' structure, the $\theta_\gamma = 60°, 75°$ detectors being in constant disagreement with the theory. For the diagonal segments the experimental points are in a better agreement with the simulations. The attempt to fit the G_2 and G_4 values was not completely successful, leading to a big $G_2 \approx 1$ and a small $G_4 \approx 0.1$. These two values are in contradiction with the assumption of a static interaction between the nuclear spins and the atomic electrons.

As for run I, the lack of difference in the angular distributions of the different segments can be explained with the RIV effect on ϕ (refer to 1.3.7 for the theoretical approach and to 4.5.2 for the application to the present experiment).

4.5 Experimental problems

During the data taking phase and the following analysis it appeared that a number of technical problems jeopardized the success of the experiment.

4.5.1 Beam alignment

The beam alignment plays an important role in this kind of experiment. In the first run when the target was taken out it was clear that the beam was not centered and was hitting the target frame. Together with the fact that the beam's position and angle at the entrance of the reaction chamber was unknown would result in different ϕ_p angles than the expected ones. Fig. 4.10 *a)* illustrates the problem.

For the second run, where a good definition of the azimuthal ϕ_p angles was very important, a tantalum collimator of 7 mm diameter was put upstream, one meter before the target. A passive Faraday cup was positioned downstream, after the particle detector. Beam transport was performed maximizing the current on the Faraday cup. Unfortunately the current could be measured only without the target in place, so during the data taking the beam's alignment could not be verified. Off-line, it was observed that the beam did not maintain its alignment, but moved. During a period of two hours, chosen randomly among the whole experiment, an estimation from the count rates of the different segments gave a displacement of about 1.5 cm from the center, moving twice

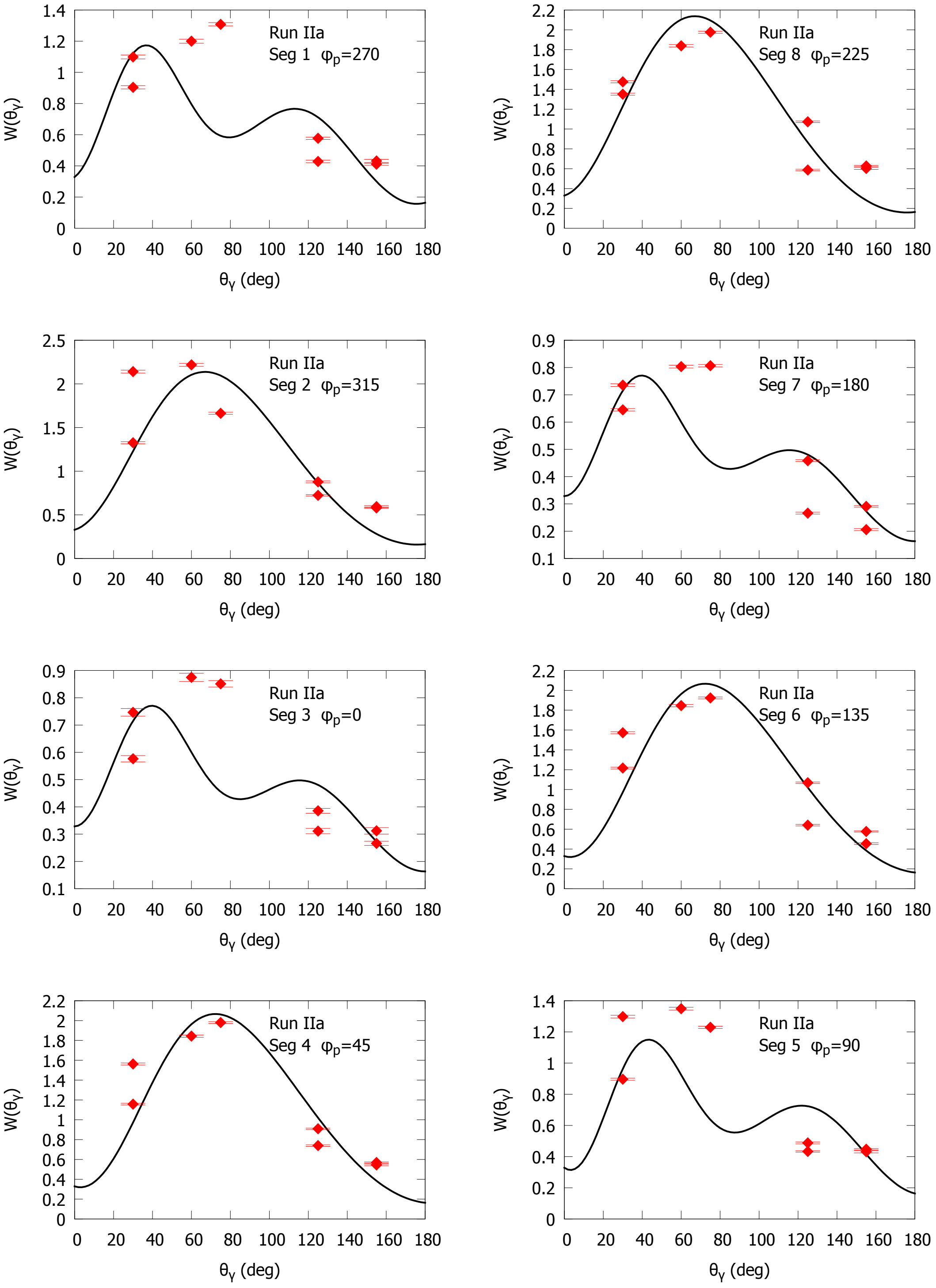

FIGURE 4.9: Angular distribution for run II, thick gadolinium target, per segment (counterclockwise order, top left segment 1 (0°), top right segment 8 (315°)), with recoil-in-vacuum deorientation parameters $G_2 = 0.928$ and $G_4 = 0.764$ as calculated by the program GKINT. The quality of the fit is unsatisfactory for the odd-numbered segments, where the theory fails to describe the experimental points, while it is satisfactory for the even-numbered ones.

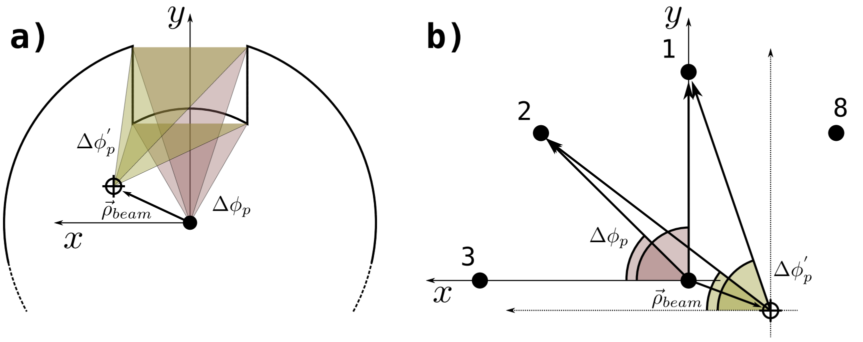

FIGURE 4.10: Effect of a translation $\vec{\rho}_{beam}$ on the beam position. $\Delta\phi_p$ is the expected angle opening if the beam was well centered, while $\Delta\phi_p^{'}$ is the one after the translation. *a)* run I: notice that not only the opening is different but also the two angles defining the interval. *b)* run II, where only four segment centers are shown.

in that time period. In Fig. 4.11 it is possible to observe the count rate as function of the segment number: the beam clearly moved four times at $t \approx 32$, 64, 96 and 128. The movements are illustrated by a variation of the counting rate: when the beam moves further away from segments 7 and 8, it approaches the ones at the opposite side, 3 and 4.

The resulting angles are very different from the expected ones, as shown in Fig. 4.10 *b)* and Tab. 4.3.

4.5.2 RIV effect on ϕ angle

As explained in chapter 1.3.7 the RIV can severely affect the ϕ dependence of the angular distribution. This particular effect was not considered during the preparation of the experiment but was discovered to be very important.

In order to estimate its magnitude, and to check if it is strong enough to destroy the

segment	ϕ_p	$\phi_p^{'}$	$\phi_p - \phi_p^{'}$
1	270°	299°	29°
2	315°	340°	25°
3	0°	13°	13°
4	45°	29°	-16°
5	90°	65°	-25°
6	135°	117°	-18°
7	180°	174°	-6°
8	225°	232°	7°

TABLE 4.3: Effect of a displacement of the beam position -1.5 cm along the x-axis and -0.5 cm along the y-axis. The angles ϕ_p are the expected particle detector segments' angles and $\phi_p^{'}$ the real ones.

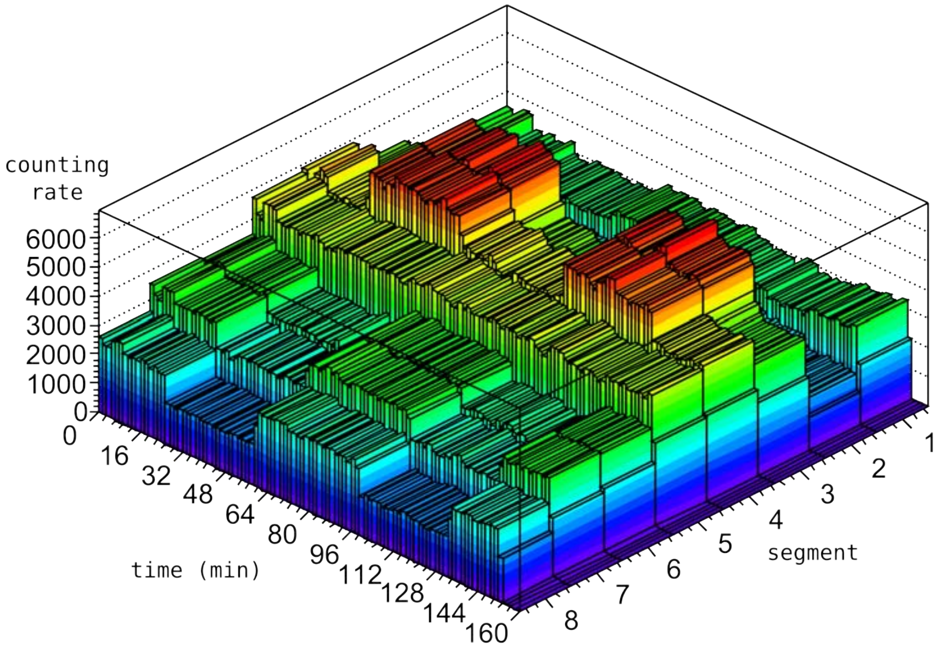

Figure 4.11: Positioning matrix. Counting rate (arbitrary units) as function of the segment number (left horizontal axis) and time (right horizontal axis, in minutes). The beam moves four times, back and forth the same position. These movements are indicated by a variation in the counting rate in opposite segments, here the neighboring pairs 7-8 and 3-4.

information on the ϕ angle, the charge state distribution was evaluated with the program LISE++ [137]. The results are shown in Tab. 4.4. We assumed that the only electrons contributing to the hyperfine field are the uncoupled ones, so for run I only charge states 35^+, 33^+ ... and for run II 31^+, 29^+ ... corresponding to H-like, Li-like and so on. Given the presence of important high-charge-state fractions, we can assume that the dependence of the angular distribution on ϕ is completely lost. It is possible to obtain the resulting angular distribution integrating ϕ. As an approximation, a numerical integration was performed, summing up the distribution calculated at fixed ϕ intervals:

$$W_{avg}(\theta_\gamma) = \frac{1}{N} \sum_{i=0}^{N-1} W(\theta_\gamma, \phi_i) \tag{4.1}$$

where the factor $1/N$ is the normalization. Taking the numerical integration interval $\Delta\phi_i = 10°$ leads to the same results as the simulation of the ring particle counter. The two methods are perfectly interchangeable.

The averaged $W_{avg}(\theta_\gamma)$ represents with a satisfactory degree of precision the experimental results, as shown in the next section.

Run I											
target	thickness mg/cm^2	36^+	35^+	34^+	33^+	32^+	31^+	30^+	29^+	28^+	27^+
Gd	197		0	2	7	18	29	26	14	4	1
Gd	79		17	38	33	9	1	0			
Pb-Fe	94+91	2	12	32	36	16	3	0			
Run II											
target	thickness mg/cm^2	32^+	31^+	30^+	29^+	28^+	27^+	26^+	25^+		
Gd	197	1	5	22	37	26	8	1	0		
Gd	79	7	30	44	17	2	0				
Gd+C	204+2	10	44	38	7	0					

TABLE 4.4: Charge-state distribution of the ions exiting the target, expressed as a percentage. Simulation from the program LISE++ [137] with GLOBAL+Leon code.

4.6 Results

In this section the results of the analysis for the two experiments will be discussed. The analysis was carried out with the technique described in section 1.2.7, with the calculation of the asymmetry and the slope.

4.6.1 Run I

In Fig. 4.12 we have the experimental points with the fitted angular distribution $W_{avg}(\theta_\gamma)$. The fitting function has three parameters: a normalization I and the two recoil-in-vacuum parameters G_2 and G_4 that are printed on the plot. The agreement is satisfactory. The pairs of points at the same angle are the pairs of detectors. Despite the accurate relative efficiency calibration, an asymmetry between the left and right sets of detectors is still present. The reason is most probably in the detector-digital ACQ

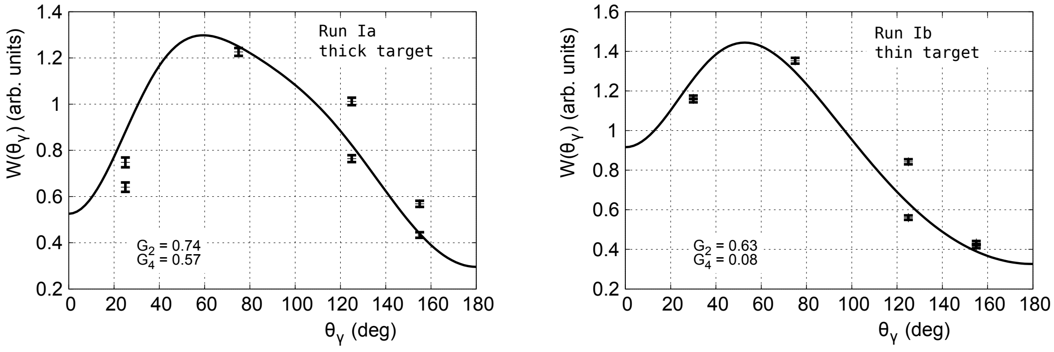

FIGURE 4.12: Angular distributions for run I: ^{78}Kr on Gd, thick target (run I*a*, left) and thin target (run I*b*, right). The averaged angular distribution $W_{avg}(\theta_\gamma)$ has three parameters: a normalization factor I and the RIV parameters G_2 and G_4.

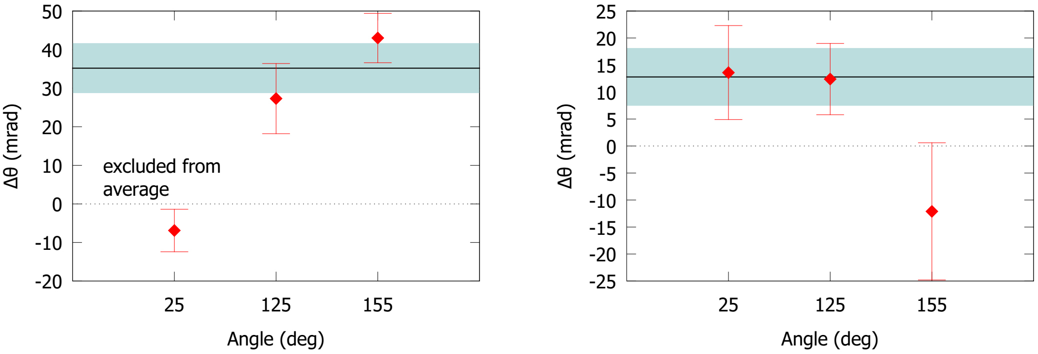

FIGURE 4.13: Precession angles for run I: ^{78}Kr on Gd, thick target (run Ia, left) and Gd thin target (run Ib, right). On the x-axis there are the three detector's pairs' angles. The exclusion of the marked points from the average is due to contaminations.

coupling. The slope S is calculated from the angular distribution at the detector angles in the nuclear reference frame. The measured precession effect is 35 ± 6 mrad for the thick 197 mg/cm^2 Gd target (run Ia) and 13 ± 5 mrad for the thin 79 mg/cm^2 Gd target (run Ib). In Fig. 4.13 the precession angles $\Delta\theta$ as function of the pair's number are presented. In both cases it was not possible to use one of the three pairs of detectors for the determination of the precession angle: in run Ia the Coulomb excitation photopeak detected by the 25° was contaminated by the 511 keV line, while in run Ib the pair at 155° showed a non physical behavior.

The ratio between the two precession effect is in agreement with what is predicted by the GKINT_phi program, which calculated for run Ia a precession angle three times bigger than the one in run Ib. The difference in precession angle is due to different interaction times and velocity ranges.

The average transient field strength is calculated with the formula 1.126

$$\langle B_{TF} \rangle = 0.0209 \frac{\varphi}{g \Delta t} \tag{4.2}$$

with Δt estimated with GKINT_phi to be 2.3 ps and 0.65 ps for run Ia and run Ib, respectively, and $g = 0.43(1)$. The field strengths are $B_{TF} = 0.74 \pm 0.14$ kT and $B_{TF} = 0.97 \pm 0.40$ kT. The averaged field strength, resulting from the weighted average of the two measurements, is $\langle B_{TF} \rangle = 0.77 \pm 0.13$ kT. The average velocity of the projectiles, calculated with GKINT_phi, is $\langle v \rangle = 0.76\ Zv_0$ for run Ia and $\langle v \rangle = 1.01\ Zv_0$ for run Ib. The higher transient field strength observed for Kr with respect to the Ge case, 0.54 ± 0.18 in chapter 3.3.2, is in line with the proposed parametrization (Eq. 1.133) that supposes the transient field to be higher for heavier elements. However, it must be remarked that the measured field is much lower than what theoretically expected, using the parameters for light ions from [47]. This could be due to a different polarization transfer mechanism for light and heavy ions, as supposed in [47]. A possible explanation could be that the

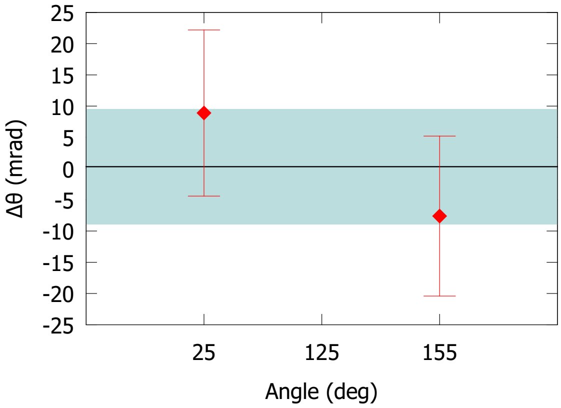

FIGURE 4.14: Precession angles for run I: ^{78}Kr on Pb-Fe target. The point at 125° is not available due to a defection of one of the detector.

transfer of polarization p_{ns}, as parametrized in Eq. 1.128 and supposed independent of the probe velocity, is not correct.

During run I a target with iron as ferromagnetic layer was used. The main reason was to confirm the measurement performed during the GANIL experiment (chap. 3), for which we did not observe any precession effect. In Fig. 4.14 the precession angles $\Delta\theta$ are presented. During the run one of the detector at 125° ceased to work, so no data are available for that pair. The observed precession angle with krypton is 0 ± 9 mrad which leads to a transient field strength of 0 ± 0.22 kT, with an interaction time of 2 ps. The conclusions of the previous chapter about the use of this ferromagnetic host are confirmed: iron cannot be used in high-velocity transient-field measurement with heavy ions. For more details refer to Sect. 3.4.1.

4.6.2 Run II

As in run I we make the distinction between the two targets: the thick 197 mg/cm^2 Gd one (run IIa) and the thin 79 mg/cm^2 Gd one (run IIb). In this run an additional target was used, the 204 mg/cm^2 Gd target backed with a carbon layer used in the GANIL experiment (chap. 3) to which we will refer as run IIc. The angular distributions (Fig. 4.16-4.21) are shown on pages 95-100, at the end of this chapter.
Due to the asymmetry between the intensities of the γ-ray detectors positioned on the right ($\phi_\gamma = 0°$) and the ones positioned on the left ($\phi_\gamma = 180°$), most probably due to a problem between the preamplifiers and the data acquisition, the data needed to be fitted separately.

In Fig. 4.16 we have the right-side detectors of run IIa. With the exclusion of the points at 30° of segment number 2 and 125° of segment 5, for which no reason was found to

explain the deviation from the expected value, the quality of the fits seems satisfactory but in most cases the G_4 values are zero. Excluding the two mentioned segments, the G_2 parameters are quite consistent, with the exclusion of segment 7 for which G_2 is 20% less than the average value $\langle G_2 \rangle = 0.77 \pm 0.07$.
The left set of detector points is shown in Fig. 4.17. The values of G_2 are less consistent than in the previous case. Segment 2 is excluded because the values of the two parameters are at their opposite limits. The averaged G_2 calculated over seven segments is $\langle G_2 \rangle = 0.85 \pm 0.10$. The G_4 values are again all zero. It must be noticed that the Coulomb excitation line in the detector pair at 155° was contaminated with the 511 keV line. Two techniques were used to cure the problem: random-coincidence subtraction, described in Sect. 3.3, and the estimation of the Coulomb excitation/contaminant intensities ratio with a double Gaussian fit. Still the problem was not completely solved because a systematic underestimation of that point by the fitting function is visible.

The fit of the thin target's data (Run IIb) is more satisfactory. Although, the extreme sensitivity of the G_2 values to the point at 30° must be remarked: its value is inversely proportional to the height of the point, e.g. for the right set of detectors (Fig. 4.18) segment 1 the point is high and G_2 low, segment 6 the point is low and the value of the parameter high. This sensitivity makes the parameter spanning widely from a minimum of $G_2 = 0.59$ to a maximum of $G_2 = 0.91$. A similar behavior must be noted for G_4 and its extreme sensitivity to the height of the 130° point. This parameter is responsible for the hump in the region $\theta_\gamma = 100° - 130°$, consequently if the point is higher than expected G_4 will be higher as well. This behavior is particularly accentuated in segment 6 and 7 of the left set of detectors (Fig. 4.19), where $G_4 > G_2$, in contrast with the RIV principles. The averaged RIV parameters for the two cases are $\langle G_2 \rangle = 0.78 \pm 0.10$ and $\langle G_4 \rangle = 0.72 \pm 0.19$ for the right set and $\langle G_2 \rangle = 0.76 \pm 0.09$ and $\langle G_4 \rangle = 0.74 \pm 0.29$ for the left one.

The purpose of the ≈2 mg/cm^2 carbon backing on the thick 204 mg/cm^2 Gd target was to shift the charge-state distribution to higher charge states in order to reduce the recoil-in-vacuum effect. A reliable simulation of this distribution was not possible because the LISE++ routines, and in general all the charge-state distribution codes, assume an *equilibrium charge-state distribution*, that is, the thickness of the layer must be large enough to allow the projectile and the target's atoms to reach an equilibrium in the electron exchange. If within the thickness of the target the equilibrium is not reached, the calculations are not reliable. The points and the fits are shown in Fig. 4.20 and Fig. 4.21. They are not satisfactory in most of the cases, the G_4 values are all zero. The same contamination problem of run IIa for the point at 155° is present, but here the random event subtraction did not work and it was not possible to make an estimation of the two intensity ratios. The average values of the two deorientation parameters are $\langle G_2 \rangle = 0.62 \pm 0.12$ for the right set and $\langle G_2 \rangle = 0.73 \pm 0.10$ for the left one.

It was not possible to observe a precession effect for any target. The calculated ϵ were not consistent between the different angles. In particular, the slope of the angular distribution is positive for the detector's pair positioned at 30° and negative for the two other pairs. This leads to the fact that the sign of ϵ should be opposite in the two cases. Instead, the calculated values are all positive for all the pairs of segments 8,1,2 and 3 and all negative for all the pairs of the segments 4,5,6 and 7.

This behavior can be explained with a different particle detector efficiency as a function of the magnetic field direction. In fact if we write down the Eq. 1.25 considering explicitly a γ-detector pair with efficiency $\eta^{\gamma}_{1,2}$ and the corresponding particle detector segments' pair efficiency $\eta^{p}_{1,2;\downarrow\uparrow}$ we have

$$\begin{aligned}
\rho &= \sqrt{\frac{I_\uparrow T_\uparrow \epsilon_1 \epsilon_{a\uparrow} N^a_{1\uparrow} \times I_\downarrow T_\downarrow \epsilon_2 \epsilon_{b\downarrow} N^b_{2\downarrow}}{I_\downarrow T_\downarrow \epsilon_1 \epsilon_{a\downarrow} N^a_{1\downarrow} \times I_\uparrow T_\uparrow \epsilon_2 \epsilon_{b\uparrow} N^b_{2\uparrow}}} \\
&= \sqrt{\frac{I_\uparrow T_\uparrow I_\downarrow T_\downarrow \epsilon_1 \epsilon_2}{I_\downarrow T_\downarrow I_\uparrow T_\uparrow \epsilon_1 \epsilon_2} \cdot \frac{\epsilon_{a\uparrow} \epsilon_{b\downarrow}}{\epsilon_{a\downarrow} \epsilon_{b\uparrow}} \cdot \frac{N^a_{1\uparrow} N^b_{2\downarrow}}{N^a_{1\downarrow} N^b_{2\uparrow}}} \qquad (4.3) \\
&= \sqrt{\frac{\epsilon_{a\uparrow} \epsilon_{b\downarrow}}{\epsilon_{a\downarrow} \epsilon_{b\uparrow}}} \cdot \sqrt{\frac{N^a_{1\uparrow} N^b_{2\downarrow}}{N^a_{1\downarrow} N^b_{2\uparrow}}}
\end{aligned}$$

where $I_{\uparrow\downarrow}$ is the intensity of the beam current as function of the field direction, $T_{\uparrow\downarrow}$ the switching intervals per field direction, and $N^{a,b}_{1,2;\uparrow\downarrow}$ the number of hits in the photopeak for the pair γ-ray detector 1 and 2 and particle segment a and b. The quantity which we are interested in, and which is proportional to the precession angle, is only the second factor. If the efficiency of the particle detector's segment is not the same for the two field's directions, the double ratio ρ is *not* proportional anymore to the precession angle.

4.7 Conclusions

The transient field strength for krypton ions at high velocity was measured to be 0.74 ± 0.14 kT. We can test the parametrization proposed in [47] comparing the result with the 0.54 ± 0.18 kT obtained using a germanium probe. Of particular interest is the Z dependency of the transient field strength. In Tab. 4.5 the average $\langle B^{theo}_{TF} \rangle$ values are presented for different Z_P values. The values are calculated integrating and normalizing the $B_{TF}(v, Z)$ as presented in Eq. 1.133. We assumed $A_P = 0.0269$ but we point out that A_P cancels when taking the ratio, which is hence independent of A_P. The measured Z dependency is compatible with the $Z_P = 2$ parameter proposed in [47] but a different,

	Z	v_{in} Zv_0	v_{out} Zv_0	$\langle v \rangle$ Zv_0	$\langle B_{TF}^{exp} \rangle$ kT	$Z_P = 2$ kTZ^2	$Z_P = 3$ kTZ^3	$Z_P = 4$ kTZ^4	$Z_P = 5$ kTZ^5
Ge	32	1.05	0.68	0.88	0.54 ± 0.18	15	481	15404	493·10^3
Kr	36	0.94	0.49	0.72	0.74 ± 0.14	15.3	550	19784	712·10^3
				ratio	1.4±0.5	1.02	1.14	1.28	1.44

Table 4.5: Comparison between the Z dependency of B_{TF} as calculated theoretically with the parametrization proposed in [47] (last four colums) and the values calculated experimentally $\langle B_{TF}^{exp} \rangle$. The ratios B_{TF}^{Kr}/B_{TF}^{Ge} are presented in the last row.

higher, value cannot be excluded. We have a match between the experimental ratio and the theoretical one for values between $Z_P = 4$ and $Z_P = 5$.

With these results we have demonstrated the validity of the technique for measuring magnetic moments in radioactive nuclei for heavy ions and the importance of the recoil-in-vacuum effect on the azimuthal angular selection. Nevertheless, it must be pointed out that in some situations the RIV effect is absent, e.g. when the probe is decaying *inside* the target. This is the case of probes with very short life times and/or thick targets. A possible negative side of this case is that the particle decays while slowing down, so the γ-rays are emitted with different values of β and undergo Doppler shifts of different magnitude, resulting in a broadened and asymmetric photopeak, as illustrated in Fig. 4.15. Such is the case for all the 2^+ of the stable even Ni isotopes, which were already measured, or the 2^+ of the supposedly doubly magic ^{68}Ni. When such radioactive isotopes will be accessible for the measurement the HVTF technique could be employed.

It must be emphasized also that the measured values for the recoil-in-vacuum parameters G_2 and G_4 of the second experiment are affected by a number of uncertainties like the

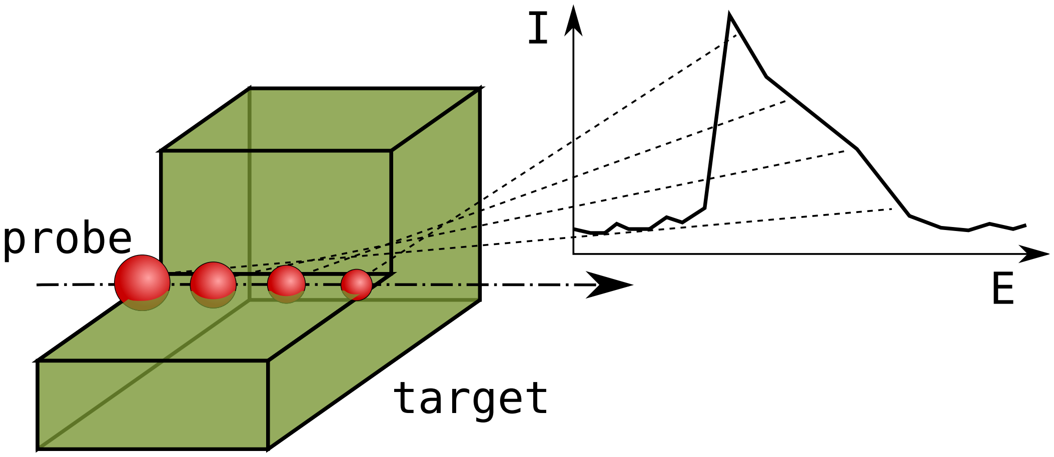

Figure 4.15: A probe with a short lifetime, if allowed to decay completely in the target, will avoid the RIV deorientation effect. The corresponding photopeak will be broadened by the velocity span of the ions in the moment of the decay. The size of the sphere is proportional to the velocity of the probe.

finite beamspot size, the extreme sensitivity to single point's position or the enhanced RIV effect on the ϕ angle. Any meaningful information on the RIV effect is most probably washed out by the otherwise unknown quantities.

The negative result for the use of an iron ferromagnetic target observed in Chap. 3 was confirmed using a different probe. The reason for such behavior is still to be investigated, but it could be due to an uncorrected parametrization of the polarization transfer, the same reason that led to a lower than expected field in the gadolinium target.

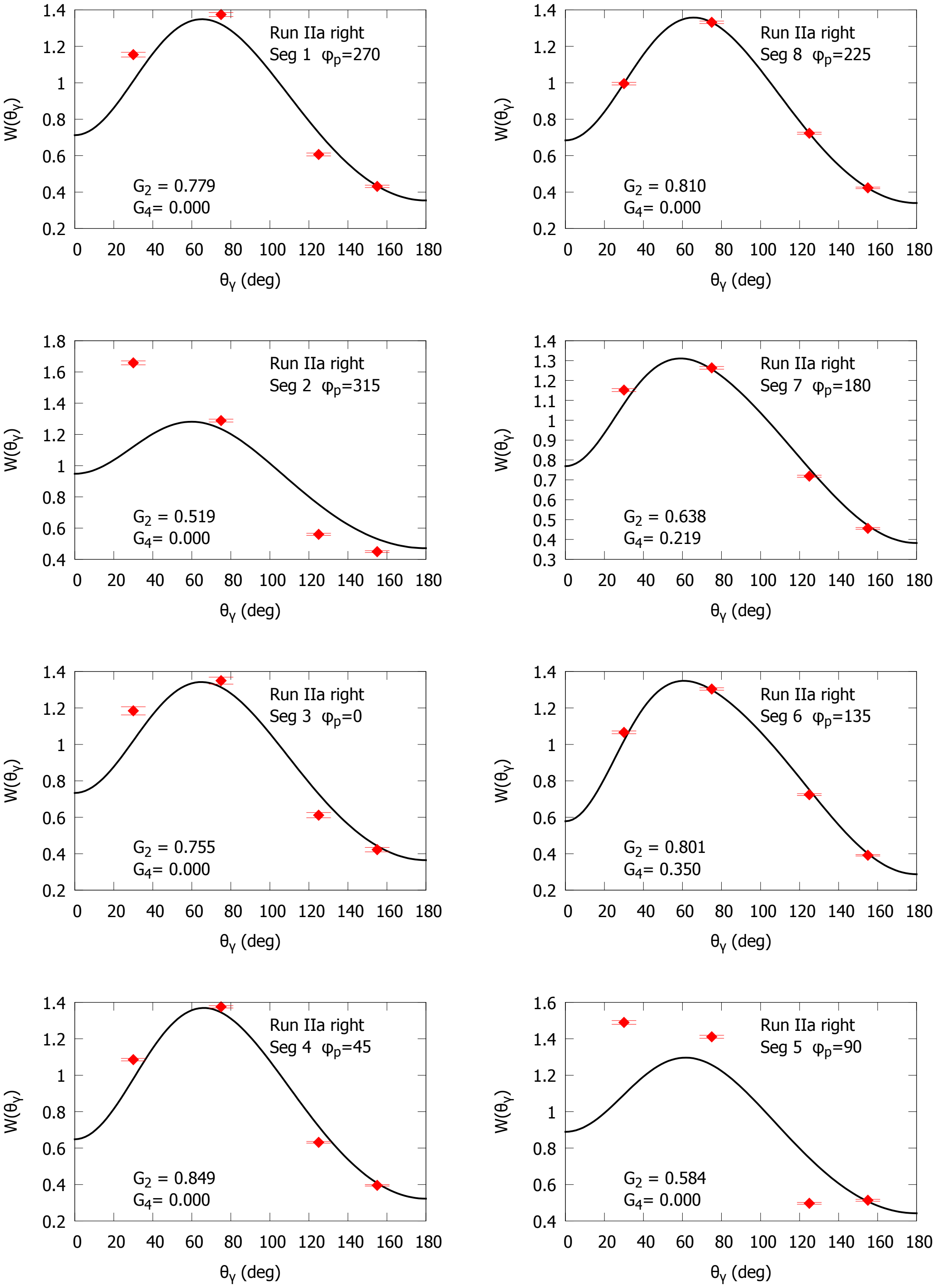

FIGURE 4.16: Angular distribution for run IIa, per segment (counterclockwise order, top left segment 1, top right segment 8), averaged angular distribution Eq. 4.1 for the right γ-ray detectors. The two recoil-in-vacuum deorientation parameters G_2 and G_4 are plotted together with the experimental data and the curve.

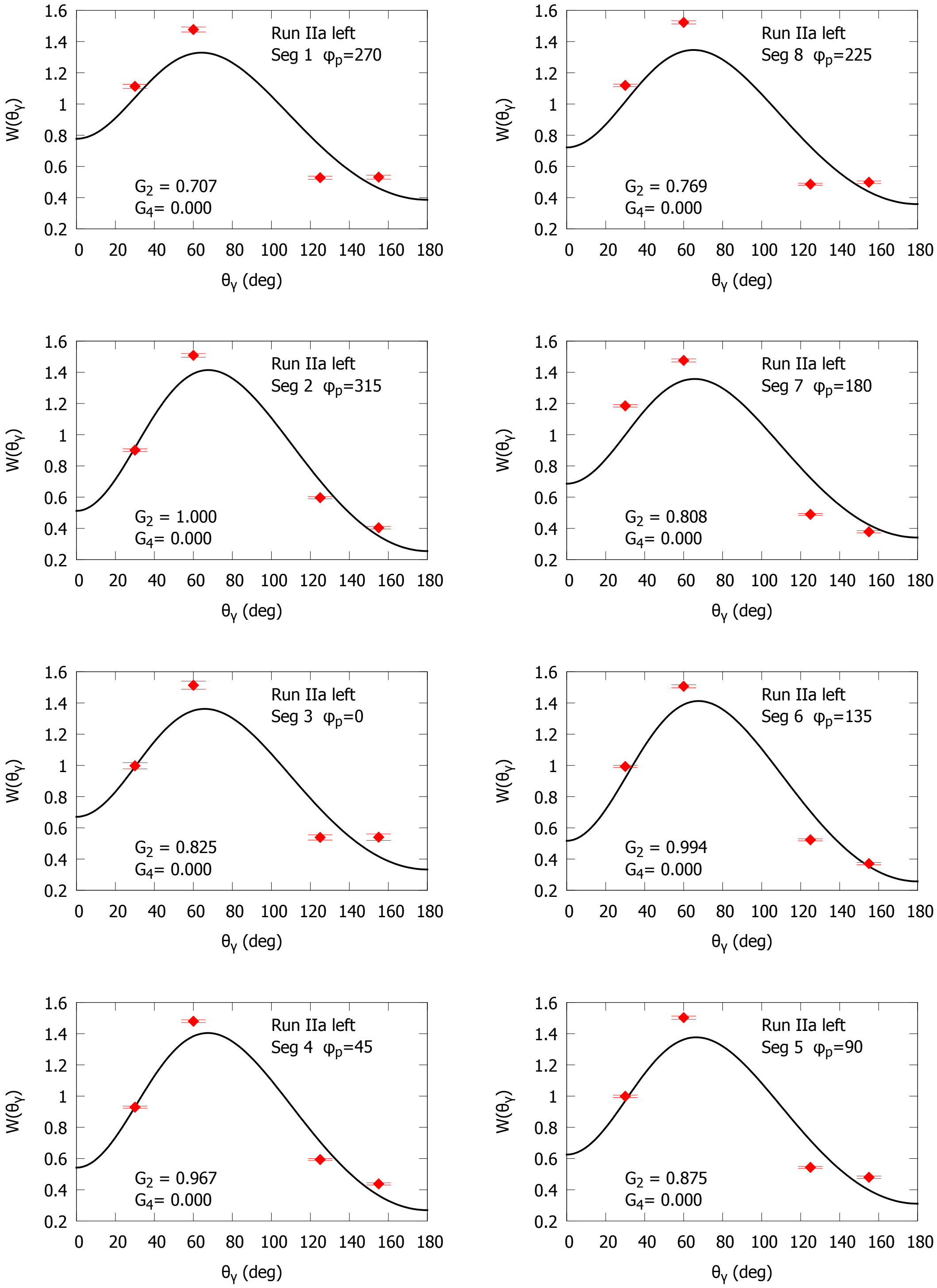

FIGURE 4.17: Angular distribution for run IIa, per segment (counterclockwise order, top left segment 1, top right segment 8), averaged angular distribution Eq. 4.1 for the left γ-ray detectors. The two recoil-in-vacuum deorientation parameters G_2 and G_4 are plotted together with the experimental data and the curve.

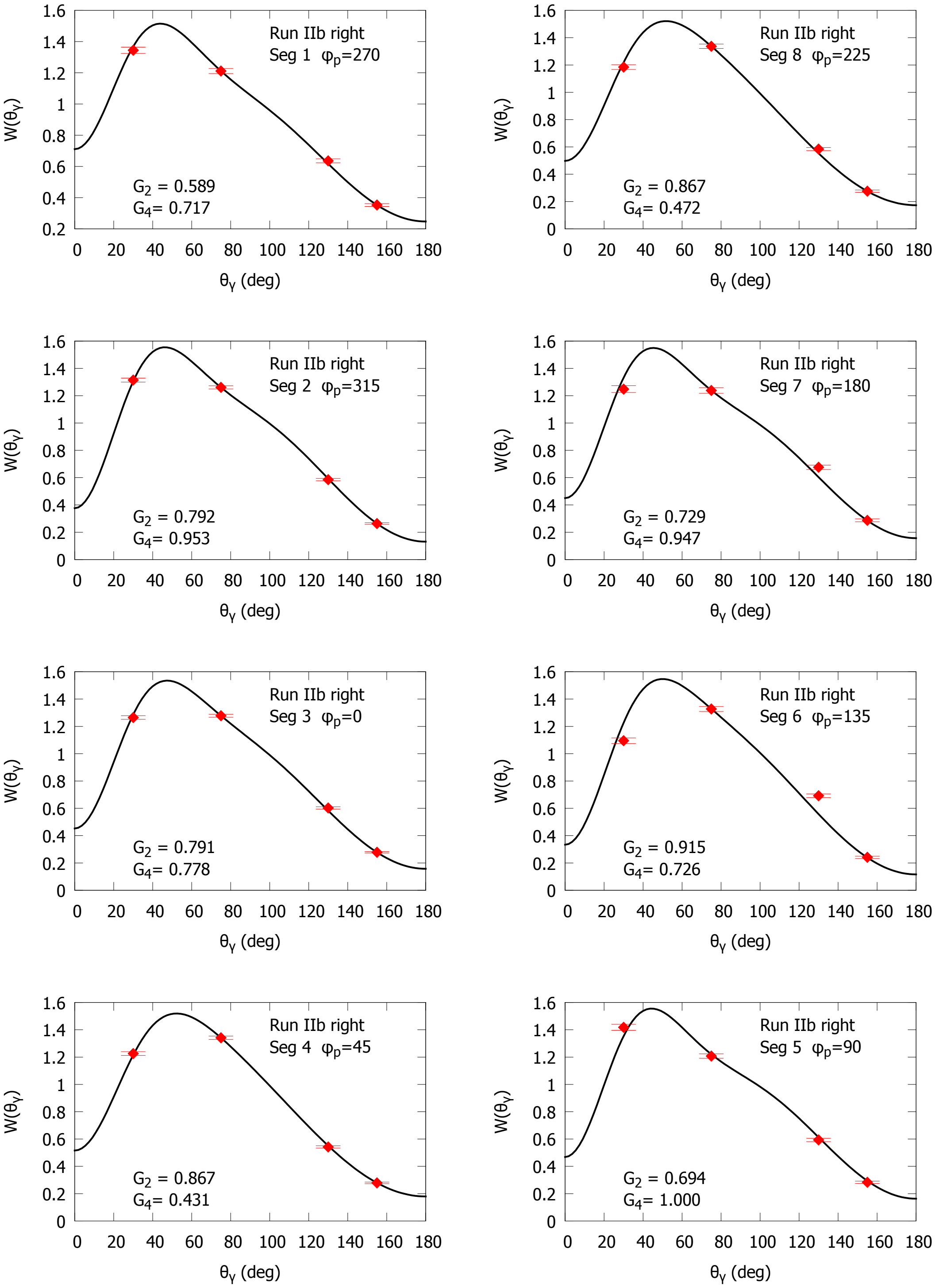

FIGURE 4.18: Angular distribution for run II*b*, per segment (counterclockwise order, top left segment 1, top right segment 8), averaged angular distribution Eq. 4.1 for the right γ-ray detectors. The two recoil-in-vacuum deorientation parameters G_2 and G_4 are plotted together with the experimental data and the curve.

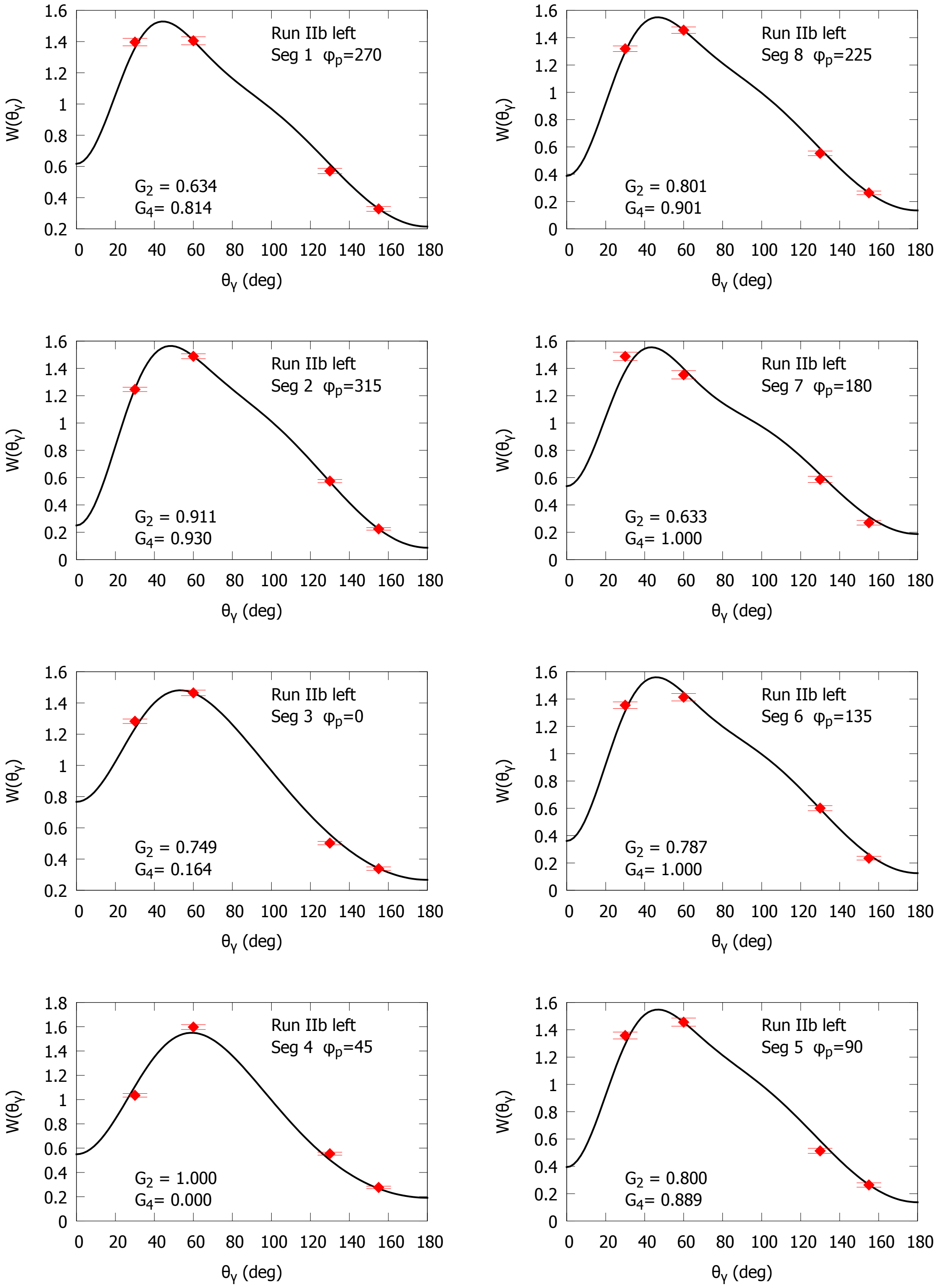

FIGURE 4.19: Angular distribution for run II*b*, per segment (counterclockwise order, top left segment 1, top right segment 8), averaged angular distribution Eq. 4.1 for the left γ-ray detectors. The two recoil-in-vacuum deorientation parameters G_2 and G_4 are plotted together with the experimental data and the curve.

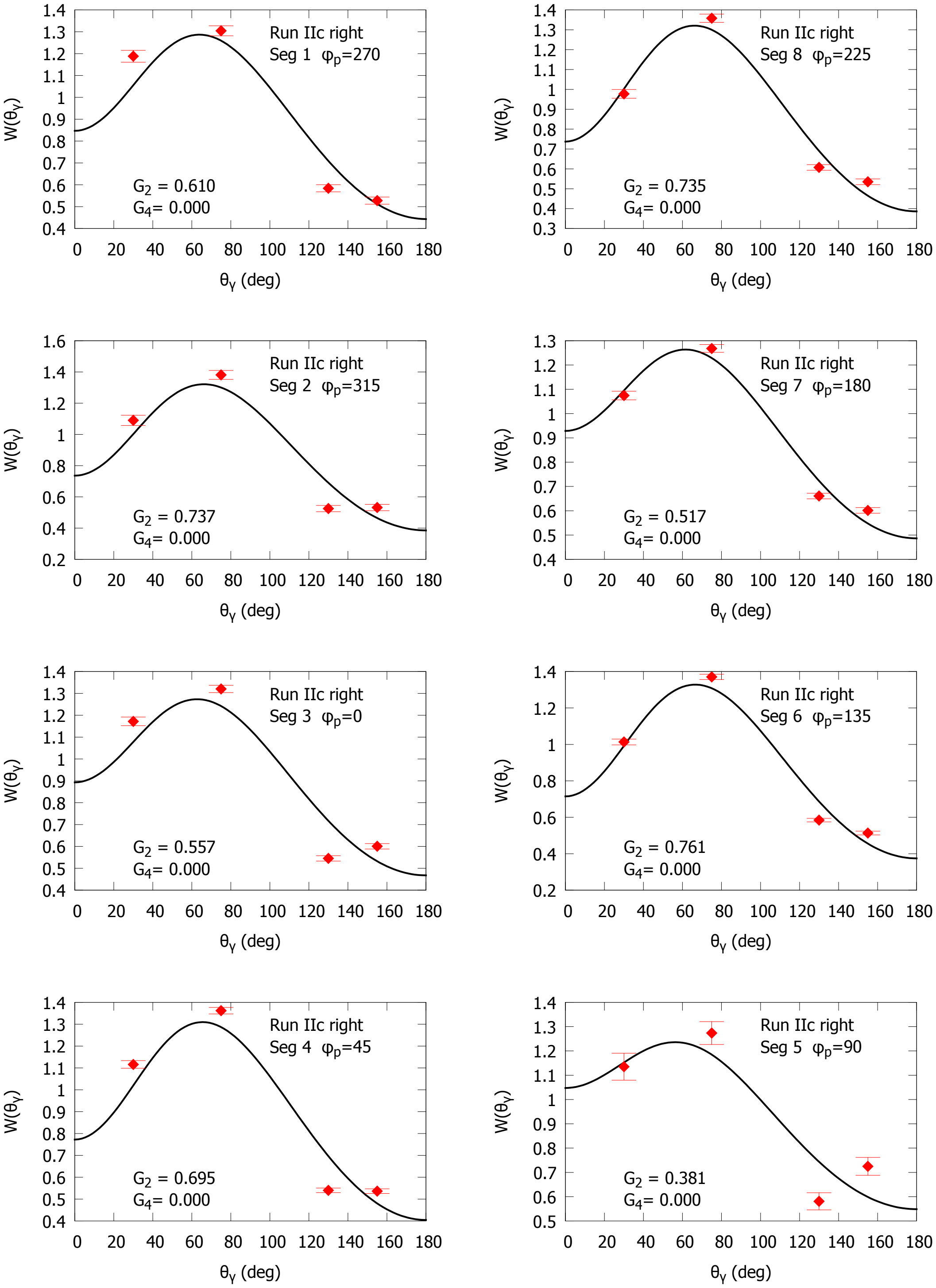

FIGURE 4.20: Angular distribution for run II*c*, per segment (counterclockwise order, top left segment 1, top right segment 8), averaged angular distribution Eq. 4.1 for the right γ-ray detectors. The two recoil-in-vacuum deorientation parameters G_2 and G_4 are plotted together with the experimental data and the curve.

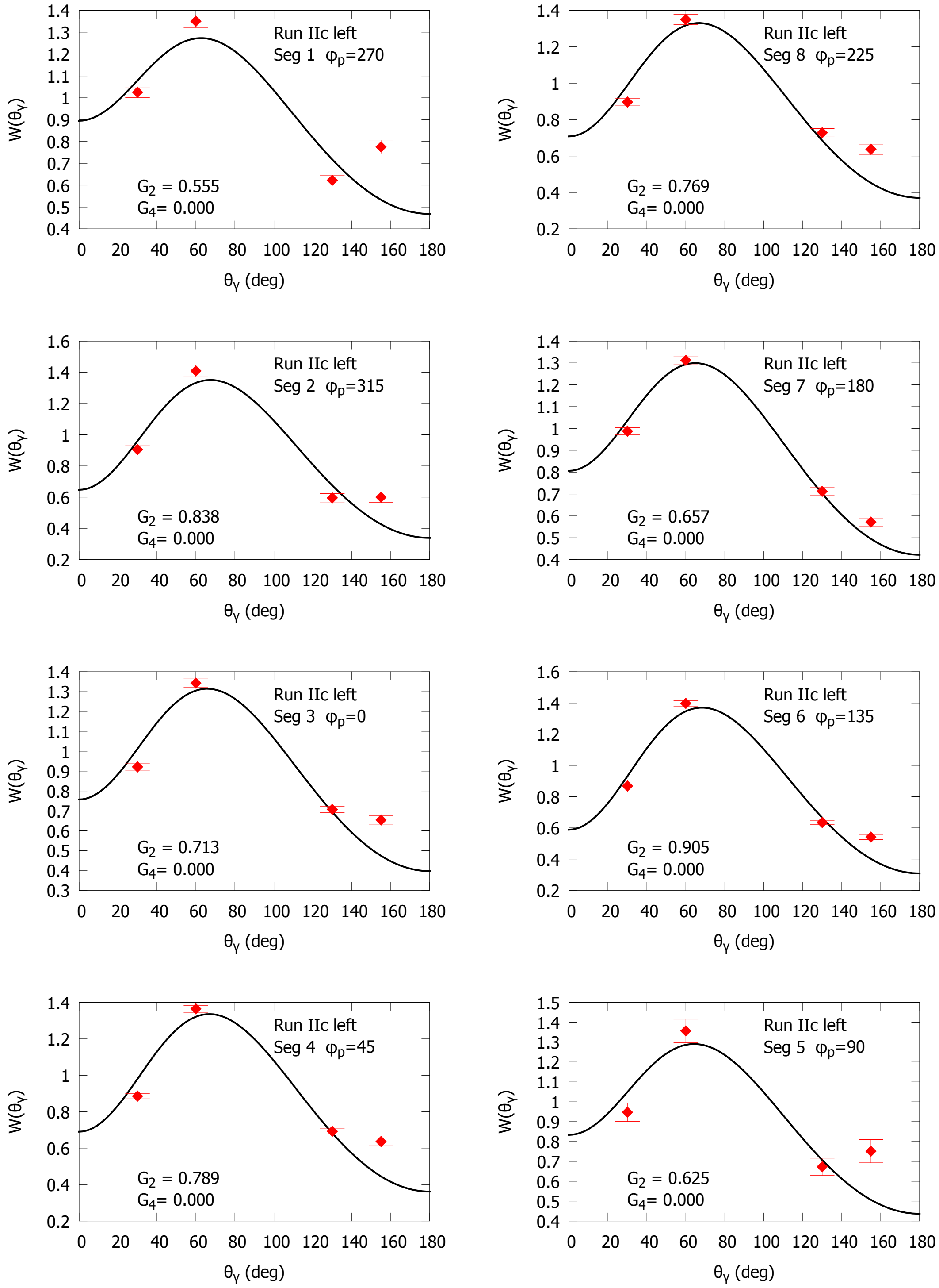

FIGURE 4.21: Angular distribution for run II*c*, per segment (counterclockwise order, top left segment 1, top right segment 8), averaged angular distribution Eq. 4.1 for the left γ-ray detectors. The two recoil-in-vacuum deorientation parameters G_2 and G_4 are plotted together with the experimental data and the curve.

Chapter 5

Summary and outlook

Dans ce travail, la technique du champ transitoire à haute vitesse (HVTF) a été utilisée pour mesurer le facteur g du premier niveau excité 2^+ *du noyau radioactif riche en neutrons* ^{72}*Zn. Une déviation de la limite hydrodynamique* Z/A*, déjà prévue par les différents calculs avec le modèle en couches, est observée. Malheureusement, la précision relativement faible de la mesure n'impose pas une contrainte forte sur la théorie.*

Il a été démontré que la technique HVTF, combinée avec l'excitation Coulombienne, peut être utilisé pour la mesure de facteur g des niveaux de courte demi-vie (10 ps et moin), d'ions lourds ($A \approx 80$*) accelérés à des vitesses relativistes intermédiaires,* $\beta \approx 0.25$.
La principale évolution de la technique est l'augmentation de la vitesse et de la masse du projectile. Cette évolution présente plusieurs avantages. Tout d'abord, l'intensité du champ moyen transitoire peut être plus élevé que dans le cas standard. Cela rend la mesure possible avec de faisceau de basse intensité, ce qui est d'une importance cruciale dans les expériences réalisées avec des faisceaux radioactifs. Deuxièmement, certaines espèces radioactives sont plus facilement disponibles à des vitesses élevées. En dernier lieu, l'énergie plus élevé du projectile permet l'utilisation d'une cible plus épaisse que dans le régime de vitesse standard, conduisant à des taux de production plus élevés et à des temps d'interaction plus long.

L'excitation Coulombienne, utilisée pour la production de l'état excité, a son origine dans la force électromagnétique, et est bien comprise. C'est à dire que la distribution angulaire du rayonnement émis peut être calculé de façon fiable à partir du premier principe. Le développement de cette thèse a consisté en l'exploration de la rupture de la symétrie azimutale du système. Un détecteur de particules segmenté a été conçu. Cette exploration a révélé l'importance de la de-orientation dû à l'effet de recul en vide (RIV). Il a été remarqué qu'on n'observe pas d'effet de précession pour les ions lourds à haute *vitesse lorsque l'on utilise le fer comme hôte ferromagnétique. Par contre, l'utilisation d'une couche de gadolinium a conduit à un effet mesurable.*

La technique HVTF peut être utilisée pour mesurer moments magnetiques des états excités dans les noyaux radioactifs créés avec des vitesses élevées. C'est le cas des faisceaux radioactifs produits au GANIL (Caen, France), à NSCL (MSU, USA), au GSI (Darmstadt, Allemagne) et RIKEN (Tokyo, Japon). Suite aux résultats de cette thèse, une proposition de la mesure des facteurs g des noyaux riches en protons ^{74,76}*Kr a été soumis au GANIL.*

In this work the high-velocity transient-field (HVTF) technique was used to measure the g-factor of the first excited 2^+ state of the radioactive neutron-rich ^{72}Zn.
A deviation from the hydrodynamical limit Z/A that characterizes the g-factors of the first excited states of the zinc isotopic chain, already predicted by different large scale shell model calculations, is observed. Unfortunately the relatively low precision of the measurement of $g(2^+;^{72}\mathrm{Zn})$, mainly due to low statistics, did not allow a strong constraint on the theories.

It was demonstrated that the HVTF technique, combined with Coulomb excitation, can be used for the measurement of g-factors of very short-lived states, with lifetimes of the order of tens of ps and lower, of heavy ions ($A \approx 80$) traveling with intermediate relativistic speeds, $\beta \approx 0.25$.
The standard transient field (TF) technique at low velocities (a few percent of the speed of light) has been used for a long time to provide the strong magnetic field necessary for the measurement of g-factors of very short-lived states. The breakthrough of the present development is the different velocity regime of the higher mass projectile under which the experiment is carried out.
There are several advantages of this technique. First of all, the average transient field strength can be higher than in the standard case. The consequent greater magnitude of the observable, the precession angle, makes the measurement possible with lower counting rate, which is of critical importance in experiments performed with radioactive beams, usually available only with low intensities. Secondly, some radioactive species are more easy available at high velocities, for example at projectile-fragmentation facilities. The problems connected to the slowing-down of the fragmentation products are such that the task hits the technical limit of feasibility. Last but not least, the higher energy of the projectile allows for the use of a thicker target than in the standard velocity regime, leading to higher production rates and longer interaction times.
Coulomb excitation, used for the production of the state of interest, has a well established theoretical background. Since the main interaction is the well understood electromagnetic force, the angular distribution of the γ radiation emitted from the decay of the state

of interest can be reliably calculated from first principles. The development in this thesis consisted in the exploration of the breaking of the azimuthal symmetry of the system. A segmented particle detector was conceived and led to an improvement of the anisotropy of the observed angular distribution, enhancing the sensitivity of the technique. This exploration revealed the importance of the recoil-in-vacuum (RIV) deorientation effect, which in our case destroyed the effect of the particle detector segmentation.

Nevertheless, the development maintains its importance in cases where the RIV effect is not present, as in the case of ps lifetime states when the probe decays inside the target.

Iron has been used as a ferromagnetic host in transient field measurements since the very beginning. In the experiments performed here, it was remarked that no precession effect could be observed for heavy ions at high-velocity using such ferromagnetic host. Instead, a gadolinium layer led to a measurable effect.

The high-velocity transient-field technique can be used to measure g-factors of excited states in radioactive nuclei created with high velocities. This is the case of radioactive beams produced in fragmentation reactions at GANIL (Caen, France), at the radioactive beam facility at NSCL (MSU, USA), at GSI (Darmstadt, Germany) and RIKEN (Tokyo,Japan). Following the results of this thesis, a proposal for the measurement of the g-factor of the proton-rich ^{74,76}Kr was submitted at the GANIL PAC.

Bibliography

[1] Peter J. Mohr, Barry N. Taylor, and David B. Newell. CODATA recommended values of the fundamental physical constants: 2006. *Rev. Mod. Phys.*, 80(2):633–730, Jun 2008. doi: 10.1103/RevModPhys.80.633.

[2] W. Pauli. Über den Einfluβ der Geschwindigkeitsabhängigkeit der Elektronenmasse auf den Zeemaneffekt. *Zeitschrift für Physik A Hadrons and Nuclei*, 31(1):373–385, February 1925. ISSN 0939-7922 (Print) 1431-5831 (Online). doi: 10.1007/BF02980592. URL `http://www.springerlink.com/content/e6631774u53u8841/`.

[3] G. E. Uhlenbeck and S. Goudsmith. Spinning electrons and the structure of spectra. *Nature*, 117(2938):264–265, 1926. doi: 10.1038/117264a0. URL `http://www.nature.com/nature/journal/v117/n2938/pdf/117264a0.pdf`.

[4] E. L. Brady and M. Deutsch. Angular correlation of successive γ-rays. *Phys. Rev.*, 78(5):558–566, Jun 1950. doi: 10.1103/PhysRev.78.558.

[5] H. Aeppli, H. Albers-Schönberg, A. S. Bishop, H. Frauenfelder, and E. Heer. The determination of the magnetic moment of an excited nuclear level (^{111}Cd, 247 keV). *Phys. Rev.*, 84(2):370–371, Oct 1951. doi: 10.1103/PhysRev.84.370.

[6] F. Bloch, W. W. Hansen, and Martin Packard. Nuclear induction. *Phys. Rev.*, 69 (3-4):127, Feb 1946. doi: 10.1103/PhysRev.69.127.

[7] B. N. Samoilov, V. V. Sklyarevskii, and E. P. Stepanov. *Soviet Physics JETP*, 9 (448), 1959.

[8] Pramila Raghavan. Table of nuclear moments. *Atomic Data and Nuclear Data Tables*, 42(2):189 – 291, 1989. ISSN 0092-640X. doi: 10.1016/0092-640X(89)90008-9. URL `http://www.sciencedirect.com/science/article/B6WBB-4DBJ0YV-1Y/2/c0265097fe266166f71cd04769fdfc79`.

[9] N.J. Stone. Table of nuclear magnetic dipole and electric quadrupole moments. *Atomic Data and Nuclear Data Tables*, 90(1):75 – 176, 2005. ISSN 0092-640X. doi:

DOI:10.1016/j.adt.2005.04.001. URL http://www.sciencedirect.com/science/article/B6WBB-4GMJ8Y7-1/2/a677b740311c219a5a05406a1616e69c.

[10] Akito Arima and Hisashi Horie. Configuration mixing and magnetic moments of nuclei. *Progress of Theoretical Physics*, 11(4):509 –511, 1954. doi: 10.1143/PTP.11.509. URL http://ptp.ipap.jp/link?PTP/11/509/.

[11] Akito Arima and Hisashi Horie. Configuration mixing and magnetic moments of odd nuclei. *Progress of Theoretical Physics*, 12(5):623–641, 1954. doi: 10.1143/PTP.12.623. URL http://ptp.ipap.jp/link?PTP/12/623/.

[12] A. Bohr and B. R. Mottelson. *Nuclear Structure*. World Scientific Publishing Company, 1998.

[13] G. Breit and E. Wigner. Capture of slow neutrons. *Phys. Rev.*, 49(7):519–531, Apr 1936. doi: 10.1103/PhysRev.49.519.

[14] G. Goldring, Y. Niv, Y. Wolfson, and A. Zemel. Magnetic hyperfine rotation of a γ-ray angular distribution due to target tilting. *Phys. Rev. Lett.*, 38(5):221–224, Jan 1977. doi: 10.1103/PhysRevLett.38.221.

[15] A. E. Stuchbery and N. J. Stone. Recoil in vacuum for Te ions: Calibration, models, and applications to radioactive-beam g-factor measurements. *Phys. Rev. C*, 76(3):034307, Sep 2007. doi: 10.1103/PhysRevC.76.034307.

[16] The ISOLDE and Neutron Time of flight Committee (INTC). Minutes of the 37th INTC meeting, 2010. URL http://committees.web.cern.ch/committees/intc/minutes/intc37.pdf.

[17] A. E. Stuchbery, S. S. Anderssen, A. P. Byrne, P. M. Davidson, G. D. Dracoulis, and G. J. Lane. Measured magnetic moments and shape coexistence in the neutron-deficient nuclei ^{184,186,188}Pt. *Phys. Rev. Lett.*, 76(13):2246–2249, Mar 1996. doi: 10.1103/PhysRevLett.76.2246.

[18] Rolf Widerøe. Über ein neues Prinzip zur Herstellung hoher Spannungen. *Electrical Engineering (Archiv fur Elektrotechnik)*, 21(4):387–406, July 1928. ISSN 0948-7921 (Print) 1432-0487 (Online). doi: 10.1007/BF01656341. URL http://www.springerlink.com/content/x575410l0l950436/.

[19] E. Rutherford. *Radioactive substances and their radiations*. Cambridge University Press, Cambridge [England] :, 1913.

[20] L. D. Landau. *Physik Z Sowjetunion 1*, 88, 1932.

[21] V. F. Weisskopf. Excitation of nuclei by bombardment with charged particles. *Phys. Rev.*, 53(12):1018, Jun 1938. doi: 10.1103/PhysRev.53.1018.

[22] S. W. Barnes and P. W. Aradine. Radioactivity induced by nuclear excitation II. excitation by protons. *Phys. Rev.*, 55(1):50–52, Jan 1939. doi: 10.1103/PhysRev.55.50.

[23] Charles J. Mullin and Eugene Guth. Electric excitation and disintegration of nuclei. I. excitation and disintegration of nuclei by the Coulomb field of positive particles. *Phys. Rev.*, 82(2):141–155, Apr 1951. doi: 10.1103/PhysRev.82.141.

[24] C. A. Bertulani, A. E. Stuchbery, T. J. Mertzimekis, and A. D. Davies. Intermediate energy Coulomb excitation as a probe of nuclear structure at radioactive beam facilities. *Phys. Rev. C*, 68(4):044609, Oct 2003. doi: 10.1103/PhysRevC.68.044609.

[25] K. Alder, A. Bohr, T. Huus, B. Mottelson, and A. Winther. Study of nuclear structure by electromagnetic excitation with accelerated ions. *Rev. Mod. Phys.*, 28 (4):432–542, Oct 1956. doi: 10.1103/RevModPhys.28.432.

[26] Aage Winther and Kurt Alder. Relativistic Coulomb excitation. *Nuclear Physics A*, 319(3):518 – 532, 1979. ISSN 0375-9474. doi: 10.1016/0375-9474(79)90528-1. URL http://www.sciencedirect.com/science/article/B6TVB-473M8N3-MP/2/fccb056288555a4c400357b0ca6a7eaf.

[27] A. N. F. Aleixo and C. A. Bertulani. Coulomb excitation in intermediate-energy collisions. *Nuclear Physics A*, 505(2):448 – 470, 1989. ISSN 0375-9474. doi: 10.1016/0375-9474(89)90385-0. URL http://www.sciencedirect.com/science/article/B6TVB-473NFD5-S3/2/fc4f2a86a18d88347151fc5de360d328.

[28] A. E. Stuchbery. private communication, 2010.

[29] Andrew E. Stuchbery. Some notes on the program GKINT: Transient-field *g*-factor kinematics at intermediate energies, 2006. URL http://www.citebase.org/abstract?id=oai:arXiv.org:nucl-ex/0609032.

[30] Andrew E. Stuchbery. γ-ray angular distributions and correlations after projectile-fragmentation reactions. *Nuclear Physics A*, 723(1-2):69 – 92, 2003. ISSN 0375-9474. doi: 10.1016/S0375-9474(03)01157-6. URL http://www.sciencedirect.com/science/article/B6TVB-488VSSD-2/2/9e9e3be137ac60a6903089f64b95cee2.

[31] A. E. Stuchbery, T. H. Heseltine, S. S. Anderssen, H. H. Bolotin, A. P. Byrne, B. Fabricius, and T. Kibedi. Systematic measurements of transient fields for W, Os and Pt ions traversing Fe. *Hyperfine Interactions*, 88(1):97–119, December

1994. ISSN 0304-3843 (Print) 1572-9540 (Online). doi: 10.1007/BF02068707. URL http://www.springerlink.com/content/v0872u2043765626/.

[32] A.E. Stuchbery, A.N. Wilson, and P.M. Davidson. Equilibrium charge-state distributions for S and Si ions emerging from iron and gadolinium targets with velocities near their K-shell electron velocity. *Nuclear Instruments and Methods in Physics Research Section B: Beam Interactions with Materials and Atoms*, 243(2):265 – 271, 2006. ISSN 0168-583X. doi: 10.1016/j.nimb.2005.09.015. URL http://www.sciencedirect.com/science/article/B6TJN-4HH8171-9/2/a312dbb4ea05b20b9d8fe10c39861067.

[33] Heather Olliver, Thomas Glasmacher, and Andrew E. Stuchbery. Angular distributions of γ rays with intermediate-energy beams. *Phys. Rev. C*, 68(4):044312, Oct 2003. doi: 10.1103/PhysRevC.68.044312.

[34] A. E. Stuchbery. private communication, 2010.

[35] R. R. Borchers, J. D. Bronson, D. E. Murnick, and L. Grodzins. Magnetic moments of 2^+ states in even Te nuclei. *Phys. Rev. Lett.*, 17(21):1099–1102, Nov 1966. doi: 10.1103/PhysRevLett.17.1099.

[36] Jens Lindhard and Aage Winther. Transient fields acting on heavy ions during slowing-down in magnetized materials. *Nuclear Physics A*, 166(3): 413 – 435, 1971. ISSN 0375-9474. doi: 10.1016/0375-9474(71)90898-0. URL http://www.sciencedirect.com/science/article/B6TVB-47197HN-140/2/432a04391337f1670ba3177af85c97b9.

[37] G. K. Hubler, H. W. Kugel, and D. E. Murnick. Nuclear magnetic moments of very short-lived states via the transient-field implantation perturbed-angular-correlation technique. *Phys. Rev. C*, 9(5):1954–1964, May 1974. doi: 10.1103/PhysRevC.9.1954.

[38] M. Forterre, J. Gerber, J. P. Vivien, M. B. Goldberg, and K. H. Speidel. The sign of the magnetic moment of the first 2^+ state in ^{18}O. *Physics Letters B*, 55(1):56 – 58, 1975. ISSN 0370-2693. doi: 10.1016/0370-2693(75)90186-0. URL http://www.sciencedirect.com/science/article/B6TVN-470N5Y4-7Y/2/29be75b4b677022fa1f310add95c44bb.

[39] M. Forterre, J. Gerber, J. P. Vivien, M. B. Goldberg, K. H. Speidel, and P. N. Tandon. Transient field at nitrogen nuclei recoiling in iron and the magnetic moment of the ^{15}N first excited state. *Phys. Rev. C*, 11(6):1976–1982, Jun 1975. doi: 10.1103/PhysRevC.11.1976.

[40] J. L. Eberhardt, G. Van Middelkoop, R. E. Horstman, and H. A. Doubt. Anomalously large transient field through polarized electron capture. *Physics Letters B*, 56(4):329 – 331, 1975. ISSN 0370-2693. doi: 10.1016/0370-2693(75)90311-1. URL `http://www.sciencedirect.com/science/article/B6TVN-46YT02H-3H1/2/ddc3248bc007740224f0a06d2682827b`.

[41] J. L. Eberhardt, R. E. Horstman, P. C. Zalm, H. A. Doubt, and G. Van Middelkoop. Large transient magnetic fields at high ion velocities in polarized iron. *Hyperfine Interactions*, 3(1):195 – 212, 1977. doi: 10.1007/BF01021550.

[42] N Benczer-Koller, M Hass, and J Sak. Transient magnetic fields at swift ions traversing ferromagnetic media and application to measurements of nuclear moments. *Annual Review of Nuclear and Particle Science*, 30(1):53–84, 1980. doi: 10.1146/annurev.ns.30.120180.000413. URL `http://arjournals.annualreviews.org/doi/abs/10.1146/annurev.ns.30.120180.000413`.

[43] J. L. Eberhardt, R. E. Horstman, P. C. Zalm, H. A. Doubt, 4, and G. Van Middelkoop. Large transient magnetic fields at high ion velocities in polarized iron. *Hyperfine Interactions*, 3(1):195–212, January 1977. ISSN 0304-3843 (Print) 1572-9540 (Online). doi: 10.1007/BF01021550. URL `http://www.springerlink.com/content/r561h3373h345h51/`.

[44] N. K. B. Shu, D. Melnik, J. M. Brennan, W. Semmler, and N. Benczer-Koller. Velocity dependence of the dynamic magnetic field acting on swift O and Sm ions. *Phys. Rev. C*, 21(5):1828–1837, May 1980. doi: 10.1103/PhysRevC.21.1828.

[45] H. R. Andrews, O. Hausser, D. Ward, P. Taras, R. Nicole, J. Keinonen, P. Skensved, and B. Haas. Calibration of the transient magnetic field for rare-earth nuclei in iron: Application to g-factors of high spin states in ^{152,154}Sm. *Nuclear Physics A*, 383(3):509 – 529, 1982. ISSN 0375-9474. doi: 10.1016/0375-9474(82)90088-4. URL `http://www.sciencedirect.com/science/article/B6TVB-471XJ0C-218/2/ef3234e04be1a0cd612e587d1b38cb1d`.

[46] G. J. Kumbartzki, K. Hagemeyer, W. Knauer, G. Krösing, R. Kuhnen, V. Mertens, K. H. Speidel, J. Gerber, and W. Nagel. The ^{12}C 2_1^+ state as probe for transient magnetic fields in polarized iron. *Hyperfine Interactions*, 7(1):253–264, March 1979. ISSN 0304-3843 (Print) 1572-9540 (Online). doi: 10.1007/BF01021508. URL `http://www.springerlink.com/content/gl80621813u2870n/`.

[47] Andrew E. Stuchbery. Transient-field strengths for high-velocity light ions and applications to g-factor measurementson fast exotic beams. *Phys. Rev. C*, 69(6):064311, Jun 2004. doi: 10.1103/PhysRevC.69.064311.

[48] N. Rud and K. Dybdal. The transient magnetic field acting on swift nuclei moving in magnetized solids. *Physica Scripta*, 34(6A):561, 1986. URL `http://stacks.iop.org/1402-4896/34/i=6A/a=012`.

[49] K. H. Speidel, O. Kenn, and F. Nowacki. Magnetic moments and nuclear structure. *Progress in Particle and Nuclear Physics*, 49(1):91 – 154, 2002. ISSN 0146-6410. doi: 10.1016/S0146-6410(02)00144-8. URL `http://www.sciencedirect.com/science/article/B6TJC-4757VKT-3/2/5e4ba7bd322de2d617dc500e083240ca`.

[50] K. H. Speidel. New developments in transient field measurements. *Hyperfine Interactions*, 80(1-4):1205–1218, March 1993. ISSN 0304-3843 (Print) 1572-9540 (Online). doi: 10.1007/BF00567485. URL `http://www.springerlink.com/content/v882083623lr5161/`.

[51] K. Dybdal, J.S. Forster, and N. Rud. On the origin of transient magnetic fields. *Nuclear Instruments and Methods*, 170(1-3):233 – 242, 1980. ISSN 0029-554X. doi: 10.1016/0029-554X(80)91018-6. URL `http://www.sciencedirect.com/science/article/B73DN-471YM8T-55/2/4fe165353237395757fd991fe2d674ff`.

[52] F. Hagelberg, T. P. Das, and K.-H. Speidel. Spin exchange between ion probes and localized moments in ferromagnets as the origin of transient fields. *Phys. Rev. C*, 48(5):2230–2237, Nov 1993. doi: 10.1103/PhysRevC.48.2230.

[53] K Dybdal and N Rud. The K-shell population of ions penetrating ferromagnetic solids. *Physica Scripta*, 35(4):441, 1987. URL `http://stacks.iop.org/1402-4896/35/i=4/a=006`.

[54] Lokesh C. Tribedi, K. G. Prasad, and P. N. Tandon. K-shell vacancies carried by swift O and Si ions inside ferromagnetic hosts. *Phys. Rev. A*, 51(5):3783–3789, May 1995. doi: 10.1103/PhysRevA.51.3783.

[55] U. Grabowy, K.-H. Speidel, J. Cub, H. Busch, H.-J. Wollersheim, G. Jakob, A. Gohla, J. Gerber, and M. Loewe. Transient magnetic field and electric field gradient of fast H-like ^{52}Cr ions traversing Gd targets. *Zeitschrift fÃ¼r Physik A Hadrons and Nuclei*, 359(4):377–383, December 1997. ISSN 0939-7922 (Print) 1431-5831 (Online). URL `http://www.springerlink.de/content/68reuj08qannbrqt/`.

[56] H. E. Nigh, S. Legvold, and F. H. Spedding. Magnetization and electrical resistivity of gadolinium single crystals. *Phys. Rev.*, 132(3):1092–1097, Nov 1963. doi: 10.1103/PhysRev.132.1092.

[57] W.M. Elsasser. Sur le principe de pauli dans les noyaux - III. *J. Phys. Radium*, 5 (12):635–639, 1934. doi: 10.1051/jphysrad:01934005012063500. URL http://dx.doi.org/10.1051/jphysrad:01934005012063500.

[58] Karen E. Johnson. From natural history to the nuclear shell model: Chemical thinking in the work of Mayer, Haxel, Jensen, and Suess. *Physics in Perspective (PIP)*, 6:295–309, 2004. ISSN 1422-6944. URL http://dx.doi.org/10.1007/s00016-003-0203-x. 10.1007/s00016-003-0203-x.

[59] N. Bohr. Neutron capture and nuclear constitution. *Nature*, 137(3461):344–348, 1936. doi: 10.1038/137344a0.

[60] Maria G. Mayer. On closed shells in nuclei. *Phys. Rev.*, 74(3):235–239, Aug 1948. doi: 10.1103/PhysRev.74.235.

[61] Maria Goeppert Mayer. On closed shells in nuclei. II. *Phys. Rev.*, 75(12):1969–1970, Jun 1949. doi: 10.1103/PhysRev.75.1969.

[62] Otto Haxel, J. Hans D. Jensen, and Hans E. Suess. On the “magic numbers” in nuclear structure. *Phys. Rev.*, 75(11):1766, Jun 1949. doi: 10.1103/PhysRev.75.1766.2.

[63] K. A. Brueckner. Nuclear saturation and two-body forces. II. tensor forces. *Phys. Rev.*, 96(2):508–516, Oct 1954. doi: 10.1103/PhysRev.96.508.

[64] Hans A. Weidenmüller. Why the shell-model came as a surprise: In memoriam J. Hans D. Jensen. *Nuclear Physics A*, 507(1):5 – 13, 1990. ISSN 0375-9474. doi: 10.1016/0375-9474(90)90564-3. URL http://www.sciencedirect.com/science/article/B6TVB-472BFK9-1F/2/b8bb5617e0a86e70cc76a608789da33e.

[65] C. Thibault, R. Klapisch, C. Rigaud, A. M. Poskanzer, R. Prieels, L. Lessard, and W. Reisdorf. Direct measurement of the masses of ^{11}Li and $^{26-32}$Na with an on-line mass spectrometer. *Phys. Rev. C*, 12(2):644–657, Aug 1975. doi: 10.1103/PhysRevC.12.644.

[66] A. Ozawa, T. Kobayashi, T. Suzuki, K. Yoshida, and I. Tanihata. New magic number, $N = 16$, near the neutron drip line. *Phys. Rev. Lett.*, 84(24):5493–5495, Jun 2000. doi: 10.1103/PhysRevLett.84.5493.

[67] H. Iwasaki, T. Motobayashi, H. Akiyoshi, Y. Ando, N. Fukuda, H. Fujiwara, Zs. Fülöp, K. I. Hahn, Y. Higurashi, M. Hirai, I. Hisanaga, N. Iwasa, T. Kijima, A. Mengoni, T. Minemura, T. Nakamura, M. Notani, S. Ozawa, H. Sagawa, H. Sakurai, S. Shimoura, S. Takeuchi, T. Teranishi, Y. Yanagisawa, and M. Ishihara. Low-lying intruder 1^- state in ^{12}Be and the melting of the $N = 8$ shell

closure. *Physics Letters B*, 491(1-2):8 – 14, 2000. ISSN 0370-2693. doi: 10.1016/S0370-2693(00)01017-0. URL http://www.sciencedirect.com/science/article/B6TVN-41FMSBN-2/2/77a9bcd8cc9eece7dbe1f7658556a304.

[68] A. Navin, D. W. Anthony, T. Aumann, T. Baumann, D. Bazin, Y. Blumenfeld, B. A. Brown, T. Glasmacher, P. G. Hansen, R. W. Ibbotson, P. A. Lofy, V. Maddalena, K. Miller, T. Nakamura, B. V. Pritychenko, B. M. Sherrill, E. Spears, M. Steiner, J. A. Tostevin, J. Yurkon, and A. Wagner. Direct evidence for the breakdown of the $N = 8$ shell closure in ^{12}Be. *Phys. Rev. Lett.*, 85(2):266–269, Jul 2000. doi: 10.1103/PhysRevLett.85.266.

[69] S. D. Pain, W. N. Catford, N. A. Orr, J. C. Angélique, N. I. Ashwood, V. Bouchat, N. M. Clarke, N. Curtis, M. Freer, B. R. Fulton, F. Hanappe, M. Labiche, J. L. Lecouey, R. C. Lemmon, D. Mahboub, A. Ninane, G. Normand, N. Soić, L. Stuttge, C. N. Timis, J. A. Tostevin, J. S. Winfield, and V. Ziman. Structure of ^{12}Be: Intruder d-wave strength at $N = 8$. *Phys. Rev. Lett.*, 96(3):032502, Jan 2006. doi: 10.1103/PhysRevLett.96.032502.

[70] Hideki Yukawa. On the interaction of elementary particles. *Proc. Phys. Math. Soc. Jap.*, 17:48–57, 1935.

[71] Akito Arima and Tokuo Terasawa. Spin-orbit splitting and tensor force. II. *Progress of Theoretical Physics*, 23(1):115–136, 1960. doi: 10.1143/PTP.23.115. URL http://ptp.ipap.jp/link?PTP/23/115/.

[72] B. S. Pudliner, V. R. Pandharipande, J. Carlson, Steven C. Pieper, and R. B. Wiringa. Quantum Monte Carlo calculations of nuclei with $A < 7$. *Phys. Rev. C*, 56(4):1720–1750, Oct 1997. doi: 10.1103/PhysRevC.56.1720.

[73] Takaharu Otsuka, Toshio Suzuki, Rintaro Fujimoto, Hubert Grawe, and Yoshinori Akaishi. Evolution of nuclear shells due to the tensor force. *Phys. Rev. Lett.*, 95(23):232502, Nov 2005. doi: 10.1103/PhysRevLett.95.232502.

[74] R.K. Bansal and J.B. French. Multipole sum rules for single-nucleon-transfer spectroscopy. *Physics Letters*, 19(3):223 – 226, 1965. ISSN 0031-9163. doi: 10.1016/0031-9163(65)90079-X. URL http://www.sciencedirect.com/science/article/B6X44-46J38CX-4D/2/85f6c21db8ef2ad8f82c1ae2ed65b105.

[75] H. Grawe and M. Lewitowicz. Shell structure of nuclei far from stability. *Nuclear Physics A*, 693(1-2):116 – 132, 2001. ISSN 0375-9474. doi: 10.1016/S0375-9474(01)01138-1. URL http://www.sciencedirect.com/science/article/B6TVB-43W5CYS-B/2/af54e26375301d4e0926eb0b82798c04.

[76] C. Dossat, A. Bey, B. Blank, G. Canchel, A. Fleury, J. Giovinazzo, I. Matea, F. de Oliveira Santos, G. Georgiev, S. Grévy, I. Stefan, J. C. Thomas, N. Adimi, C. Borcea, D. Cortina Gil, M. Caamano, M. Stanoiu, F. Aksouh, B. A. Brown, and L. V. Grigorenko. Two-proton radioactivity studies with ^{45}Fe and ^{48}Ni. *Phys. Rev. C*, 72(5):054315, Nov 2005. doi: 10.1103/PhysRevC.72.054315.

[77] P. T. Hosmer, H. Schatz, A. Aprahamian, O. Arndt, R. R. C. Clement, A. Estrade, K.-L. Kratz, S. N. Liddick, P. F. Mantica, W. F. Mueller, F. Montes, A. C. Morton, M. Ouellette, E. Pellegrini, B. Pfeiffer, P. Reeder, P. Santi, M. Steiner, A. Stolz, B. E. Tomlin, W. B. Walters, and A. Wöhr. Half-life of the doubly magic r-process nucleus ^{78}Ni. *Phys. Rev. Lett.*, 94(11):112501, Mar 2005. doi: 10.1103/PhysRevLett.94.112501.

[78] M. Bernas, Ph. Dessagne, M. Langevin, J. Payet, F. Pougheon, and P. Roussel. Magic features of ^{68}Ni. *Physics Letters B*, 113(4):279 – 282, 1982. ISSN 0370-2693. doi: 10.1016/0370-2693(82)90039-9. URL `http://www.sciencedirect.com/science/article/B6TVN-46YKHT1-14B/2/52e2ffbc09bec0a7e15fe4e74928373e`.

[79] R. Broda, B. Fornal, W. Królas, T. Pawł at, D. Bazzacco, S. Lunardi, C. Rossi-Alvarez, R. Menegazzo, G. de Angelis, P. Bednarczyk, J. Rico, D. De Acuña, P. J. Daly, R. H. Mayer, M. Sferrazza, H. Grawe, K. H. Maier, and R. Schubart. $N = 40$ neutron subshell closure in the ^{68}Ni nucleus. *Phys. Rev. Lett.*, 74(6):868–871, Feb 1995. doi: 10.1103/PhysRevLett.74.868.

[80] Faisal Azaiez. In-beam γ-spectroscopy at GANIL: present and future. *Physica Scripta*, 2000(T88):118, 2000. URL `http://stacks.iop.org/1402-4896/2000/i=T88/a=021`.

[81] O. Sorlin, S. Leenhardt, C. Donzaud, J. Duprat, F. Azaiez, F. Nowacki, H. Grawe, Zs. Dombrádi, F. Amorini, A. Astier, D. Baiborodin, M. Belleguic, C. Borcea, C. Bourgeois, D. M. Cullen, Z. Dlouhy, E. Dragulescu, M. Górska, S. Grévy, D. Guillemaud-Mueller, G. Hagemann, B. Herskind, J. Kiener, R. Lemmon, M. Lewitowicz, S. M. Lukyanov, and P. Mayet. $^{68}_{28}$Ni$_{40}$: Magicity versus superfluidity. *Phys. Rev. Lett.*, 88(9):092501, Feb 2002. doi: 10.1103/PhysRevLett.88.092501.

[82] K. Langanke, J. Terasaki, F. Nowacki, D. J. Dean, and W. Nazarewicz. How magic is the magic ^{68}Ni nucleus? *Phys. Rev. C*, 67(4):044314, Apr 2003. doi: 10.1103/PhysRevC.67.044314.

[83] P.G. Reinhard, M. Bender, T. Buervenich, C. Reiss, J. Maruhn, and W. Greiner. Skyrme-Hartree-Fock in the realm of nuclear mean field models. *RIKEN Review*, 26:23–30, Jan 2000.

[84] D. Pauwels, O. Ivanov, N. Bree, J. Büscher, T. E. Cocolios, J. Gentens, M. Huyse, A. Korgul, Yu. Kudryavtsev, R. Raabe, M. Sawicka, I. Stefanescu, J. Van de Walle, P. Van den Bergh, P. Van Duppen, and W. B. Walters. Shape isomerism at N = 40: Discovery of a proton intruder state in ^{67}Co. *Physical Review C (Nuclear Physics)*, 78(4):041307, 2008. doi: 10.1103/PhysRevC.78.041307. URL http://link.aps.org/abstract/PRC/v78/e041307.

[85] M. Hannawald, T. Kautzsch, A. Wöhr, W. B. Walters, K.-L. Kratz, V. N. Fedoseyev, V. I. Mishin, W. Böhmer, B. Pfeiffer, V. Sebastian, Y. Jading, U. Köster, J. Lettry, H. L. Ravn, and the ISOLDE Collaboration. *Phys. Rev. Lett.*, 82(7): 1391–1394, Feb 1999. doi: 10.1103/PhysRevLett.82.1391.

[86] I. Stefanescu, G. Georgiev, D. L. Balabanski, N. Blasi, A. Blazhev, N. Bree, J. Cederkäll, T. E. Cocolios, T. Davinson, J. Diriken, J. Eberth, A. Ekström, D. Fedorov, V. N. Fedosseev, L. M. Fraile, S. Franchoo, K. Gladnishki, M. Huyse, O. Ivanov, V. Ivanov, J. Iwanicki, J. Jolie, T. Konstantinopoulos, Th. Kröll, R. Krücken, U. Köster, A. Lagoyannis, G. Lo Bianco, P. Maierbeck, B. A. Marsh, P. Napiorkowski, N. Patronis, D. Pauwels, G. Rainovski, P. Reiter, K. Riisager, M. Seliverstov, G. Sletten, J. Van de Walle, P. Van Duppen, D. Voulot, N. Warr, F. Wenander, and K. Wrzosek. Interplay between single-particle and collective effects in the odd-A Cu isotopes beyond $N = 40$. *Phys. Rev. Lett.*, 100(11):112502, Mar 2008. doi: 10.1103/PhysRevLett.100.112502.

[87] S. Franchoo, M. Huyse, K. Kruglov, Y. Kudryavtsev, W. F. Mueller, R. Raabe, I. Reusen, P. Van Duppen, J. Van Roosbroeck, L. Vermeeren, A. Wöhr, H. Grawe, K.-L. Kratz, B. Pfeiffer, and W. B. Walters. Monopole migration in ^{69,71,73}Cu observed from β decay of laser-ionized $^{68-74}$Ni. *Phys. Rev. C*, 64(5):054308, Oct 2001. doi: 10.1103/PhysRevC.64.054308.

[88] M. Lewitowicz, J.M. Daugas, R. Grzywacz, L. Achouri, J.C. Angélique, D. Baiborodin, R. Béntida, R. Beraud, C. Bingham, C. Borcea, W. Catford, A. Emsallem, G. de France, M. Glogowski, H. Grawe, D. Guillemaud-Mueller, M. Houry, S. Hurskanen, K.L. Jones, R.C. Lemmon, A.C. Mueller, A. Nowak, F. de Oliveira-Santos, A. Plochocki, M. Pfutzner, P.H. Regan, K. Rykaczewski, M.G. Saint-Laurent, J.E. Sauvestre, M. Sawicka, M. Schaefer, G. Sletten, O. Sorlin, M. Stanoiu, J. Szerypo, W. Trinder, S. Viteritti, and J. Winfield. Study of μs-isomers in neutron-rich nuclei around $Z = 28$ and $N = 40$ shell closures. *Nuclear Physics A*, 654(1, Supplement 1):687c – 690c, 1999. ISSN 0375-9474. doi: 10.1016/S0375-9474(00)88527-9. URL http://www.sciencedirect.com/science/article/B6TVB-4066MSR-1M/2/b4a04c2f344e2a6680241a4de63caa47.

[89] H. Mach, M. Lewitowicz, M. Stanoiu, F. Becker, J. Blomqvist, M. J. G. Berge, R. Boutami, B. Cederwall, Z. Dlouhy, B. Fogelberg, L. M. Fraile, G. Georgiev, H. Grawe, R. Grzywacz, P. I. Johansson, W. Klamra, S. Lukyanov, M. Mineva, J. Mrazek, G. Neyens, F. de Oliveir Santos, M. Pfuzner, Yu. E. Penionzhkevich, E. Ramstrom, and M. Sawicka. Coupling of valence particles/holes to ^{68,70}Ni studied via measurements of the $B(E2)$ strength in ^{67,69,70}Ni and ^{71}Cu. *Nuclear Physics A*, 719:C213 – C216, 2003. ISSN 0375-9474. doi: 10.1016/S0375-9474(03)00920-5. URL `http://www.sciencedirect.com/science/article/B6TVB-48THMYN-1C/2/f0fe02d5ac2f3c8803c50764325a6055`.

[90] O. Perru, O. Sorlin, S. Franchoo, F. Azaiez, E. Bouchez, C. Bourgeois, A. Chatillon, J. M. Daugas, Z. Dlouhy, Zs. Dombrádi, C. Donzaud, L. Gaudefroy, H. Grawe, S. Grévy, D. Guillemaud-Mueller, F. Hammache, F. Ibrahim, Y. Le Coz, S. M. Lukyanov, I. Matea, J. Mrazek, F. Nowacki, Yu.-E. Penionzhkevich, F. de Oliveira Santos, F. Pougheon, M. G. Saint-Laurent, G. Sletten, M. Stanoiu, C. Stodel, Ch. Theisen, and D. Verney. Enhanced core polarization in ^{70}Ni and ^{74}Zn. *Phys. Rev. Lett.*, 96(23):232501, Jun 2006. doi: 10.1103/PhysRevLett.96.232501.

[91] M. Stanoiu. PhD thesis, GANIL, Caen, 2003.

[92] A. F. Lisetskiy, B. A. Brown, M. Horoi, and H. Grawe. New $T = 1$ effective interactions for the $f_{5/2}\ p_{3/2}\ p_{1/2}\ g_{9/2}$ model space: Implications for valence-mirror symmetry and seniority isomers. *Phys. Rev. C*, 70(4):044314, Oct 2004. doi: 10.1103/PhysRevC.70.044314.

[93] O. Sorlin and M.-G. Porquet. Nuclear magic numbers: New features far from stability. *Progress in Particle and Nuclear Physics*, 61(2):602 – 673, 2008. doi: 10.1016/j.ppnp.2008.05.001.

[94] William B. Walters. Monopole shifts of single-particle energy level and the positions of magic nuclides for very neutron-rich nuclides. *AIP Conference Proceedings*, 447 (1):196–203, 1998. doi: 10.1063/1.56737. URL `http://link.aip.org/link/?APC/447/196/1`.

[95] K. Heyde, J. Jolie, J. Moreau, J. Ryckebusch, M. Waroquier, P. Van Duppen, M. Huyse, and J. L. Wood. A shell-model description of 0^+ intruder states in even-even nuclei. *Nuclear Physics A*, 466(2):189 – 226, 1987. ISSN 0375-9474. doi: 10.1016/0375-9474(87)90439-8. URL `http://www.sciencedirect.com/science/article/B6TVB-473181X-5X/2/c404cda3db439f3cb360757edbe3fab1`.

[96] H. Grawe, M. Górska, Z. Hu, E. Roeckl, M. Lipoglavsek, C. Fahlander, J. Nyberg, R. Grzywacz, K. Rykaczewski, J. M. Daugas, and M. Lewitowicz. Interfaces of

nuclear structure studies-decay vs in-beam experiments. Technical Report GSI-99-16, GSI, Darmstadt, May 1999.

[97] N. A. Smirnova, A. De Maesschalck, A. Van Dyck, and K. Heyde. Shell-model description of monopole shift in neutron-rich Cu. *Phys. Rev. C*, 69(4):044306, Apr 2004. doi: 10.1103/PhysRevC.69.044306.

[98] K. T. Flanagan, P. Vingerhoets, M. Avgoulea, J. Billowes, M. L. Bissell, K. Blaum, B. Cheal, M. De Rydt, V. N. Fedosseev, D. H. Forest, Ch. Geppert, U. Köster, M. Kowalska, J. Krämer, K. L. Kratz, A. Krieger, E. Mané, B. A. Marsh, T. Materna, L. Mathieu, P. L. Molkanov, R. Neugart, G. Neyens, W. Nörtershäuser, M. D. Seliverstov, O. Serot, M. Schug, M. A. Sjoedin, J. R. Stone, N. J. Stone, H. H. Stroke, G. Tungate, D. T. Yordanov, and Yu. M. Volkov. Nuclear spins and magnetic moments of ^{71,73,75}Cu: Inversion of $\pi 2p_{3/2}$ and $\pi 1f_{5/2}$ levels in ^{75}Cu. *Phys. Rev. Lett.*, 103(14):142501, Oct 2009. doi: 10.1103/PhysRevLett.103.142501.

[99] Xiangdong Ji and B. H. Wildenthal. Shell-model calculations for the energy levels of the $N = 50$ isotones with $A = 80 - 87$. *Phys. Rev. C*, 40(1):389–398, Jul 1989. doi: 10.1103/PhysRevC.40.389.

[100] J Sinatkas, L D Skouras, D Strottman, and J D Vergados. Shell-model calculations in the $A = 80-100$ mass region: I. a study of the $N = 50$ nuclei. *Journal of Physics G: Nuclear and Particle Physics*, 18(8):1377, 1992. URL http://stacks.iop.org/0954-3899/18/i=8/a=012.

[101] A. M. Oros-Peusquens and P. F. Mantica. Particle-core coupling around ^{68}Ni: a study of the subshell closure at $N = 40$. *Nuclear Physics A*, 669(1-2):81 – 100, 2000. ISSN 0375-9474. doi: 10.1016/S0375-9474(99)00816-7. URL http://www.sciencedirect.com/science/article/B6TVB-3YVDV64-7/2/156226c0b1b0c69caf273979f79a6203.

[102] I. Stefanescu, D. Pauwels, N. Bree, T. E. Cocolios, J. Diriken, S. Franchoo, M. Huyse, O. Ivanov, Y. Kudryavtsev, N. Patronis, J. Van De Walle, P. Van Duppen, and W. B. Walters. Evidence for a β-decaying $1/2^-$ isomer in ^{71}Ni. *Phys. Rev. C*, 79(4):044325, Apr 2009. doi: 10.1103/PhysRevC.79.044325.

[103] D. Pauwels, O. Ivanov, N. Bree, J. Büscher, T. E. Cocolios, M. Huyse, Yu. Kudryavtsev, R. Raabe, M. Sawicka, J. Van de Walle, P. Van Duppen, A. Korgul, I. Stefanescu, A. A. Hecht, N. Hoteling, A. Wöhr, W. B. Walters, R. Broda, B. Fornal, W. Krolas, T. Pawlat, J. Wrzesinski, M. P. Carpenter, R. V. F. Janssens, T. Lauritsen, D. Seweryniak, S. Zhu, J. R. Stone, and X. Wang. Structure of ^{65,67}Co studied through the β decay of ^{65,67}Fe and a deep-inelastic reaction. *Phys. Rev. C*, 79(4):044309, Apr 2009. doi: 10.1103/PhysRevC.79.044309.

[104] O. Sorlin, C. Donzaud, F. Nowacki, J.C. Angélique, F. Azaiez, C. Bourgeois, V. Chiste, Z. Dlouhy, S. Grévy, D. Guillemaud-Mueller, F. Ibrahim, K.-L Kratz, M. Lewitowicz, S.M. Lukyanov, J. Mrasek, Yu.-E. Penionzhkevich, F. de Oliveira Santos, B. Pfeiffer, F. Pougheon, A. Poves, M.G. Saint-Laurent, and M. Stanoiu. New region of deformation in the neutron-rich $^{60}_{24}\mathrm{Cr}_{36}$ and $^{62}_{24}\mathrm{Cr}_{38}$. *The European Physical Journal A - Hadrons and Nuclei*, 16:55–61, 2003. ISSN 1434-6001. URL `http://dx.doi.org/10.1140/epja/i2002-10069-9`. 10.1140/epja/i2002-10069-9.

[105] P. Adrich, A. M. Amthor, D. Bazin, M. D. Bowen, B. A. Brown, C. M. Campbell, J. M. Cook, A. Gade, D. Galaviz, T. Glasmacher, S. McDaniel, D. Miller, A. Obertelli, Y. Shimbara, K. P. Siwek, J. A. Tostevin, and D. Weisshaar. In-beam γ-ray spectroscopy and inclusive two-proton knockout cross section measurements at $N \approx 40$. *Phys. Rev. C*, 77(5):054306, May 2008. doi: 10.1103/PhysRevC.77.054306.

[106] N. Aoi, H. Suzuki, E. Takeshita, S. Takeuchi, S. Ota, H. Baba, S. Bishop, T. Fukui, Y. Hashimoto, H.J. Ong, E. Ideguchi, K. Ieki, N. Imai, H. Iwasaki, S. Kanno, Y. Kondo, T. Kubo, K. Kurita, K. Kusaka, T. Minemura, T. Motobayashi, T. Nakabayashi, T. Nakamura, T. Nakao, M. Niikura, T. Okumura, T.K. Ohnishi, H. Sakurai, S. Shimoura, R. Sugo, D. Suzuki, M.K. Suzuki, M. Tamaki, K. Tanaka, Y. Togano, and K. Yamada. Shape transition observed in neutron-rich pf-shell isotopes studied via proton inelastic scattering. *Nuclear Physics A*, 805 (1-4):400c – 407c, 2008. ISSN 0375-9474. doi: 10.1016/j.nuclphysa.2008.02.280. URL `http://www.sciencedirect.com/science/article/B6TVB-4SHVKJK-21/2/d91130029923e089ecada67214c2a40f`. INPC 2007 - Proceedings of the 23rd International Nuclear Physics Conference.

[107] Muhammad Zamrun F., Zakarya Mohamed Mohamed Mahmoud, N. Takigawa, and K. Hagino. Structure of ^{72,74}Ge nuclei probed with a combined analysis of heavy-ion fusion reactions and Coulomb excitation. *Phys. Rev. C*, 81(4):044609, Apr 2010. doi: 10.1103/PhysRevC.81.044609.

[108] J. Dobaczewski, W. Nazarewicz, J. Skalski, and T. Werner. Nuclear deformation: A proton-neutron effect? *Phys. Rev. Lett.*, 60(22):2254–2257, May 1988. doi: 10.1103/PhysRevLett.60.2254.

[109] M. M. Sharma, M. A. Nagarajan, and P. Ring. Rho meson coupling in the relativistic mean field theory and description of exotic nuclei. *Physics Letters B*, 312(4):377 – 381, 1993. ISSN 0370-2693. doi: 10.1016/0370-2693(93)90970-S. URL `http://www.sciencedirect.com/science/article/B6TVN-470G13S-69/2/b3e2b625f3a9be50fc271b3986c87fda`.

[110] E. F. Aguilera, J. J. Kolata, and R. J. Tighe. Nuclear structure effects in the sub-barrier fusion of ^{16}O + ^{70,72,73,74,76}Ge. *Phys. Rev. C*, 52(6):3103–3113, Dec 1995. doi: 10.1103/PhysRevC.52.3103.

[111] E. F. Aguilera, J. J. Vega, J. J. Kolata, A. Morsad, R. G. Tighe, and X. J. Kong. Sub-barrier fusion of ^{27}Al+^{70,72,73,74,76}Ge: Evidence for shape transition and structure effects. *Phys. Rev. C*, 41(3):910–919, Mar 1990. doi: 10.1103/PhysRevC.41.910.

[112] D. Mücher, G. Gürdal, K.-H. Speidel, G. J. Kumbartzki, N. Benczer-Koller, S. J. Q. Robinson, Y. Y. Sharon, L. Zamick, A. F. Lisetskiy, R. J. Casperson, A. Heinz, B. Krieger, J. Leske, P. Maier-Komor, V. Werner, E. Williams, and R. Winkler. Nuclear structure studies of ^{70}Zn from g-factor and lifetime measurements. *Phys. Rev. C*, 79(5):054310, May 2009. doi: 10.1103/PhysRevC.79.054310.

[113] K. Moschner, K.-H. Speidel, J. Leske, C. Bauer, C. Bernards, L. Bettermann, M. Honma, T. Möller, P. Maier-Komor, and D. Mücher. New measurement of the ^{68}Zn (4_1^+) g factor combined with a reanalysis of previous data. *Phys. Rev. C*, 82(1):014301, Jul 2010. doi: 10.1103/PhysRevC.82.014301.

[114] M. Hasegawa, T. Mizusaki, K. Kaneko, and Y. Sun. Enhancement of $B(E2)\uparrow$ and low excitation of the second 0^+ state near $N = 40$ in Ge isotopes. *Nuclear Physics A*, 789(1-4):46 – 54, 2007. ISSN 0375-9474. doi: 10.1016/j.nuclphysa.2007.02.012. URL `http://www.sciencedirect.com/science/article/B6TVB-4N6FFJ6-1/2/67f51599f95531dab2ae36cb4ea9642a`.

[115] R. Grzywacz, R. Anne, G. Auger, D. Bazin, C. Borcea, V. Borrel, J. M. Corre, T. Dörfler, A. Fomichov, M. Gaelens, D. Guillemaud-Mueller, R. Hue, M. Huyse, Z. Janas, H. Keller, M. Lewitowicz, S. Lukyanov, A. C. Mueller, Yu. Penionzhkevich, M. Pfützner, F. Pougheon, K. Rykaczewski, M. G. Saint-Laurent, K. Schmidt, W. D. Schmidt-Ott, O. Sorlin, J. Szerypo, O. Tarasov, J. Wauters, and J. Zylicz. Identification of μs-isomers produced in the fragmentation of a ^{112}Sn beam. *Physics Letters B*, 355(3-4):439 – 446, 1995. ISSN 0370-2693. doi: 10.1016/0370-2693(95)00501-B. URL `http://www.sciencedirect.com/science/article/B6TVN-3YMWSS0-88/2/8f68530953d0892bec76115fa479a7c9`.

[116] R. Grzywacz. The structure of nuclei near ^{78}Ni from isomer and decay studies. *The European Physical Journal A - Hadrons and Nuclei*, 25:89–92, 2005. ISSN 1434-6001. URL `http://dx.doi.org/10.1140/epjad/i2005-06-209-7`. 10.1140/epjad/i2005-06-209-7.

[117] M. Sawicka, M. Pfützner, R. Grzywacz, J.M. Daugas, I. Matea, M. Lewitowicz, H. Grawe, F. Becker, G. Bélier, C. Bingham, R. Borcea, E. Bouchez,

A. Buta, E. Dragulescu, J.E. Sauvestre, G. Georgiev, J. Giovinazzo, F. Hammache, F. Ibrahim, P. Mayet, V. Méot, F. Negoita, F. Oliveira Santos, O. Perru, O. Roig, K.P. Rykaczewski, M.G. Saint-Laurent, O. Sorlin, M. Stanoiu, I. Stefan, C. Stodel, C. Theisen, and D. Verney. Evidence for an isomer in ^{76}Ni. *The European Physical Journal A - Hadrons and Nuclei*, 20:109–110, 2003. ISSN 1434-6001. URL `http://dx.doi.org/10.1140/epja/i2002-10333-0`. 10.1140/epja/i2002-10333-0.

[118] C. Mazzocchi, R. Grzywacz, J. C. Batchelder, C. R. Bingham, D. Fong, J. H. Hamilton, J. K. Hwang, M. Karny, W. Krolas, S. N. Liddick, P. F. Mantica, A. C. Morton, W. F. Mueller, K. P. Rykaczewski, M. Steiner, A. Stolz, and J. A. Winger. Isomer and beta-decay studies of nuclei near ^{78}Ni. *AIP Conference Proceedings*, 764(1):164–169, 2005. doi: 10.1063/1.1905306. URL `http://link.aip.org/link/?APC/764/164/1`.

[119] G. Georgiev, G. Neyens, M. Hass, D.L. Balabanski, C. Bingham, C. Borcea, N. Coulier, R. Coussement, J.M. Daugas, G. France, M. Górska, H. Grawe, R. Grzywacz, M. Lewitowicz, H. Mach, I. Matea, F. Oliveira Santos, R.D. Page, M. Pfützner, YuE. Penionzhkevich, Z. Podolyák, P.H. Regan, K. Rykaczewski, M. Sawicka, N.A. Smirnova, Yu Sobolev, M. Stanoiu, S. Teughels, and K. Vyvey. *g*-factors of isomeric states in the neutron-rich nuclei. *The European Physical Journal A - Hadrons and Nuclei*, 20:93–94, 2003. ISSN 1434-6001. URL `http://dx.doi.org/10.1140/epja/i2002-10328-9`. 10.1140/epja/i2002-10328-9.

[120] G. Georgiev, I. Matea, D. Balabanski, J. Daugas, F. de Oliveira Santos, S. Franchoo, F. Ibrahim, F. Le Blanc, M. Lewitowicz, G. Lo Bianco, S. Lukyanov, V. Meot, P. Morel, G. Neyens, Yu. Penionzhkevich, A. Saltarelli, O. Sorlin, M. Stanoiu, M. Tarisien, N. Vermeulen, D. Verney, and D. Yordanov. *g*-factor of the $9/2^+$ isomeric state in ^{65}Ni from transfer reaction. *The European Physical Journal A - Hadrons and Nuclei*, 30:351–356, 2006. ISSN 1434-6001. URL `http://dx.doi.org/10.1140/epja/i2006-10135-4`. 10.1140/epja/i2006-10135-4.

[121] J. Bleck, R. Michaelsen, W. Ribbe, and W. Zeitz. Energy, lifetime and *g*-factor of the first excited state in ^{63}Ni. *Physics Letters B*, 32 (1):41 – 42, 1970. ISSN 0370-2693. doi: 10.1016/0370-2693(70)90331-X. URL `http://www.sciencedirect.com/science/article/B6TVN-470W7CC-1K4/2/569b1a237059e7e35f2efd5efaa5bd80`.

[122] R. Anne, D. Bazin, A.C. Mueller, J.C. Jacmart, and M. Langevin. The achromatic spectrometer LISE at GANIL. *Nuclear Instruments and Methods in Physics*

Research Section A: Accelerators, Spectrometers, Detectors and Associated Equipment, 257(2):215 – 232, 1987. ISSN 0168-9002. doi: 10.1016/0168-9002(87)90741-8. URL http://www.sciencedirect.com/science/article/B6TJM-473FVM5-D7/2/96fc4f41834b9ac28e318f7ccf98f5f9.

[123] A. D. Davies, A. E. Stuchbery, P. F. Mantica, P. M. Davidson, A. N. Wilson, A. Becerril, B. A. Brown, C. M. Campbell, J. M. Cook, D. C. Dinca, A. Gade, S. N. Liddick, T. J. Mertzimekis, W. F. Mueller, J. R. Terry, B. E. Tomlin, K. Yoneda, and H. Zwahlen. Probing shell structure and shape changes in neutron-rich sulfur isotopes through transient-field g-factor measurements on fast radioactive beams of ^{38}S and ^{40}S. *Phys. Rev. Lett.*, 96(11):112503, Mar 2006. doi: 10.1103/PhysRevLett.96.112503.

[124] F. Azaiez. EXOGAM: a γ-ray spectrometer for radioactive beams. *Nuclear Physics A*, 654(1, Supplement 1):1003c – 1008c, 1999. doi: 10.1016/S0375-9474(00)88588-7.

[125] A Pakou, J Billowes, J Burde, J A G De Raedt, M A Grace, and W R Kolbl. Transient magnetic field measurements for even Ge isotopes. *Journal of Physics G: Nuclear Physics*, 10(12):1759, 1984. URL http://stacks.iop.org/0305-4616/10/i=12/a=014.

[126] G.J. Lampard, H.H. Bolotin, A.E. Stuchbery, C.E. Doran, and A.P. Byrne. Sytematics of gyromagnetic ratios of the 2_1^+ states in even Ge isotopes. *Australian Journal of Physics*, 40:117, 1987.

[127] O. Kenn, K.-H. Speidel, R. Ernst, S. Schielke, S. Wagner, J. Gerber, P. Maier-Komor, and F. Nowacki. Measurements of g factors and lifetimes of low-lying states in ^{70}Zn and their shell model implication. *Phys. Rev. C*, 65(3):034308, Feb 2002. doi: 10.1103/PhysRevC.65.034308.

[128] J. Leske, K.-H. Speidel, S. Schielke, J. Gerber, P. Maier-Komor, T. Engeland, and M. Hjorth-Jensen. Dominant $(g_{9/2})^2$ neutron configuration in the 4_1^+ state of ^{68}Zn based on new g factor measurements. *Phys. Rev. C*, 72(4):044301, Oct 2005. doi: 10.1103/PhysRevC.72.044301.

[129] M. Hjorth-Jensen. private communication, 2006.

[130] F. Nowacki. private communication, 2006.

[131] J. Van de Walle, F. Aksouh, F. Ames, T. Behrens, V. Bildstein, A. Blazhev, J. Cederkäll, E. Clément, T. E. Cocolios, T. Davinson, P. Delahaye, J. Eberth, A. Ekström, D. V. Fedorov, V. N. Fedosseev, L. M. Fraile, S. Franchoo, R. Gernhauser, G. Georgiev, D. Habs, K. Heyde, G. Huber, M. Huyse, F. Ibrahim, O. Ivanov,

J. Iwanicki, J. Jolie, O. Kester, U. Köster, T. Kröll, R. Krücken, M. Lauer, A. F. Lisetskiy, R. Lutter, B. A. Marsh, P. Mayet, O. Niedermaier, T. Nilsson, M. Pantea, O. Perru, R. Raabe, P. Reiter, M. Sawicka, H. Scheit, G. Schrieder, D. Schwalm, M. D. Seliverstov, T. Sieber, G. Sletten, N. Smirnova, M. Stanoiu, I. Stefanescu, J.-C. Thomas, J. J. Valiente-Dobón, P. Van Duppen, D. Verney, D. Voulot, N. Warr, D. Weisshaar, F. Wenander, B. H. Wolf, and M. Zielińska. Coulomb excitation of neutron-rich Zn isotopes: First observation of the 2_1^+ state in ^{80}Zn. *Phys. Rev. Lett.*, 99(14):142501, Oct 2007. doi: 10.1103/PhysRevLett.99.142501.

[132] O. Kenn, K.-H. Speidel, R. Ernst, J. Gerber, P. Maier-Komor, and F. Nowacki. Measurements of g factors and lifetimes of low lying states in $^{58-64}$Ni and their shell model implications. *Phys. Rev. C*, 63(6):064306, May 2001. doi: 10.1103/PhysRevC.63.064306.

[133] S. Leenhardt, O. Sorlin, M. G. Porquet, F. Azaiez, J. C. Angélique, M. Belleguic, C. Borcea, C. Bourgeois, J. M. Daugas, C. Donzaud, I. Deloncle, J. Duprat, A. Gillibert, D. Grévy, S. Guillemaud-Mueller, J. Kiener, M. Lewitowicz, S.M. Lukyanov, F. Marie, N.A. Orr, Yu.-E. Penionzhkevich, F. de Oliveira Santos, F. Pougheon, M. G. Saint-Laurent, W. Shuying, Yu. Sobolev, and J.S. Winfield. Coulomb excitation of $^{72}_{30}$Zn$_{42}$. *The European Physical Journal A - Hadrons and Nuclei*, Volume 14:1–5, May 2002. doi: 10.1140/epja/iepja1358.

[134] T. J. Mertzimekis, A. E. Stuchbery, N. Benczer-Koller, and M. J. Taylor. Systematics of first 2^+ state g-factors around mass 80. *Phys. Rev. C*, 68(5):054304, Nov 2003. doi: 10.1103/PhysRevC.68.054304.

[135] J. Leske, K.-H. Speidel, S. Schielke, O. Kenn, J. Gerber, P. Maier-Komor, S. J. Q. Robinson, A. Escuderos, Y. Y. Sharon, and L. Zamick. Nuclear structure of the first 2^+ state in radioactive ^{68}Ge based on g factor and lifetime measurements. *Phys. Rev. C*, 71(4):044316, Apr 2005. doi: 10.1103/PhysRevC.71.044316.

[136] R. Lecomte, M. Irshad, S. Landsberger, G. Kajrys, P. Paradis, and S. Monaro. Coulomb-excitation studies of ^{70}Ge, ^{72}Ge, ^{74}Ge, and ^{76}Ge. *Phys. Rev. C*, 22(6):2420–2423, Dec 1980. doi: 10.1103/PhysRevC.22.2420.

[137] O.B. Tarasov and D. Bazin. LISE++: Radioactive beam production with in-flight separators. *Nuclear Instruments and Methods in Physics Research Section B: Beam Interactions with Materials and Atoms*, 266(19-20):4657 – 4664, 2008. ISSN 0168-583X. doi: 10.1016/j.nimb.2008.05.110. URL `http://www.sciencedirect.com/science/article/B6TJN-4SR7115-9/2/2812b311ac0f7b4d7b0066dc548acfdc`. Proceedings of the XVth International

Conference on Electromagnetic Isotope Separators and Techniques Related to their Applications.